Neutron Diffraction Study of *In Situ*-Reinforced Silicon Nitride during Creep

Thesis by

Geoffrey A. Swift

In Partial Fulfillment of the Requirements

for the Degree of

Doctor of Philosophy

California Institute of Technology

Pasadena, California

2004

(Defended March 4, 2004)

Acknowledgments

First and foremost, this research would not have been possible without the funding provided by the National Aeronautics and Space Administration. I would also like to thank all the personnel at the various national laboratories where I have been fortunate enough to perform experiments, on behalf of myself and for others. Thanks to my advisor, Ersan Üstündag, for the funding that allowed me to pursue this research.

Thanks to my thesis committee for their time and effort in reading this compilation of my research efforts at Caltech.

Perhaps most of all, I thank Professor Rasit Koc of Southern Illinois University at Carbondale, my former advisor and employer, for his unflagging support and confidence. Further thanks go to Dr. Maria Oh, for holding fast in belief that I could make it through to the end; to Prof. G. Ravichandran, for without his support, confidence and encouragement, I would not have gotten this far; to the incomparable Mike Vondrus, for always lending an ear for problems, being quick to help with design and machining of new components, and expressing his confidence in me; to Bjørn Clausen, for providing analysis tools and collaborating with determination of the AS800 stiffness tensor, the only portion of this research (including data collection, reduction, analysis, and interpretation) not done solely by myself. Finally, thanks to the men of the CCBTG, the creators of CBT, and the giant killer robots therein, for helping keep me sane!

"Always tell the truth; then you don't have to remember anything." – Mark Twain

Abstract

Neutron diffraction was used to study the high-temperature creep of *in situ*-reinforced silicon nitride (ISR Si_3N_4). Full pattern and single peak fitting methods were used to calculate the average and *hkl*-specific mechanical properties, including thermal expansion coefficient, creep exponent, Young's modulus, and Poisson's ratio. This is both the first in-depth study using time-of-flight neutron diffraction to examine materials at such high temperatures (above 1273K) and the first *in situ* microstructural study of creeping silicon nitride. Two commercial grades of ISR Si_3N_4 were tested, AS800 and GS-44.

The refractory grain boundary phase of AS800 prevented the onset of creep in the vacuum environment of the SMARTS furnace. However, the high-temperature stress-strain data allowed determination of the 1648 K single crystal elastic stiffness tensor, the first such calculation from neutron diffraction strain data. Also determined was the coefficient of thermal expansion (CTE) tensor. The 1648 K stiffness tensor indicated a less stiff C_{33} component compared to a room temperature stiffness tensor. This lesser value is due either to microstructural (grain-grain interaction) or thermal effects.

Creep was observed for GS-44. A stress step-up test and four constant stress creep tests were performed. Large strains were measured by an extensometer, though of much less magnitude than literature creep studies, with the difference attributed to the vacuum environment protecting the grain boundary phase from suffering reduced viscosity. This is supportive evidence of the long-held notion that the grain boundary phase is the primary determinate of creep behavior. The diffraction strains, though of significantly

lower magnitude than the extensometer strains, were measured as non-constant, though the silicon nitride lattice parameters behaved in an unexpected manner. The two lattice parameters were seen to split or fork from a common initial strain, with the *c* lattice parameter indicating tensile strain and the *a* lattice parameter compressive. The relative changes, however, corresponded to an essentially constant unit cell volume, as computed from simple geometry. None of the potential inelastic strain effects on diffraction peaks, such as peak broadening, were observed, further supporting the notion that the grain boundary phase is the source of strain. Neither was there any measured preferred orientation evolution due to creep. The creep exponent of GS-44 was calculated as 3.18, a greater value than in literature, likely due to the same creep inhibition of the vacuum furnace.

The classic Norton Equation for creep matched well with the steady-state creep rates as a function of applied stress, while a newer model by Luecke and Wiederhorn, incorporating multiple facets specific to Si_3N_4, matched the data comparably, though with an additional empirical stress dependence incorporated. The effect of performing these experiments in a vacuum rather than in air likely prevented as accurate prediction by their model as with Norton's. This result is based on the much-reduced creep strain measured compared to literature measurements of the same material at like temperature and stress. However, given the large disparity between the extensometer creep strain and the diffraction creep strain, it is clear that the grain boundary phase experiences the bulk of the deformation. Subsequent SEM observations of tested samples indicated no microstructural change due to the short duration of creep experiments. As with AS800, the GS-44 CTE tensor was

found, while the stiffness tensor was incalculable due to extreme non-linearity of single peak data.

Contents

List of Figures

List of Tables

I. Introduction

Ceramics have achieved greater widespread use worldwide as their properties are enhanced and verified through the efforts of materials scientists. Of particular interest is the use of ceramic materials for high-temperature structural applications, as ceramics have superior high-temperature properties, generally, than metals. For ceramics to be used at elevated temperatures it is important, particularly for structural applications, to understand the mechanical properties at elevated temperatures. Silicon nitride, Si_3N_4, is considered the most promising of ceramic materials for high-temperature structural applications [1, 2]. The history and processing of Si_3N_4 will be discussed briefly, with a focus on generalities and recent developments. The properties subsequent to such preparation methods will be discussed as relevant, primarily mechanical properties, as well as applications currently involving Si_3N_4.

1.1 Silicon Nitride

Silicon nitride does not occur in nature. There are two common polymorphs of Si_3N_4, α (trigonal) and β (hexagonal), while cubic Si_3N_4 has more recently been synthesized. The β polymorph (space group $P6_3/m$) is the more stable phase, and is the commonly found phase in densified parts made of Si_3N_4 [2, 3]. The α form is known to convert into β at high temperature, while the reverse process is energetically unfavorable [3]. Thus the α-β transformation is permanent, since the β-α transformation does not occur. When properties are discussed they will be those of β-Si_3N_4; hereafter if Si_3N_4 is used, it is referring to β-Si_3N_4. However, before solid parts can be made, Si_3N_4 powder must be synthesized. This powder is then compacted and densified by one of several methods

requiring high temperature and, sometimes, high pressure.

1.1.1 Powder Synthesis

Si_3N_4 is synthesized in a variety of methods, with varying effects on the resulting properties. First, however, high-quality powder must be prepared. There are several techniques used in industry today. These include direct nitridation, carbothermal reduction and nitridation, imide processing, and vapor phase reaction. The starting materials are either silicon (Si) powder, silicon dioxide (silica, SiO_2), or silicon tetrachloride ($SiCl_4$), depending upon the process. Regardless of which process is employed, it is desired to produce powders that are high-purity, free of agglomerations, spherical, sub-μm in size, and possessing a narrow size distribution [4, 5].

Direct nitridation of silicon is an older method, generally used to produce β-Si_3N_4 powder for refractory purposes [5]. The reaction proceeds according to:

$$3Si + 2N_{2(g)} \rightarrow Si_3N_4 \qquad (1)$$

Depending on the quality of the starting powders, reaction time and resulting quality are affected. This process generally produces coarse, agglomerated particles, requiring milling to obtain a suitable powder. Resulting powders are α-Si_3N_4, only being converted to β-Si_3N_4 during densification.

Diimide decomposition utilizes $SiCl_4$ and ammonia to produce Si_3N_4 powder [5]. The first step in this process produces an intimate mixture of ammonium chloride and silicon diimide. Washing with liquid ammonia followed by a sublimation/calcination step produces silicon imide chloride. A final evaporation of the ammonium chloride thus

produced yields a mixture of amorphous Si-N compounds which are crystallized above 1250°C, influenced by conditions including such as impurities, heating time, and atmosphere. There is usually residual chlorine impurity in the reaction products. Again, fine powder requires milling to produce.

The vapor phase reaction makes use of the high-temperature reaction [5]

$$3SiCl_{4(g)} + 4NH_{3(l)} \rightarrow Si_3N_4 + 12HCl_{(g)} \qquad (2)$$

Temperatures up to 1350°C can be required to effect this reaction, with some residual silicon diimide being common. This must be removed by the same calcination/crystallization as for diimide decomposition. The Si_3N_4 produced is amorphous and is crystallized by heat treating.

Carbothermal reduction and nitridation is a commonly applied method, due to the low cost of starting materials and the relatively high-quality resulting powders [5, 6]. The starting materials are silica and carbon, both commercially available at low costs. These are reacted at around 1500°C in the presence of nitrogen first to reduce the silica then to nitridate it. The overall reaction is

$$3SiO_{2(g)} + 2N_{2(g)} + 6C \rightarrow Si_3N_4 + 6CO_{(g)} \qquad (3)$$

The powders are usually highly α phase, being the preferred phase for *powders*, with carbon contamination <1%. While the powders are near-fine, milling is often employed to reduce the size.

1.1.2 Powder Densification

The various methods for densifying ceramic powders are general, and are used to densify

many different materials. The methods include pressureless sintering, hot-pressing, and hot isostatic pressing, for example. Another method is reaction bonding, which actually merges the powder synthesis and densification steps.

Sintering is the general process by which ceramic powders are densified [4, 7, 8]. Pressureless sintering is the process by which high temperature is applied to a compacted powder form (called the green state or green article) such that the energy input from the furnace heat drives a surface area reduction of the powders. This is accomplished by the bonding of neighboring particles. This bonding reduces the surface area of the particles, and thus their surface energy. It is for this reason that fine-size (and thus high surface area) powders are desired. Other factors affect the densification, like powder packing density, which is the motivation for obtaining spherical particles with a narrow size distribution, and low state of agglomeration. Impurities affect the process by altering the temperature at which densification will occur, in addition to affecting the properties of the resulting final article [4].

In the case of many ceramics, including Si_3N_4, densification cannot be achieved at a low temperature in a short time (since grains grow at elevated temperatures by the same mechanism that drives sintering, reducing the time at the processing temperature is necessary to allow for small grain size, which relates to increased strength) unless sintering aids are used [4, 6]. In many cases, these aids are used to generate liquid phase sintering. That is, the foreign particles melt during the processing. By melting, they provide a transport mechanism to speed densification. Provided the material to be

sintered is soluble in the liquid phase, a solution-precipitation process allows fast rearrangement of material into a lower energy state. The liquid phase can also assist densification by creating substantial internal capillary pressure; this internal pressure aids in particle rearrangement (improving the particle packing) and increases the pressure between particles (increasing the rate of material transfer). Note that this effect is enhanced when fine size particles are used.

For Si_3N_4, there are many potential sintering aids, though oxides are preferred. These are used with the intent of reacting with the pre-existing oxide layer (SiO_2) on the Si_3N_4 powder surface to form a silicate liquid, and result in a refractory second phase [4]. Common sintering aids are magnesia (MgO), alumina (Al_2O_3), and yttria (Y_2O_3), though the latter two are used often as they have less detrimental effects on the mechanical properties when used in appropriate weight fractions. The sintering aids are chosen to have similar thermal properties to the majority phase, if possible, so that upon heating, thermal expansion mismatch will not cause catastrophic failure of the part, as when one of the phases expands much more than the other phase and the material fractures.

Liquid phase sintering is often used in concert with external applied pressure (hot-pressing, *e.g.*, as discussed later) to decrease further the sintering time and temperature [4]. The liquid phase composition plays a large part, in that the viscosity of the material affects the wetting of the Si_3N_4 particles, since greater wetting leads to greater benefit in that more particles are affected, and the surface tension increases the magnitude of the internal pressure. Further, the final composition of the liquid phase, which forms a grain-

boundary and triple-point phase after cooling, plays a major role in determining the creep behavior of the sintered material.

Pressureless sintering is that in which the green article (ceramic powder compacted with sintering aids) is simply heated in a furnace [4]. This heating is usually carried out in an inert atmosphere to inhibit oxidation of the powders. For Si_3N_4 the atmosphere can also be nitrogen, which would not be harmful to the part. The sintering temperature for Si_3N_4 is about 1750°C, depending on the amount and type of sintering aids, if any, as well as the quality of the Si_3N_4 powder itself [4]. Densities achieved through pressureless liquid phase sintering are generally high, but are not theoretical density (TD). A value of 97% TD or higher can be expected. As the green article can be in the shape and size of the final part (allowing for up to 15% shrinkage associated with the sintering process), this is an economical method, as post-machining is reduced.

Hot pressing (HP) is a process which sinters the green article in concert with application of high pressure [4]. The addition of pressure reduces the sintering time and temperature, while still obtaining near-TD and a fine-grained microstructure, and optimizing strength. Also, hot pressing allows for an overall reduction in the amount of sintering aid, which greatly improves high-temperature properties, including creep. Due to the application of pressure, there is commonly texture of the resulting parts, in that there are elongated grains perpendicular to the pressing direction. This preferred orientation can cause a 20% difference in strength and other properties between the pressing and perpendicular directions. Such materials with a bimodal grain size distribution (that in which two

different grain sizes are present with an insignificant presence of grains of intermediate sizes) are termed *in situ*-reinforced (ISR), as the longer grains in the material function as would reinforcements in a composite material, increasing the strength, fracture toughness and high-temperature creep resistance. The use of hot-pressing can also reduce the amount of sintering aids required, thus allowing for a more pure product. The parts produced by hot-pressing are generally very hard and dense, causing machining difficulties in addition to those due to the texture. Densities of produced parts are often ~100% TD.

Hot isostatic pressing (HIP) is another processing method incorporating application of external pressure to speed the densification process [4]. The ability to apply very high pressures, more than one order of magnitude higher than hot-pressing, enhances the densification. This higher pressure is believed to produce a more uniform microstructure of finer grains. The green article, as with pressureless sintering, can be in the final shape, another advantage over hot-pressing; the green article often experiences about the same amount of shrinkage as in pressureless sintering, reducing post-machining costs. A similar method is gas-pressure sintering, in which a high pressure atmosphere is used, but no preferred orientation results, unlike for HP or HIP. The microstructure produced in the sintered Si_3N_4 resulting from these methods is different from that in which no pressure is applied, and this altered morphology has an effect on the mechanical properties.

Reaction bonding is a process by which silicon powder is consolidated by some method

(slip-casting, *e.g.*), then pre-sintered in an inert atmosphere [4, 9]. The pre-sintering gives strength to the green article so that it can be machined to the desired shape and size for the final part. The part is then nitrided under nitrogen atmosphere at ~1400°C for several days. Thus does the part densify at the same time that Si_3N_4 is formed. Resulting parts have high porosity, and thus have reduced strength compared to parts from other methods.

For nearly all methods of producing dense Si_3N_4, sintering aids are used. Sintering aids reduce the required time and/or temperature necessary to achieve TD. For Si_3N_4, sintering aids assist liquid phase sintering, *i.e.*, the sintering aid melts [4, 8]. The liquid phase assists the mass transport by providing a faster diffusion medium, allowing sintering to proceed faster. For many ceramic systems, including Si_3N_4, the liquid phase is "persistent," meaning that the second phase from the sintering aid remains in the dense final part. This phase usually constitutes a grain boundary phase, being very thin and linking the Si_3N_4 grains. This grain boundary phase (an oxynitride silicate glass, sometimes called a sialon glass (when the composition is of the form SiAlON); the grain boundary phase hereafter may be referred to as oxynitride glass or silicate) has considerable effect on the properties of the final part, especially high-temperature properties. GS-44 is reported to use Al_2O_3, Y_2O_3, and MgO as sintering aids [10]. The grain boundary phase for AS800 has been reported as $Y_{10}Si_7N_4O_{23}$, referred to as the H-Phase, and was found to be approximately 10wt% of the sintered material [11], a relatively typical amount of sintering aid. This seems to indicate that only Y_2O_3 is used for production of AS800; as mentioned earlier, MgO is known to cause poorer high-

temperature creep resistance in Si_3N_4-based ceramics, even when an ISR microstructure results. Thus, it was expected that GS-44 would experience greater creep than AS800. This notion correlates with the earlier development of GS-44, while AS800 is a more recently-produced variety.

1.1.3 Properties and Applications

Silicon nitride has many desirable properties for structural applications, even at high temperature. For turbine components, for example, materials need to possess high strength, low density, high toughness, resistance to corrosion and oxidation, and good creep resistance [7, 12]. Presently, turbine blades are made from nickel-based superalloys. Si_3N_4 is considered a candidate to replace superalloys in this application. The density of Si_3N_4 is less than half that of nickel alloys (3.2 g/cm^3 compared to 8.5 g/cm^3) [7, 12]. Metal alloys can have fracture toughness (K_{IC}) of more than 100 MPa$\sqrt{m}$, while many ceramic materials have K_{IC} of around 1 MPa$\sqrt{m}$. Si_3N_4 has K_{IC} ranging from 4 to as high as 8 MPa$\sqrt{m}$, depending on the processing method [12]. Si_3N_4 has less tendency to oxidize than do nickel alloys above 1000°C, while also having better creep resistance, owing partially to higher melting temperature for Si_3N_4 (actually, Si_3N_4 does not have a melting temperature, *per se*, but it dissociates into Si and N_2 at around 1900°C) as opposed to nickel melting around 1450°C (note that structure and composition also influence this) [7, 12]. (There is a relation between the melting temperature of a material and its creep onset temperature, which is around 0.3-0.4 of the melting temperature for metals, and 0.4 and 0.5 of the melting temperature for ceramic materials [12].) Si_3N_4 has a low thermal expansion coefficient (α, which is the relation

between the amount which a material expands due to a change in temperature) of around 3.6×10^{-6} K^{-1}, while metal alloys often have $\alpha > 10 \times 10^{-6}$ K^{-1} [7]. Thus, for a given temperature change, ceramic components will tend to expand much less than metal components, easing the design allowances. The limitations of nickel-based alloys, in terms of their susceptibility to oxidize and the creep properties, limit their applications in turbines to temperatures below 1000°C [12]. For fuel efficiency reasons, running at hotter temperatures is desirable, thus in addition to the weight reduction (thanks to low density), the improved mechanical properties at high temperature drive the interest in Si_3N_4 as a replacement material in such applications [11, 13].

Table I gives properties for the two grades of Si_3N_4 studied in this thesis, GS-44 and AS800 [14, 15]. While both have the ISR microstructure, AS800 is the more recently developed. Both of these materials are produced by the same manufacturer (Allied Signal, originally, now Honeywell Ceramic Components, Torrance, CA). Note that both have good strength retention at high temperature, with both retaining about 70% of their strength near their respective maximum use temperatures. This is due to improved processing based on characterization of prior Si_3N_4 grades, such as GS-44; these studies determined the effects of sintering aids in terms of chemical composition and amount of additive [16-20].

Often, mechanical properties of Si_3N_4 are affected by the densification method, specifically when an ISR structure is produced. Aided by the application of pressure, using HP, HIP, or gas-pressure sintering, some Si_3N_4 grains elongate and a bi-modal

grain distribution is produced in the sintered material. While the different grain types are the same phase (β-Si_3N_4), there are both elongated ("acicular") and more equi-axed grains present in the final microstructure, as shown in Figure 1 [18, 21]. Surrounding the grains is a grain boundary phase, usually vitreous (*i.e.*, glassy, non-crystalline), produced by the liquid-phase sintering method. Heat treatment can crystallize this phase to improve the creep resistance [22, 23], but this is not typically the case [24].

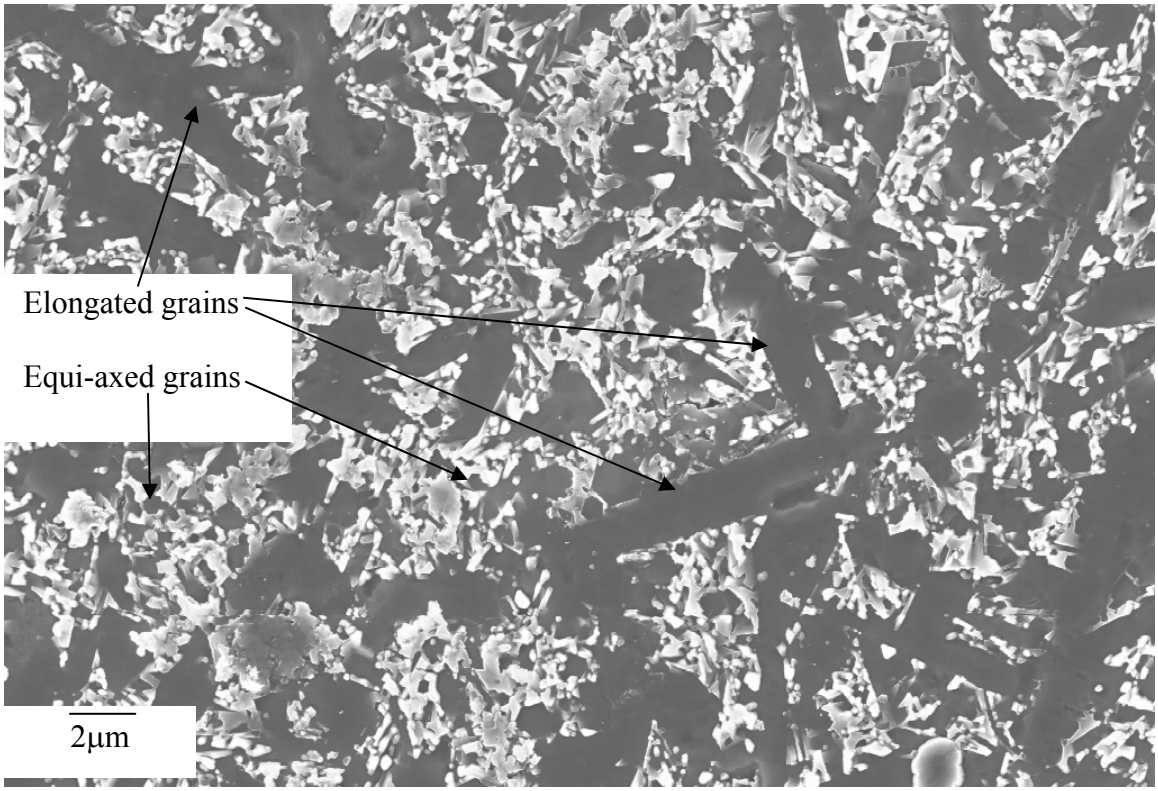

Figure 1. SEM image of the microstructure of as-received GS-44, polished and plasma etched, showing the ISR microstructure of elongated grains and equi-axed grains (dark) in the surrounding grain boundary phase (white).

Table I. Properties of GS-44 and AS800 silicon nitride [14, 15]

	GS-44	**AS800**
Flexural strength (MPa) Room temperature (T = 293 K) High temperature	 977 655 (at T = 1373 K)	 797 580 (at T = 1640 K)
Fracture Toughness (K_{IC}, MPa√m, at 293 K)	8.25	8.1
Hardness (Vickers, 10 kg)	1460	1650
Density (g/cm^3)	3.2	3.3
Coefficient of Thermal Expansion (CTE, 293-1273 K, x10^{-6} K^{-1})	3.4	3.9
Elastic Modulus (GPa) 293 K 1273 K	 300 220	 310 297
Poisson's ratio	-	0.28 (293-1473 K)
Maximum use temperature (K)	1373	1673

1.1.3.1 Creep of ISR Si_3N_4

Creep is time- and temperature-dependent plastic deformation due to an applied constant load. This can happen at room temperature for some materials, but as with Si_3N_4, is often observed for applied load at high temperature.

Si_3N_4, including ISR grades such as GS-44, experiences classical tensile creep behavior, in that there is a fast creep rate regime, followed by a slower regime, and a final fast regime before failure, as shown in Figure 2. These are termed the primary, secondary or steady-state, and tertiary creep regimes. The regime of interest is the steady-state regime, the rate of which is often used to quantify the creep behavior. The steady-state creep rate is an important design consideration for long-life applications in which excessive strain is unacceptable, as with turbine blades; the time to rupture, the time at which fracture occurs due to creep, is also used as a design characteristic [7]. The purpose of creep tests is to gather data regarding the longevity of these materials at the conditions under which they will be utilized. The data are used to compare with models of creep to determine what mechanism allows the creep to occur. In many cases, the nonconformity of the data to an established model has motivated new model construction.

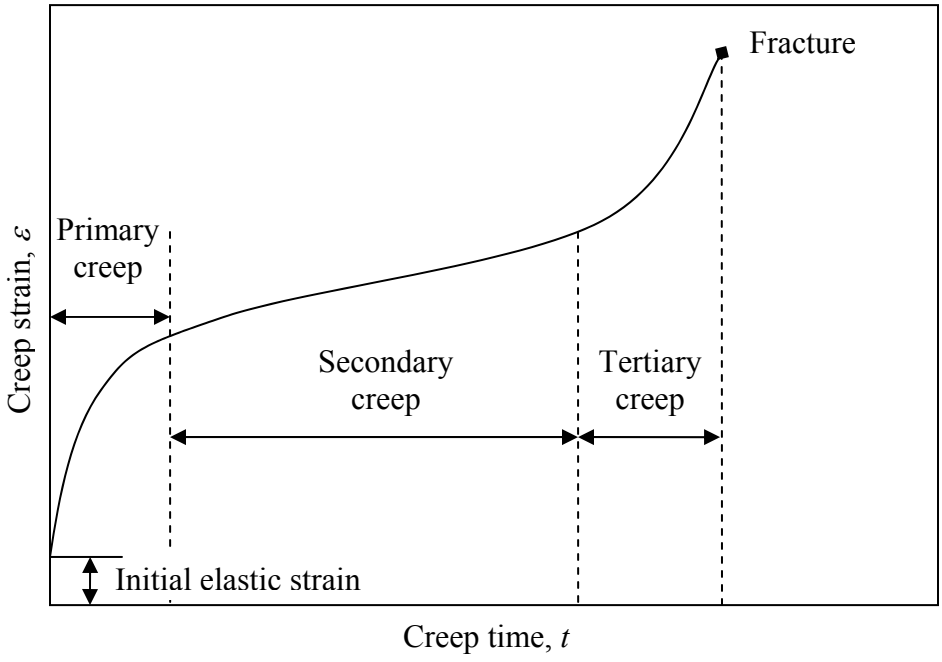

Figure 2. Generalized creep curve, showing the three typical creep regimes.

The steady-state creep rate of metals and ceramics has traditionally been modeled using the Norton equation, shown in Equation (4),

$$\dot{\varepsilon} = \frac{ADGb}{kT}\left(\frac{b}{d}\right)^{p}\left(\frac{\sigma}{G}\right)^{n} \qquad (4)$$

in which σ is the applied stress, D is the diffusion coefficient, G is the shear modulus, b is the Burger's vector, k is the Boltzmann constant, T is the absolute temperature, d is the average grain size, p is the inverse grain exponent, n is the stress exponent, and A is a constant. For cases when the grain size is (assumed) constant and there is no dependence on the presence of the grain boundaries, as with intergranular mechanisms, $p = 0$. When this is not the case, p typically has values from 1-3. Often, Equation (4) is rewritten as Equation (5), combining all the non-stress factors into a single constant, which is valid in that the deformation mechanism should not be dependent upon stress at a given temperature. Thus, the value of p in this case is not a factor. (As will be discussed later, Si_3N_4 creep is grain boundary-controlled, thus $p \geq 1$.)

$$\dot{\varepsilon} = B\sigma^{n} \qquad (5)$$

The stress exponent (also called the creep exponent) is determined using Equation (5) by plotting the logarithm of the steady-state creep rate versus the logarithm of applied stress, for several stresses at a single temperature. The slope of the data in this case is the creep exponent. For Si_3N_4, the creep exponent n ranges from 2-4, with some results reported as high as 16 [3, 10, 25-27]. For GS-44, the creep exponent has been reported as 2.24 by Wei *et al.*[25, 27]. Note that the value of n depends upon the mechanism of creep. For $n = 1$, a diffusion or solution-precipitation mechanism, such as Lifshitz or Rachinger sliding, determines the creep behavior. Lifshitz sliding is that in which the grains

elongate in addition to sliding due to the grain boundary phase, while Rachinger sliding is for grain boundary sliding without grain elongation [27]. These simple cases, however, are not valid for Si_3N_4, since $n \neq 1$. Note that what occurs in Si_3N_4 is similar to Rachinger sliding, in that the sample elongation is attributed to the grain boundary phase, but is aided by the formation of cavities that facilitate the rearrangement of grains and redistribution of stress. Given that the stress exponent is often ~2, recent efforts have attempted to model tensile creep through either an interface reaction-controlled diffusion mechanism, or cavity nucleation in the vitreous grain boundary phase in addition to its viscosity [3, 13, 22, 24, 27-33].

The grain boundary phase is known to be the major factor in the creep of Si_3N_4 at high temperature [2, 10, 22, 24-26, 29, 32, 34]. Depending upon the sintering aids used (composition and amount), the creep behavior is affected. For example, MgO has a degrading effect on the creep behavior (*i.e.*, the creep is more pronounced, greater deformation occurs at a faster rate) compared, *e.g.*, to Y_2O_3 additives. In any case, Si_3N_4 with an acicular grain structure is known to possess greater creep resistance than Si_3N_4 with a uniform equi-axed microstructure; this greater resistance is attributed to the interaction of the grains with one another, in a locking manner, as rearrangement occurs due to creep and flow of the grain boundary phase.

Creep studies of ISR Si_3N_4 indicate creep exponents of n = 1.5-4, with values of n = 2-2.5 being typical [3, 10, 25, 26]. Such a value indicates that diffusion is not the dominant creep mechanism (which would have n = 1), when there is no grain size influence. The

stress exponent *n* is determined by plotting on a log-log plot the steady-state creep rate for multiple stresses at a single temperature. The data are usually linear, with the slope being *n*. Various mechanisms have been proposed to account for the creep mechanism of ISR Si_3N_4, including grain boundary sliding, and solution-precipitation of Si_3N_4 in the grain boundary phase, though the non-Newtonian nature of the flow of the grain boundary phase is often noted as the primary determinant of the creep behavior [22, 24, 29, 32].

Standard creep tests are performed in air, which accurately simulates the service environment for Si_3N_4. However, this allows ambient oxygen to decrease the viscosity of the grain boundary phase, thus allowing creep to proceed faster [2, 23, 35]. The viscosity of the grain boundary phase plays a significant role. In oxynitride glasses such as the silicate glass grain boundary phase, the higher the nitrogen to oxygen ratio, the higher the viscosity. Given that most creep tests take place in air, oxygen is available to diffuse into the grain boundary phase, and as a result decrease its viscosity [3, 23]. This leads to a faster creep rate. A creep test in vacuum or inert atmosphere would limit this effect [36], and would be a more accurate measure of both the creep of Si_3N_4 and the inherent properties of the grain boundary phase.

From tensile creep experiments of an ISR Si_3N_4, Gasdaska noted that the high creep exponent and large creep activation energy precluded a diffusion mechanism from the major creep determinant. The conditions of those tests also eliminated dislocations as the major factor, as he verified with post-test TEM imaging. Gasdaska concluded that, while cavitation was likely a factor in the creep behavior, that it was not the cause of the high

creep exponents. However, he drew a correlation between the stress dependence of the ISR Si_3N_4 creep and the non-Newtonian flow of silicate glasses. Given that the grain boundary phase was such a glass, Gasdaska developed a model for the steady-state creep strain rate. The model was developed assuming that, as stress is applied at high temperature, the grain boundary phase softens, allowing grain boundaries to slide due to the grain boundary viscosity at that stress and temperature; this sliding of grain boundaries was attributed for the primary creep behavior. This leads to a steady-state creep rate when there are sufficient mechanisms within the grain boundary phase to accommodate the sliding of grain boundaries, including cavitation and flow. Building upon work by Eyring regarding fluid viscosity Gasdaska's equation, which better approximates creep behavior than Norton's equation (Equation (4)), is shown in Equation (6) (for stresses greater than 50 MPa) [22].

$$\dot{\varepsilon} = A_s T \exp\left(\frac{-\Delta H_s + \Omega_s \sigma}{RT}\right) \qquad (6)$$

In this model, ΔH_s and Ω_s are the apparent activation energy and activation volume, respectively, R is the universal gas constant, A_s is a pre-exponential constant, and T is the absolute temperature. Activation energies for various temperatures were comparable to that for viscous flow in glasses, supporting this formulation.

Luecke and Wiederhorn developed a model for tensile creep of ISR Si_3N_4 based on general observations of the creep behavior, including the formation of cavities in the grain boundary phase as the primary source of creep strain, the inactivity of dislocations, and the curvature of plotted tensile creep data. Cavities have been reported after TEM investigations of crept samples [3, 22, 32]. These cavities form in multi-grain junctions.

From this information, they inferred that diffusion mechanisms were not responsible for the accumulation of tensile creep strain, but that a rearrangement of the rigid grains in the microstructure facilitates the creep, requiring the grain network to dilate. The increase of cavity volume fraction with creep strain indicated that the tensile creep depends heavily on that cavitation. They assumed three possible rate-limiting steps in the tensile creep: nucleation of cavities, grain boundary sliding during the microstructural dilation, and flow of the grain boundary phase away from a nucleated cavity. Noting that the cavitation of the grain boundary phase from tensile creep does not affect a volumetric expansion, but only contributes to the elongation, they assumed that the volume change was equal to the creep strain. Due to the low creep exponent for Si_3N_4 they demonstrated that cavity nucleation was not the rate-limiting step. They further eliminated grain boundary sliding as the possible rate-limiting step, as the predicted flow rate was much faster than that observed in Si_3N_4; thus the non-linear viscosity of the grain boundary phase did not explain the exponential relation of the tensile creep rate due to the applied stress.

Thus, Luecke and Wiederhorn assumed that the redistribution of the grain boundary phase was the limiting step. From this they derived a model based on the assumption that the axial strain during creep is equal to the volume fraction of cavities that have been nucleated in the grain boundary phase. They further assumed an Arrhenius relation with temperature for the grain boundary viscosity [22, 24, 32]. Their resultant creep equation is shown in Equation (7),

$$\dot{\varepsilon} = A\sigma \exp\left(\frac{-\Delta H}{RT}\right)\frac{f^3}{(1-f)^2}\exp(\alpha\sigma) \qquad (7)$$

in which f is the volume fraction of second phase, α is a constant incorporating the critical stress to nucleate a cavity, and the other terms are as before. This formula includes terms for the dependence of the steady-state creep rate on the applied stress, and the effective viscosity and volume fraction of the grain boundary phase. The temperature dependence of the creep rate is preserved by the Arrhenius form of the viscosity. They demonstrated that this equation matched the curvature of creep data plotted on a semi-log basis for various ISR silicon nitrides.

The creep mechanism of ISR Si_3N_4 remains undetermined in that experts cannot agree on the nature of the creep, despite numerous creep studies on different grades; however, it is certain that the creep depends heavily upon the grain boundary phase, its viscosity and the cavities that are nucleated within it. Based upon the creep exponent, some possible mechanisms have been ruled out, while new models have been developed in efforts to provide predictive power for these materials. What is lacking in the creep literature is an *in situ* microstructural study. There have been investigations of the microstructure of ISR Si_3N_4 using SEM and TEM, but the images are only comparisons of pre- and post-crept samples. While this shows the effects of creep on the microstructure, there is no knowledge of what occurred *in situ* during creep. This absence of an *in situ* microstructural study is due simply to a lack of suitable equipment. Given the high temperature required for creep of ISR Si_3N_4, actual imaging of the microstructure is impossible. At present, only a diffraction method can provide bulk microstructural information *in situ* while applying mechanical stress at high temperature. This study was undertaken in an effort to perform a creep test as have other researchers, at like

temperatures and stresses, while collecting neutron diffraction data. Since Luecke and Wiederhorn indicate that Si_3N_4 stays elastic while the grain boundary phase flows, diffraction data should be measurable, since diffraction is capable of obtaining only elastic strains. It was intended that the creep mechanism might be deduced based on effects of creep noted in the diffraction patterns, including but not limited to, peak broadening, changes in preferred orientation (evident as changes in relative intensity of diffraction peaks), and/or peak position changes indicating internal strain.

II. Experimental Methods

2.1. Neutron Diffraction

Neutron diffraction was applied in the latter half of the twentieth century for the study of materials. The following is a brief summary of the technique as applied for this thesis and is not intended as a full technical review.

The demonstration that crystal structures diffract neutrons first occurred in 1936 [37]. However, it was not until the development of nuclear reactors, and the incumbent production of sufficient neutrons to allow collimation into a beam as well as control of neutron wavelength, that the technique of neutron diffraction was "born." Nuclear reactors became sources of monochromatic (single wavelength) neutrons, and are still used thusly today; however, such reactor sources have several shortcomings, including long data collection times which limit data collection to a select few peaks for time-sensitive experiments. The desire for faster and more comprehensive data collection led to the development of the time-of-flight (TOF) method of neutron diffraction [37].

Monochromatic neutron diffraction obeys the same Bragg's Law of diffraction as X-rays (save that neutrons diffract from atomic nuclei rather than orbiting electrons), see Equation (8), in which λ is the neutron wavelength, d is the spacing between planes parallel to the diffracting crystal (often referred to as d-spacing), and θ is the incident diffraction angle (equal to the diffracted angle), all of which are shown schematically in Figure 3 [37-39].

$$\lambda = 2d \sin\theta \qquad (8)$$

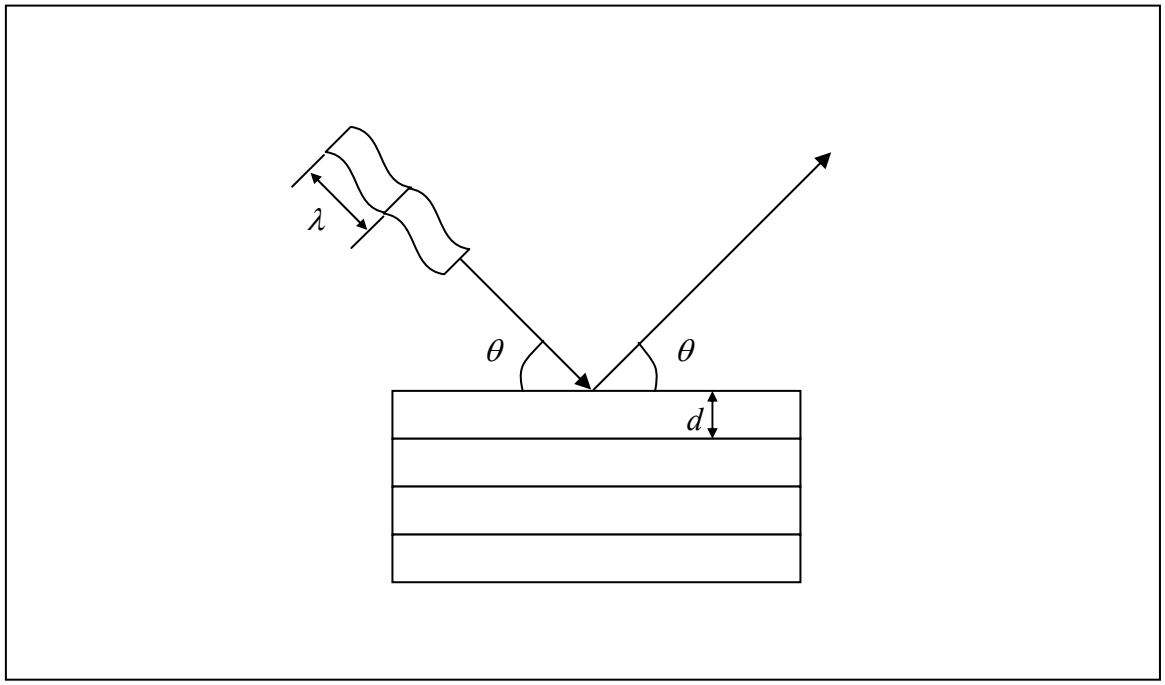

Figure 3. Idealized schematic of concept of neutron diffraction, with relevant parameters for Bragg's Law indicated.

Basically, a beam of neutrons strikes a sample and is diffracted from the crystal planes within the sample. For each crystal plane of different orientation (or composition or structure for multi-phasic materials) within a polycrystalline sample, the neutron beam will require a different angle to diffract and be detected. Thus, for a single wavelength neutron source, the incident angle (and thus diffraction angle) is altered by rotating the sample with respect to the incident beam, which itself cannot move and always admits the beam from the same direction. Thus, for the case of monochromatic diffraction, the only unknown is d, while λ is fixed and known, and θ is known but varied and controlled.

TOF diffraction, however, due to the presence of multiple wavelengths of neutrons cannot make use of Equation (8) directly, since one needs first determine the wavelength of the neutron which is detected. Modern spallation neutron sources create neutrons by sending pulses of protons at a heavy element target, which when hit by the proton beam, emits neutrons of random wavelength in random directions. This neutron production method is called spallation. A neutron spectrometer uses a beam guide to channel neutrons form the source to the sample, collimating the beam and eliminating very fast and very slow neutrons. The time of flight is simply the time from creation of the neutron by the proton pulse hitting the target until the neutron is detected after diffracting from the sample [37, 40]. Once the TOF is known, Bragg's Law, Equation (8), can be modified into Equation (9). This modification makes use of the neutron wavelength dependence on the velocity of the neutron, *i.e.*, $\lambda=h/mv$, where m is the neutron mass, h is Planck's constant, and v is the neutron velocity. Also needed is the simple relation between velocity and time, namely $v = L/t$, where L is the distance from the neutron source to the detector (termed the "flight path"), and t is the time that the neutron takes to traverse L. Also, with the use of multiple wavelengths, sample motion is no longer necessary, thus θ is fixed in TOF neutron diffraction. Since the times are known (determined from the time passed between neutron creation and detection), the unknown is again d.

$$t = \frac{2mL\sin\theta}{h}d \qquad (9)$$

Neutron diffraction, much like other diffraction methods, can be used for elastic lattice strain measurement [39, 41]. It is well known that the strain of a particular crystal is

evident from a change in the *d*-spacing measured with diffraction. The same relation holds true for the TOF method. The general methodology for strain determination is discussed in the Section II (Experimental Procedure).

While TOF ND is often applied for engineering analyses, there are a number of specific test methods that have not lent themselves well to integration with diffraction. X-ray diffraction requires small beam sizes to give high-resolution information, and even with high-energy X-rays (as from a synchrotron), typically only small sample sizes can be tested. While such tests do provide essential information, engineering materials are rarely used in very small sizes. Thus there is ambiguity as to whether the information provided from micro-diffraction measurements scales with, and allows predictive modeling of, large samples. Neutron diffraction, however, being fundamentally different, allows for diffraction from larger size samples than X-rays, at least as regards diffraction from the volume and not the surface. Nonetheless, some mechanical tests are still in their infancy as regards mating with diffraction, *e.g.*, high-temperature creep studies, in which the literature contains no studies over 1000°C.

Tests involving application of mechanical stress are numerous, and have been used to study a myriad of materials, using both X-rays and neutrons. There have also been a number of high-temperature experiments, again with both X-rays and neutrons, for measuring such things as thermal expansion and phase changes. However, there is a dearth of literature combining the two, as for creep studies. Winand *et al.* [42], and Madgwick *et al.* [43], performed tests on particulate-reinforced aluminum-matrix

composites at low temperatures (270-320°C) using TOF ND. Winand *et al.* [42], used diffraction pattern collection times of 25-30 minutes, noting the typical lack of increased elastic diffraction strain during primary and steady-state creep. Madgwick *et al.* [43], determined the creep rates for comparison to models, concluding that the effective creep exponent of the composite was less than that of the matrix material under steady-state conditions, contrary to prior findings. Madgwick *et al*. [44], studied creep of an A359/SiC composite at 300°C using single wavelength neutron diffraction, noting only elastic strains. They related the degradation of room temperature properties of crept specimens to damage induced by creep. Daymond *et al.* [45], examined a Mo-reinforced Cu matrix alloy using TOF ND up to 350°C. They compared their data to finite element models, and found some agreement between predictions and observations. Choo *et al.* performed heating experiments with TOF ND to measure the CTE and internal strain evolution up to 1170 K of a Ti-SiC composite, with no stress application [46, 47]. While they presented data on internal strain evolution from two phases, the CTE data presented was for GSAS-refined lattice parameters only, with no tensorial quantities detailed. Rangaswamy *et al.*, measured the residual strain with TOF ND and compared the results to finite element model predictions and residual strains measured by X-ray diffraction [48]. Latella *et al*., studied the liquid phase sintering of alumina ceramic compacts up to 1400°C, but these were using reactor source, single wavelength neutrons, with count times as long as 2 hours for a single pattern [49]. Note that there have been no TOF ND experiments studying creep at temperatures greater than 1000°C. This type of experiment requires two things: first, a sample that can survive high temperatures and is intended for use under such conditions, and second, a facility to perform the

experiment. Until recently, there has been no such apparatus for performing creep at high temperature.

2.2. SMARTS

The new SMARTS neutron spectrometer at the Los Alamos Neutron Science Center, however, is such an instrument, and was developed specifically to carry out such tests through an integrally-designed load frame-furnace setup [50, 51]. As silicon nitride is a high-temperature material, and has been the subject of numerous creep studies of which none used neutron diffraction *in situ*, the SMARTS spectrometer was chosen to perform this line of research.

The SMARTS diffractometer has available a high-capacity (250 kN) load frame (Instron) that can mate with a high-temperature (1600°C) furnace (MRF), shown assembled in the photograph from the SMARTS cave Figure 4. Hot rods are of a refractory metal (W-10wt% Th). The furnace elements (TaW) are susceptible to oxidation, and thus failure, so samples are heated only in vacuum. Figure 5 shows the inside of the furnace, with the hot rods, furnace elements, and a mounted sample with attached sample thermocouples, while Figure 6 shows the sample as viewed through the sight glass at temperature, in which the controller thermocouple is visible. The vacuum level is always kept below $5x10^{-2}$ torr. While this ensures the furnace functions safely, there are effects of testing a sample in a vacuum. The furnace center coincides with the center of diffraction for the diffractometer. An aluminum (Al) window allows the incident neutron beam to reach the sample with minimal loss. Similarly, Al windows allow diffracted neutrons to exit the furnace [50].

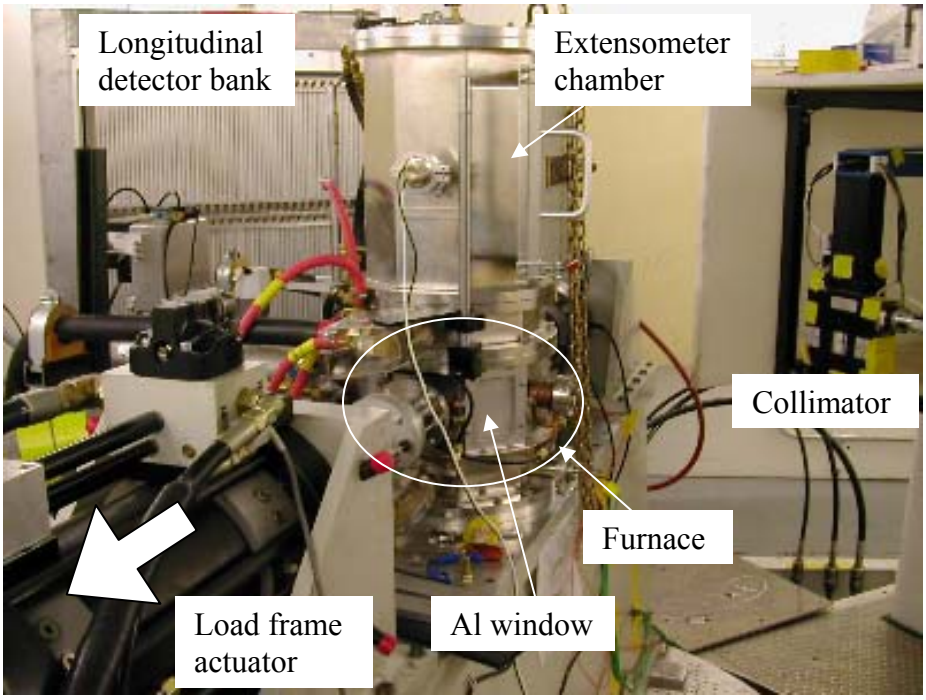

Figure 4. Photograph from inside the SMARTS cave with labeled points of interest. The load frame and furnace are assembled together. The longitudinal detector bank is visible in the background. For diffraction pattern collection, the collimator is moved nearly into contact with the entrance Al window (not shown) of the furnace.

SMARTS is a time-of-flight (TOF) neutron diffractometer. A standard material (CaF_2), for which the diffraction pattern is well-characterized, is used to calibrate the diffractometer and determine the proper "time-focusing" necessary to reconstruct the diffraction pattern from the detected neutrons. An instrument parameter file is generated on the basis of the CaF_2 pattern, and this pattern is used for preparation ("binning") of all diffraction data. Since the detector banks cover a range of angles, but data are given as though detected at only $\pm 90^\circ$ 2θ, a calculation is performed within the binning program

to account for this effect. The exact time-focusing is determined with the use of the standard material.

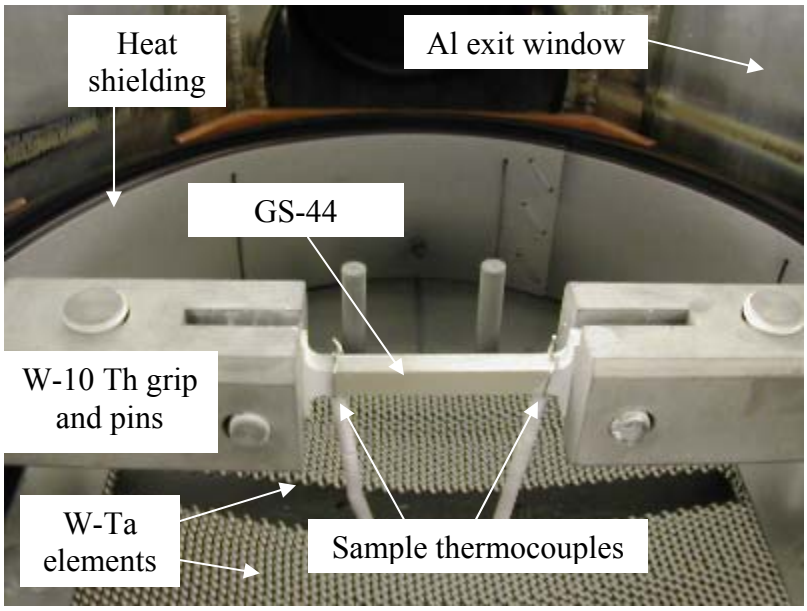

Figure 5. Photograph of the inside of the SMARTS furnace, with a GS-44 sample mounted in the W-10Th grips.

Diffracted neutrons are detected by one of two detector banks. Each bank consists of 144 ^{3}He tubes, in three rows of 48, in which each tube is aligned vertically. These banks are parallel to the incident beam on opposite sides of the sample. The furnace and frame are aligned at 45° to the incident beam, thus the detector banks are at Bragg angles of ±90° 2θ (actually, the detector tubes cover approximately ±75-105°, with time-focusing to 90°) [50]. These angles allow for collection of neutrons that diffract from grains whose crystal planes are aligned along the sample axis (-90°) and perpendicular to the sample axis (+90°); these two directions give longitudinal and transverse diffraction data,

respectively (see Figure 7). The TOF method with this detector arrangement allows the diffraction patterns for both directions to be collected simultaneously and in relatively short times.

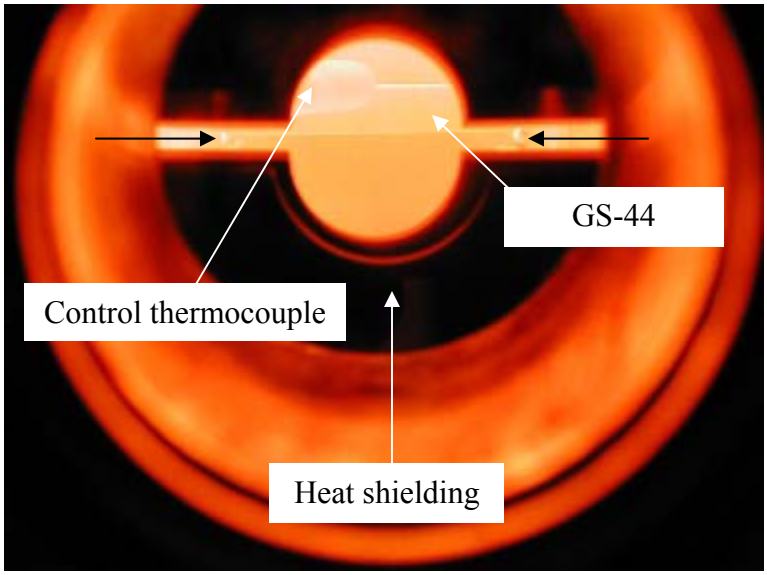

Figure 6. Photograph of a GS-44 sample at temperature, viewed through the sight glass on the SMARTS furnace. The control thermocouple is shown in relation to the sample, which was shown in the furnace in Figure 5. The two unlabeled arrows indicate the beads of the sample thermocouples in contact with the sample.

Diffraction data for Si_3N_4 was collected on the SMARTS diffractometer at the Los Alamos Neutron Science Center (Los Alamos National Laboratory, Los Alamos, NM). For this study, typical data collection times for a quality diffraction pattern (such that GSAS pattern fitting residuals were reduced, typically under 10%) were 15-30 minutes (though actual data collection sometimes took longer for room temperature experiments, for which there was less concern about inelastic effects since Si_3N_4 is elastic at room

temperature). The SMARTS data collection system allows for automated data collection in either a specified time or a specified neutron count. For high-temperature work, especially creep experiments, time resolution is of greater import, so a time-specific data collection routine was employed whereby single patterns were collected for the time mentioned above, with different collection times for different samples. Room temperature experiments were completed on the basis of total neutron counts, rather than time; 170,000 monitor counts was determined as sufficient to result in diffraction patterns which were fit by GSAS with under 5% fitting residuals in some cases.

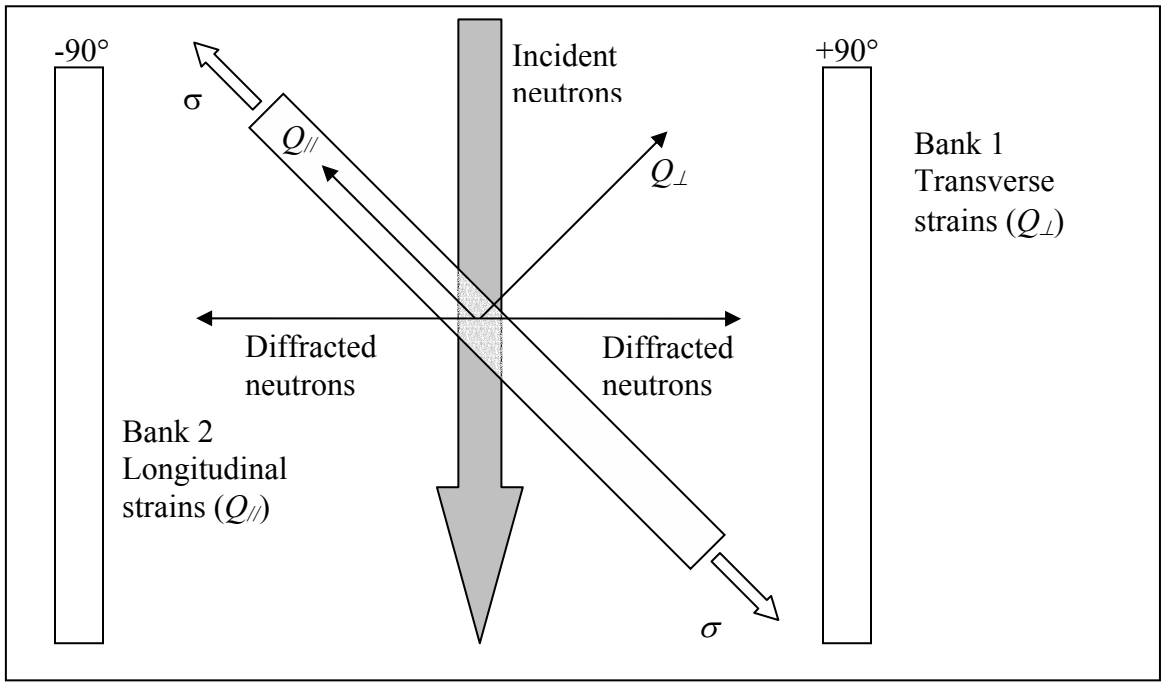

Figure 7. Time-of-flight neutron diffraction schematic. $Q_{\perp}$ and $Q_{//}$ are the diffraction vectors, indicating the orientation of crystal planes from which the diffracted neutrons originate, either those perpendicular to (transverse strains) or those parallel to (longitudinal strains) the loading direction, which is indicated as σ.

2.2.1. Mechanical Test Methodology

The SMARTS load frame is of horizontal orientation, as shown in Figure 5. This geometry requires that a tensile stress be applied to the pin-loaded dog-bone sample (shown in Figure 8) to keep it in the correct position for diffraction. Without an applied stress, the sample sags away from the ideal position for diffraction. By applying the tensile stress, the sag due to gravity is compensated for. In addition, if the sample is allowed to sag, it will lose contact with the high-temperature extensometer. The SiC-bladed extensometer is placed in contact with the top surface of the sample gage section. The extensometer has a spring to reduce any vertical position fluctuation, but this is only effective in a short range. Should the sample sag, due either to gravity inadequately compensated for or to sample fracture, the macroscopic strain data from the extensometer would be lost, eliminating the ability to compare the diffraction strains to any other measurement.

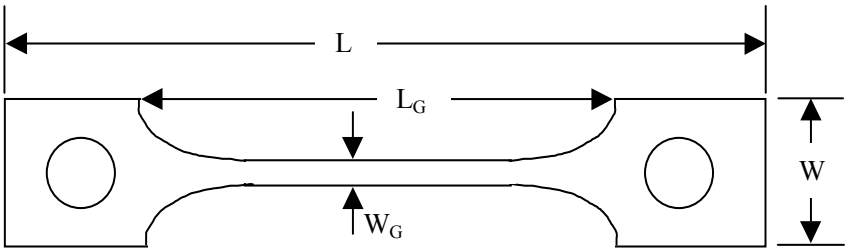

Figure 8. Schematic of tensile specimen. Approximate dimensions were: L = 89 mm, L_G = 51 mm, W = 19 mm, W_G = 6.3 mm. The sample thickness was 5.0 mm unless otherwise noted for individual samples.

2.2.2. High Temperature and Applied Stress

For room temperature experiments, since time was deemed less important as the

deformation was expected to be fully elastic, a larger number of stress levels were applied in order to obtain an accurate measure of the mechanical response. The increment in stress was typically 10 MPa, though initial load increases fluctuated depending upon the starting stress, while the decrement in stress level from the maximum was typically 25 MPa. Samples were loaded to a maximum stress of 150 MPa. If different stresses were applied to a sample, it will be noted in the discussion for that sample.

High-temperature experiments collected diffraction patterns at fewer stress levels. This is because of the importance of reaching the maximum stress for that experiment in as short a time as possible. Since at the test temperature, creep was expected to occur for increased stress, minimizing that stress was necessary for the load-up procedure. Typically, diffraction patterns were collected for every 25 MPa of stress, up to the maximum for that experiment. Upon reaching the desired stress, the load was held constant while diffraction patterns were collected in succession. At the end of creep experiments, the stress was reduced quickly to the initial stress level (that needed at room temperature to hold the sample in the diffraction position) for creep recovery, during which diffraction patterns again were collected in succession. Eventually, the furnace was cooled back to room temperature, and one or more (nearly) room temperature diffraction patterns were collected before the sample was removed.

2.3. Heating Experiments

For early experiments with each type of Si_3N_4 studied, the heating portion of the experiment was not carried out in a single step. Rather, the furnace temperature was set

to intermediate values and the system was allowed to equilibrate. Such temperature equilibration was determined by observing a lack of strain increase in the extensometer data, corresponding to a cessation of thermal expansion. Thermal expansion is that change in dimension (length change is often measured) which occurs in a material due to a change in temperature. The coefficient of thermal expansion (CTE), α, is the relation between the temperature change and the resulting dimensional change. When the thermal expansion is plotted versus temperature, for many materials the slope of the data is linear, the value of which is α with units of inverse temperature (K^{-1}). When measuring a single dimension, the determined CTE is called the linear CTE (as opposed to the volumetric CTE from measuring the volume change due to a temperature change), and generally conforms to the relation shown in Equation (10), in which l_0 is the initial length, Δl the change in length, and ΔT the temperature change.

$$\frac{\Delta l}{l_0} = \alpha \ \Delta T \qquad (10)$$

For Si_3N_4, the measured thermal expansion was for the length of the material, so the CTEs reported are linear CTEs. After thermal expansion had completed, a diffraction pattern was obtained from the sample. Typical temperature increments were 200 K. The patterns from these scans were used to determine the CTE from full diffraction pattern fits (see Section 2.4). Single peak fits to reflections in these patterns were used to calculate the CTE tensor, a mode shown by Jessen and Küppers to be of greater validity [52]. Jessen and Küppers showed that of the two methods, one determining the lattice parameters from thermal expansion from diffraction data, then using the result to determine the CTE tensor required extraneous computations, and a series of propagated

errors reduced the precision of the obtained CTE tensor. Essentially, by fitting the entire pattern the *hkl*-anisotropy of the structure can be lost in the resulting lattice parameters due to the averaging of the full-pattern fit. For non-cubic materials, the CTE anisotropy is not reflected properly in the full-pattern-derived lattice parameters. Jessen and Küppers found that by obtaining information from at least six different *hkl*s for the temperature range of interest, and using the *d*-spacing of those reflections directly to refine the CTE tensor via a least-squares method, preserved the *hkl*-behavior and resulted in greater precision of the CTE tensor. Only by refining the behavior for individual reflections are errors minimized. They demonstrated this reduction of accuracy for two different triclinic materials, finding that the direct CTE tensor determination method was of great precision by at least a factor of 2 compared to the CTE tensor results based on lattice parameters. The errors are introduced when the experimental error of the *d*-spacing (due to factors that affect diffraction pattern accuracy, for example, absorption or displacement error) is incorporated into the determination of the lattice parameters. This error is propagated when using these refined lattice parameters in turn to refine the CTE tensor. If there were no such propagation of errors, then the two methods would yield tensor components of the same precision, but they do not. The method and computer program (ALPHA) of Jessen and Küppers were used for CTE tensor computation from the *d*-spacing of individual *hkl* reflections [52].

2.4 Mechanical Loading (Elasticity and Creep)

For high-temperature experiments, upon reaching the test temperature, the stress on the sample was increased incrementally to the desired test stress. At each stress level, a diffraction pattern was obtained. Based upon the very small extensometer strain increase

over time for each of these load levels, the sample was considered still to be in the elastic strain regime, and calculation of the elastic properties (modulus and stiffness tensor depending upon sample) proceeded; this procedure was successful for AS800 but unsuccessful for GS-44–a likely indicator that despite relatively small changes in strain over time for GS-44, the sample was not completely elastic. The stress level was then maintained while diffraction patterns were collected over time. Some early experiments with GS-44 were stress-jump tests, a method shown to allow for calculation of the creep exponent. This technique subjects a single sample to multiple stresses at a single temperature. Creep is allowed to occur at that stress, and the slop of the steady-state creep for each stress is determined. These data are plotted as creep rate versus stress on a log-log plot, and a linear fit is applied. The slope of the linear fit (if indeed the data *are* linear) is the creep exponent.

2.5 Data Analysis

Diffraction patterns were analyzed using the GSAS program [53]. This program uses a least square refinement (the Rietveld method) to fit the diffraction data [54]. Phase information, including space group ($P6_3/m$), atomic types and positions, and lattice parameters (a = 7.608 Å, c = 2.911 Å) were input [55]. These were refined along with the background function (six term), scale factor, peak profile coefficients, absorption factor, and atomic thermal parameter (Debye-Waller factor). Each refinement was repeated until convergence was achieved, indicating that further variation of these parameters could no longer improve the fit. The fitted values were then used to determine the lattice strains from the lattice parameters, according to Equation (11). Strains were determined separately for the two lattice parameters of Si_3N_4.

$$\varepsilon_a = \frac{a - a_0}{a_0} \qquad (11a)$$

$$\varepsilon_c = \frac{c - c_0}{c_0} \qquad (11b)$$

The values for a_0 and c_0 varied depending upon the calculation being made. They were the lattice parameters for the initial room temperature pattern for CTE calculations, while for creep calculations they were the first pattern acquired at high temperature; one single value sufficed as the reference lattice parameter value (a_0 or c_0) for all the strains in that particular calculation; the particular data used as for these strain reference values is identified for each analysis set. Strains were plotted versus temperature (for CTE purposes), stress (for elastic loading data), or time (for creep data). Note that strains are typically plotted as microstrain (με), which is simply, *e.g.*, $10^6 * \varepsilon_a$. Also, an overall strain ε_d, was calculated with the same formalism as in Equation (11), where d replaces a or c and d_0 replaces a_0 or c_0, and d is found using Equation (12).

$$d = \frac{2a + c}{3} \qquad (12)$$

This quantity d is used here for convenience only, as something of a polycrystalline average d-spacing.

Single peak fits, using the Voigt peak profile, were also carried out with the GSAS program, though only the Rawplot module was used. Nine different reflections were fit for both bank 1 and bank 2. Strains were determined as for full pattern fits as discussed above (see Equation (11)), though for single peak fits, the d-spacing of an individual peak was used rather than an averaged lattice parameter. These strains were plotted in the

same manner as the full pattern GSAS fits described previously. In addition, some of the single peak fit data were used to determine *hkl*-specific properties. First, single peak fit data from diffraction patterns were used to determine the CTE tensor [52, 56]. Subsequent calculation indicated the degree of anisotropy, A (also called the aspherism index) for the material based on the tensor components, determined by Equation (13), the equation for A for hexagonal crystals. A purely isotropic CTE will give A=0 [57].

$$A = \frac{2}{3}\left|\frac{\alpha_{11} - \alpha_{33}}{2\alpha_{11} + \alpha_{33}}\right| \qquad (13)$$

The components of the CTE tensor are the α_{ij} shown in Equation (13). Note that the *11* axis corresponds to the *a*-axis of β-Si_3N_4, while the *33* axis corresponds to the *c*-axis. Thus, when comparing the tensor results to those from full-pattern refinements, α_{11} is compared to a, and α_{33} to c. Single peak fits of diffraction patterns from mechanical loading experiments were used to attempt refinement of the stiffness tensor for the sample. Often, systematic errors prevented obtaining the tensor, but the high-temperature stiffness tensor for AS800 was determined in this manner.

For mechanical loading experiments, both full-pattern fits and single peak fits were used to determine properties. By plotting the diffraction strains versus applied stress, average mechanical properties were determined. The slope of a linear fit to the longitudinal strain data yielded the Young's modulus, E. The ratio of slopes to linear fits to both the longitudinal and transverse diffraction strains yielded the Poisson's ratio, ν. In some cases, the diffraction data from multiple patterns at a given stress and temperature were averaged in order to improve the statistics. This was only performed when there was

little variation between the patterns, thus indicating a lack of inelastic effects. For high-temperature applied stress, this lack of inelastic behavior is necessary for determination of elastic properties, since plastic deformation (*i.e.*, creep) is more easily induced at elevated temperature. Before a stiffness tensor could be determined, this lack of elasticity was ascertained first.

There has been past success using elastic-plastic self-consistent (EPSC) polycrystal deformation models for predicting diffraction elastic constants (DECs, the elastic constants derived from the stress-strain behavior of lattice reflections measured by diffraction) for several materials [58-61], requiring only the input of single crystal stiffnesses for the given material. However, for silicon nitride, there is an absence of high-temperature stiffness data. Thus, a reversed calculation was performed using the measured DECs and a least squares fitting routine to obtain the best fit for the single crystal stiffnesses for AS800. The starting point for the calculation was the isotropic stiffness tensor obtained from the measured macroscopic DECs (the Young's modulus, E, and Poisson's ratio, ν) determined using full-pattern GSAS fits to stress-strain data from 1648 K diffraction data for AS800. For this starting tensor, the tensor components were determined as shown in Equations (14)-(16).

$$C_{12} = \lambda = \frac{\upsilon E}{(1+\upsilon)(1-2\upsilon)} \tag{14}$$

$$C_{44} = G = \frac{E}{2(1+\upsilon)} \tag{15}$$

$$C_{11} = \lambda + 2\upsilon \tag{16}$$

In these equations, G is the shear modulus, λ is a Lamé constant, E is the Young's modulus, and ν is the Poisson's ratio. For isotropic materials, the elastic stiffness tensor only has two independent components, since $C_{11} = C_{22} = C_{33}$ and $C_{12} = C_{13} = C_{23}$; note that $(C_{11} - C_{12}) = 2C_{44}$, and that $C_{44} = C_{55} = C_{66}$. The data were insufficient to allow this refinement, in that the tensor components were possessed of greater error bars, so, in the case of multiple patterns (when several patterns were collected for a particular applied stress), data were summed into a single pattern. Then, strains from single peak fits for nine reflections were used to refine the stiffness tensor by attempting to match the *hkl* stress-strain behavior. As mentioned, this method was successful for AS800 at 1648 K, and the resulting values were compared to literature values for room temperature elastic stiffness. After the tensor was refined, the macroscopic Young's modulus and Poisson's ratio were determined from the tensor components by solving Equations (15) and (16) simultaneously. However, the refinement was not possible for GS-44, likely due to some inelastic effects due to loading, despite the precaution of reducing the time at each applied stress.

While there is a lack of literature data for elevated temperature stiffness tensors for materials, there has been some prior work to determine the room temperature stiffness of Si_3N_4. Vogelgesang *et al*., determined the stiffness tensor of this material (Si_3N_4) using single crystal β-Si_3N_4 samples [62]. It was desired to compare the Young's moduli determined from linear fits to single peak strains to an expected value based on literature. The easiest method was to determine the *hkl*-dependent elastic properties using s_1 and s_2, which relate to the Young's modulus, E, and Poisson's ratio, ν (see Equations (16) and

(17)). Gnaupel-Herold *et al.*, developed a program to calculate s_1 and s_2 for a given crystal system (hexagonal for β-Si_3N_4) for any *hkl* [63]. This program assumes that all grains are spherical and embedded in an isotropic matrix, with grain-grain interactions allowed, which is neither the Voigt approach (which assumes constant strain in all grains) nor the Reuss approach (which assumes constant stress in all grains), but an adaptation of the Kröner approach; this approach gives greater accuracy than the typically good agreement obtained from the average of the Voigt and Reuss methods, which can account for grain shape as well as grain interactions within the isotropic matrix [63]. The stiffness tensor of the material must be input, as well as the crystal system of the material and the lattice parameter(s). The program then calculates s_1 and s_2, from which E_{hkl} and ν_{hkl} were determined by solving Equations (17) and (18) simultaneously, to compare with those values from diffraction data.

$$s_1(hkl) = \frac{\upsilon_{hkl}}{E_{hkl}} \qquad (17)$$

$$\frac{1}{2}s_2(hkl) = \frac{1+\upsilon_{hkl}}{E_{hkl}} \qquad (18)$$

For determining s_1 and s_2 with the Gnaupel-Herold program, the tensor of Vogelgesang *et al.* [62], was used for the stiffness tensor of Si_3N_4. The lattice parameters were those that were refined for the Si_3N_4 (either GS-44 or AS800) under consideration. Note that the Vogelgesang *et al.* [62], tensor was determined from a room temperature measurement of a single crystal and would not represent accurately the high-temperature polycrystal material being tested here. Similarly, the calculated 1648 K AS800 stiffness tensor was used to acquire s_1 and s_2 for comparison. Though the AS800 tensor was for that grade at

1648 K, and the Vogelgesang *et al*. [62], tensor for single crystals at room temperature, this effort was intended for order-of-magnitude level comparison with both AS800 and GS-44. The lattice parameters used were the initial room temperature lattice parameters from GSAS. This prediction of *hkl*-dependent properties was compared with the results from diffraction data. Comparison was hindered when the single peak stress-strain data behaved non-linearly, as one might expect, even for the AS800 predictions compared with the AS800 data.

2.6 Microscopy

Scanning electron microscopy (SEM) was used to image the grain morphology of the Si_3N_4 samples tested in various experiments. First, the samples were cut with a diamond saw in the middle of the gage section (where the diffraction data originated). The surface was polished using established materialographic procedures [64]. The polished surfaces were then sectioned off, again with a diamond saw. The polished surfaces were plasma etched to reveal the microstructure. Plasma etching has been determined to be the optimum etching method for Si_3N_4 [64]. Specifically, the sample was etched using chemical assisted ion beam etching (CAIBE). CAIBE was carried out with the settings in Table II, using a Kaufman-type ion source, Xe as the background gas, and Cl to etch. The etched samples were carbon coated then imaged in a field emission SEM (LEO 1550VP, LEO Electron Microscopy, Inc., Thornwood, NY). The samples had to be carbon coated, since Si_3N_4 is a semiconductor and charging of the samples prevented imaging otherwise. The accelerating voltage of the electron beam was 10 keV. Images were obtained from

both the untested material and samples tested at high temperature on SMARTS for comparison.

Table II. CAIBE conditions

Filament current	3.24 A
Discharge current	0.21 A
Discharge voltage	40.0 V
Beam current	17 mA
Beam voltage	750 eV
Accelerator current	2 mA
Accelerator voltage	120 V
Neutralizer emission current	9 mA
Neutralizer filament current	2.98 A

2.7 Ultrasonic Elastic Modulus Measurement

The elastic modulus of untested samples and samples tested on SMARTS were measured using an ultrasonic technique. In this technique, a sonic wave was input to the sample surface with a transducer (V112 10 MHz normal transducer and V156 5 MHz shear transducer, both manufactured by Parametrics, Waltham, MA), and an oscilloscope recorded the reflection of that sound wave. The samples tested were those from creep experiments, with the dimensions indicated in Figure 8, unless otherwise noted when the results are discussed. Two reflections were observed, one from the normal transducer and the other from the shear transducer. Each sample was tested at two locations, one

near the middle of the gage section, and the other region near the grip. Only one result is reported, as the results were the same for the two regions. These observations gave V_L and V_S, respectively, the velocity of the wave in that sample. The wave velocities and the sample density ρ were used to determine the elastic modulus *E* and shear modulus *G* as follows.

$$G = \rho\left(V_S\right)^2 \qquad (19)$$

$$E = \rho\left(V_S\right)^2\left(\frac{3-4\left(\frac{V_S}{V_L}\right)^2}{1-\left(\frac{V_S}{V_L}\right)^2}\right) \qquad (20)$$

The Poisson's ratio υ is related to *E* and *G* according to Equation (21), a simple rearrangement of Equation (15).

$$\nu = \left(\frac{E}{2G}\right) - 1 \qquad (21)$$

The density ρ used in these calculations was the manufacturer quoted density (see Table I). Results of these calculations were compared to literature values and to experimental data (both diffraction and extensometer when possible). Note that Equation (21) is a relation for isotropic materials. While Si_3N_4 is not isotropic, from a macroscopic point of view it is assumed to be isotropic, and this method is effective in providing a boundary value for these elastic constants.

III. Results and Discussion

3.1 AS800

Several AS800 samples were tested. The experiments performed on AS800 are summarized in Table III. Significant data were collected from AS800, it being the first ISR Si_3N_4 to be tested. New data include both the CTE tensor for 298-1648 K, and the 1648 K elastic stiffness tensor. Subsequent room temperature experiments were aimed at obtaining similar data to the 1648 K experiment with which to determine the effect of temperature on mechanical properties. Diffraction patterns (see Figure 9 for an AS800 pattern) contain only peaks from β-Si_3N_4, indicating either that the grain boundary phase remained vitreous, or that crystallization was an insufficient fraction to appear in the patterns. The exact amount of secondary phase is unknown, but ranges from 6-12 wt%. Typically, a crystalline phase will not appear if it is less than 2wt% of the material, depending on its neutron scattering power, which does not increase with an element's atomic number as does X-ray scattering.

Table III. AS800 experiments

CTE	**High-Temperature Loading**	**Room Temperature Loading**	**Date**
Yes	Yes	No	December 2001
No	No	Yes	October 2002
No	No	Yes	September 2003

3.1.1. CTE data

The CTE of AS800 was determined from diffraction data. The sample was held under a 30 MPa stress to ensure it was in the center of diffraction of the SMARTS furnace.

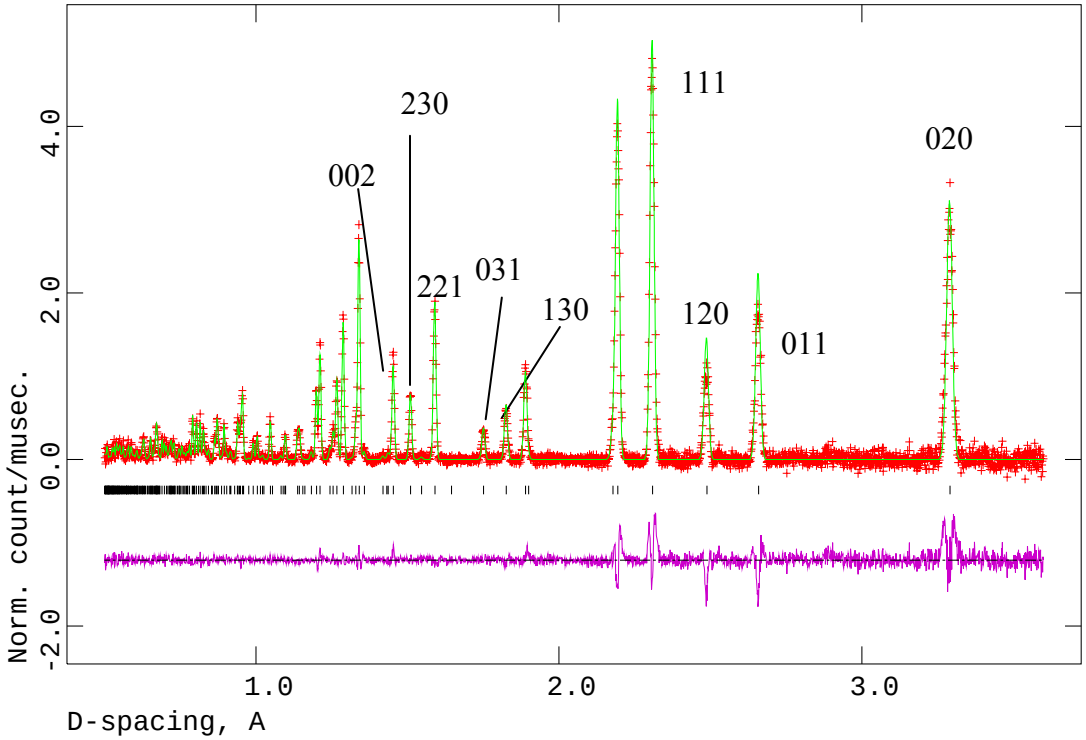

Figure 9. Diffraction pattern for AS800 at 298 K, 25 MPa. Labeled peaks are those fit singly.

Diffraction patterns were obtained at room temperature (298 K), and at isotherms of 473, 773, 1073, 1373 and 1648 K. The furnace was heated at 20 K/min after each pattern was acquired, until the test temperature of 1648 K was reached. After reaching each isotherm, diffraction patterns were not acquired until the extensometer reached a constant value. Strains were calculated using Equations (11) and (12); the room temperature diffraction data was the strain reference for thermal expansion. Multiple patterns were

collected at each isotherm. Plotted strains are the average of the strains from each isotherm.

The measured thermal expansion is plotted in Figure 10 for longitudinal diffraction data (bank 2). Though not shown, the transverse (bank 1) thermal expansion diffraction data were similar, while the longitudinal data are plotted as they are an appropriate comparison to the similarly oriented extensometer. Included in Figure 10 are the diffraction data for both the *a* and *c* lattice parameters, the polycrystalline average *d*, the extensometer thermal expansion measurement, and the calculations from the program ALPHA [52]. The plotted results for ALPHA are similar to the polycrystalline average, in which the two independent CTE tensor components are used to determine the average CTE value according to Equation (22).

$$\alpha_{\text{avg}} = \frac{2\alpha_{11} + \alpha_{33}}{3} \qquad (22)$$

CTE results for all the plotted quantities are summarized in Table IV. The ALPHA calculation was based on the strains from single peak fits of the following *hkl*s: (02·0), (01·1), (12·0), (11·1), (13·0), (03·1), (22·1), (23·0), and (00·2). Data used were from the initial and final temperatures to give a single value for the entire thermal expansion (as opposed to using each isotherm to give a piecewise CTE for the full temperature interval). The CTE tensor resulting from these single peak data is given in Equation (23). These tensor components are the α_{ij} used in Equation (22) to obtain α_{avg} (see Table IV).

$$\alpha = \begin{pmatrix} 3.50 \pm 0.03 & 0 & 0 \\ 0 & 3.50 \pm 0.03 & 0 \\ 0 & 0 & 4.06 \pm 0.04 \end{pmatrix} \times 10^{-6} K^{-1} \qquad (23)$$

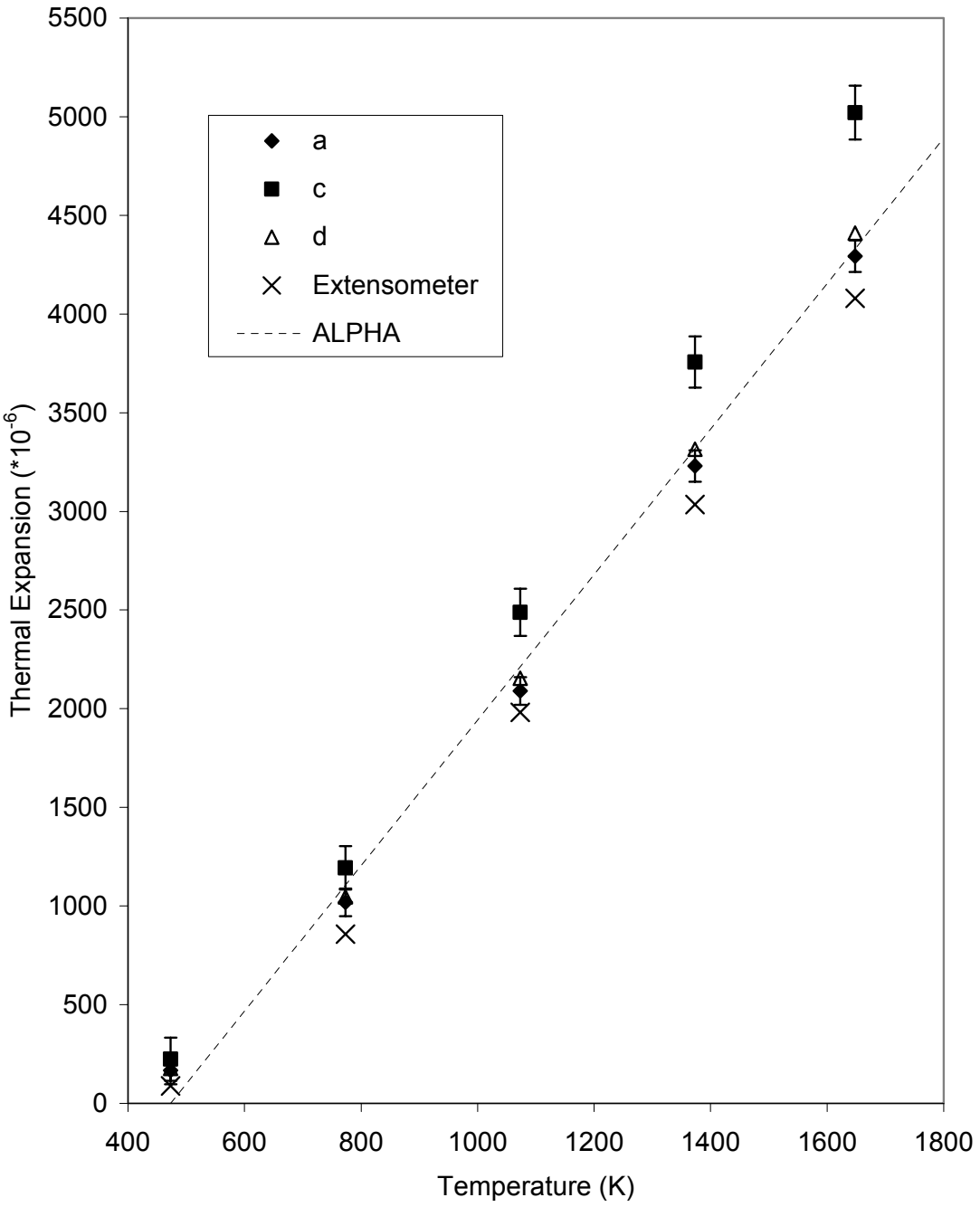

Figure 10. Thermal expansion of AS800 based on SMARTS measurements. Error bars are for GSAS fitting residuals to the lattice parameters.

Table IV. CTE values for lattice parameters (*a, c* and *d*), ALPHA (α_{avg}), all from longitudinal diffraction strains, and the extensometer, as shown in Figure 10.

Parameter	**CTE (*10^{-6} K^{-1})**
a	3.54
c	4.12
d	3.64
α_{avg}	3.69
Extensometer	3.44

Table V. CTE of individual reflections shown in Figure 11 for both longitudinal and transverse diffraction data. CTE values are based on linear fits to single peak thermal expansion strains, with r^2 for linear fits given in parentheses. All values are *10^{-6} K^{-1}.

hkl	**CTE (longitudinal)**	**CTE (transverse)**
(02·0)	3.24 (0.99)	3.20 (0.99)
(01·1)	3.75 (0.99)	3.65 (0.98)
(12·0)	3.38 (0.99)	3.19 (0.98)
(11·1)	3.58 (0.99)	3.51 (0.99)
(13·0)	3.29 (0.99)	3.22 (0.98)
(03·1)	3.46 (0.98)	3.44 (0.99)
(22·1)	3.42 (0.99)	3.39 (0.98)
(23·0)	3.31 (0.99)	3.20 (0.98)
(00·2)	3.82 (0.99)	3.73 (0.98)

The errors in the CTE tensor are fitting errors from the least-squared refinement of the ALPHA program. Single peak CTE behavior is shown in Figure 11 for all nine reflections, while individual *hkl* thermal expansions for both detector banks are given in Table V. (Note that error bars are not shown in Figure 11, as the data point overlap eliminates the clarity of error bars. However, strain errors range from 40-300 με, varying for *hkl* and detector bank.) As shown in Figure 10 and Figure 11 and Tables IV and V, the *c*-axis of AS800 experiences a greater thermal expansion than the *a*-axis. Note, as shown in Table V, that the greatest CTE is for the purely *c*-axis (00·2) reflection. The (01·1) reflection has the next highest CTE, and it also has the highest *c*-character of the remaining eight reflections, while those reflections with zero *c*-character, namely, (02·0), (12·0), (13·0) and (23·0), have the lowest CTE. Mixed *hkl* reflections, *e.g.*, (11·1), have intermediate CTEs. The aspherism index, computed from Equation (13) using the tensor components of Equation (22), is $A = 0.034$. Given that the CTE is anisotropic, and that this material is manufactured at high temperature, it is clear that upon cooling the material will shrink in a non-isotropic manner, causing some residual strain which may be alleviated, in part, by the grain boundary phase.

3.1.2. High-Temperature Stress Application

After heating AS800 to 1648 K and collecting thermal expansion data, the stress on the sample was increased incrementally. Applied stresses, in addition to the initial 30 MPa, were 50-175 MPa, in 25 MPa steps. At each stress, 2-4 diffraction patterns were collected. The applied stress was decreased, collecting patterns at 125 and 75 MPa, finally returning to the initial 30 MPa. During stress increase, the extensometer ceased

functioning, thus there is no macroscopic data to compare with the diffraction strains hereafter presented.

Figure 12 shows the diffraction strains ε_d as a function of applied stress at 1648 K. Note the linear behavior for both longitudinal and transverse strains. The strain reference for these data was the 30 MPa (initial stress) data at 1648 K; essentially thermal expansion strain has been subtracted. The error bars shown are computed as per Equation (12) but using *a* and *c* strain *errors* instead of strains. A linear fit to the longitudinal data gave the Young's modulus as E_d = 339 GPa. The Poisson's ratio was determined from the negative ratio of the longitudinal data slope to the transverse data slope (giving the negative ratio of the transverse and longitudinal strains) as ν_d = 0.32. Note that the literature values (Table I) for these parameters are 310 GPa at 298 K (297 GPa at 1273 K) and 0.28 (up to 1473 K), respectively.

It is uncertain why the measured mechanical properties showed an increase with increased temperature, though it might be due to diffraction strain error. More likely, however, is the lack of information from the grain boundary phase. Only Si_3N_4 was sampled in these experiments, thus only Si_3N_4 strains were measured. The degradation of properties noted in literature [14, 15], as with the effect on creep resistance, must be attributed to the grain boundary phase. This loading occurred in vacuum rather than air, unlike typical mechanical tests. It is known that the grain boundary phase of ISR Si_3N_4 experiences a viscosity decrease at high temperature aided by oxygen, a decrease inhibited here by lack of oxygen. Clearly, the mechanical properties of AS800 should degrade with temperature. Unfortunately, there is no extensometer data for comparison.

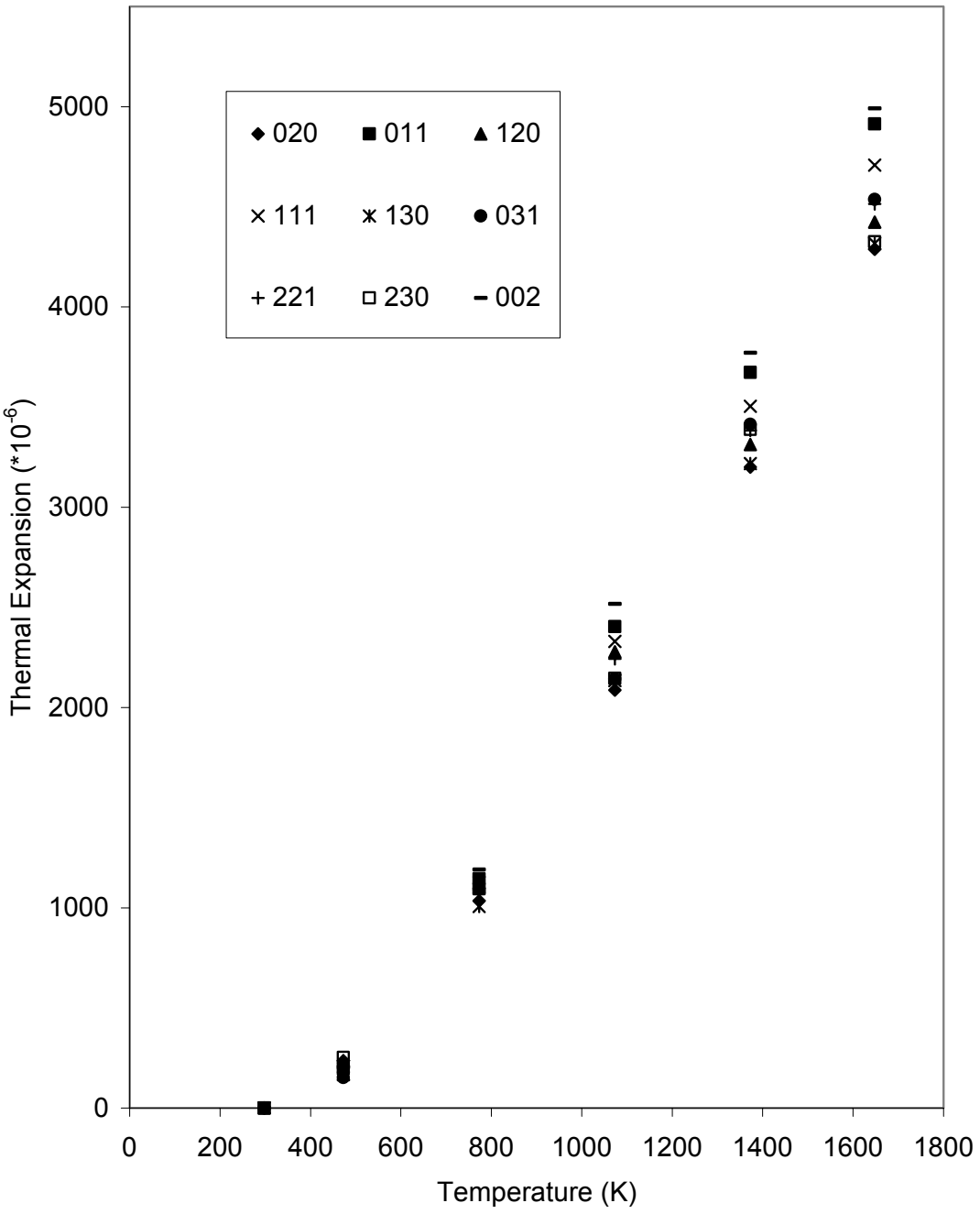

Figure 11. Single peak thermal expansion diffraction data for AS800. Note that reflections with a c-axis component experience greater thermal expansion, also indicated in Figure 10.

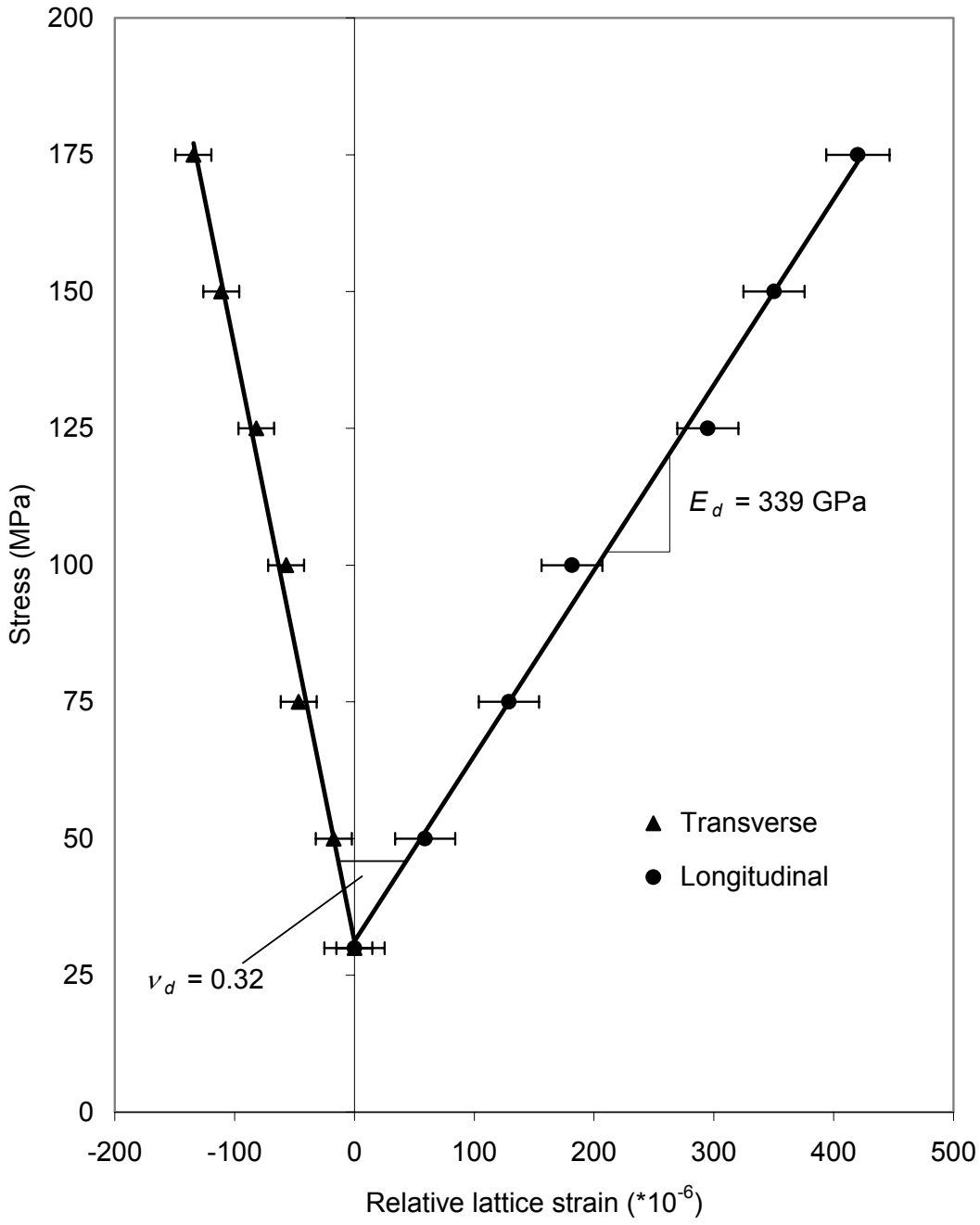

Figure 12. Applied stress versus diffraction strain ε_d for AS800 at 1648 K. Young's modulus, E_d, and Poisson's ratio, ν_d, are indicated with the linear fits used to determine them. Error bars are from fitting residuals of the GSAS-determined lattice parameters.

As with CTE calculations, mechanical anisotropy was assumed intrinsic to the AS800 system. Figure 13 and Figure 14 show the GSAS results for *a* and *c* lattice strains, respectively. Note the large difference between the two elastic moduli, with E_a = 359 GPa and E_c = 257 GPa. The Poisson's ratios of the two lattice parameters are similar, though, at 0.31 and 0.33 for ν_a and ν_c, respectively.

When examining individual reflections, there is little non-linearity of diffraction strains, within the fitting error, as with the full pattern fit-derived *a* and *c* lattice parameters. Since the single peak method is known to be more accurate than the averaging effect of the GSAS full-pattern fits for CTE calculations, the same should hold true for elastic strain calculation (for the same reason of propagation of errors in using lattice parameters for calculating strain versus determining strain from individual reflections first).

Strains are shown in Figure 15 for selected reflections, for longitudinal and transverse strains, while Figures A1-A9 in the Appendix show stress-strain data for both directions for all nine reflections fit as single peaks. Table VI gives the properties determined from Figures A1-A9 based on linear fits. Numbers in parentheses for *E* are the r^2 values from linear fits to the longitudinal data, while the numbers in parentheses for ν are the r^2 values for the linear fits to the transverse data. A value of r^2 = 1 would be a perfect fit, with greater difference indicating greater non-linearity. Note the poor linear fit for the transverse strain of (03·1) and the resulting unrealistic value ($\nu > 1$) for the Poisson's ratio.

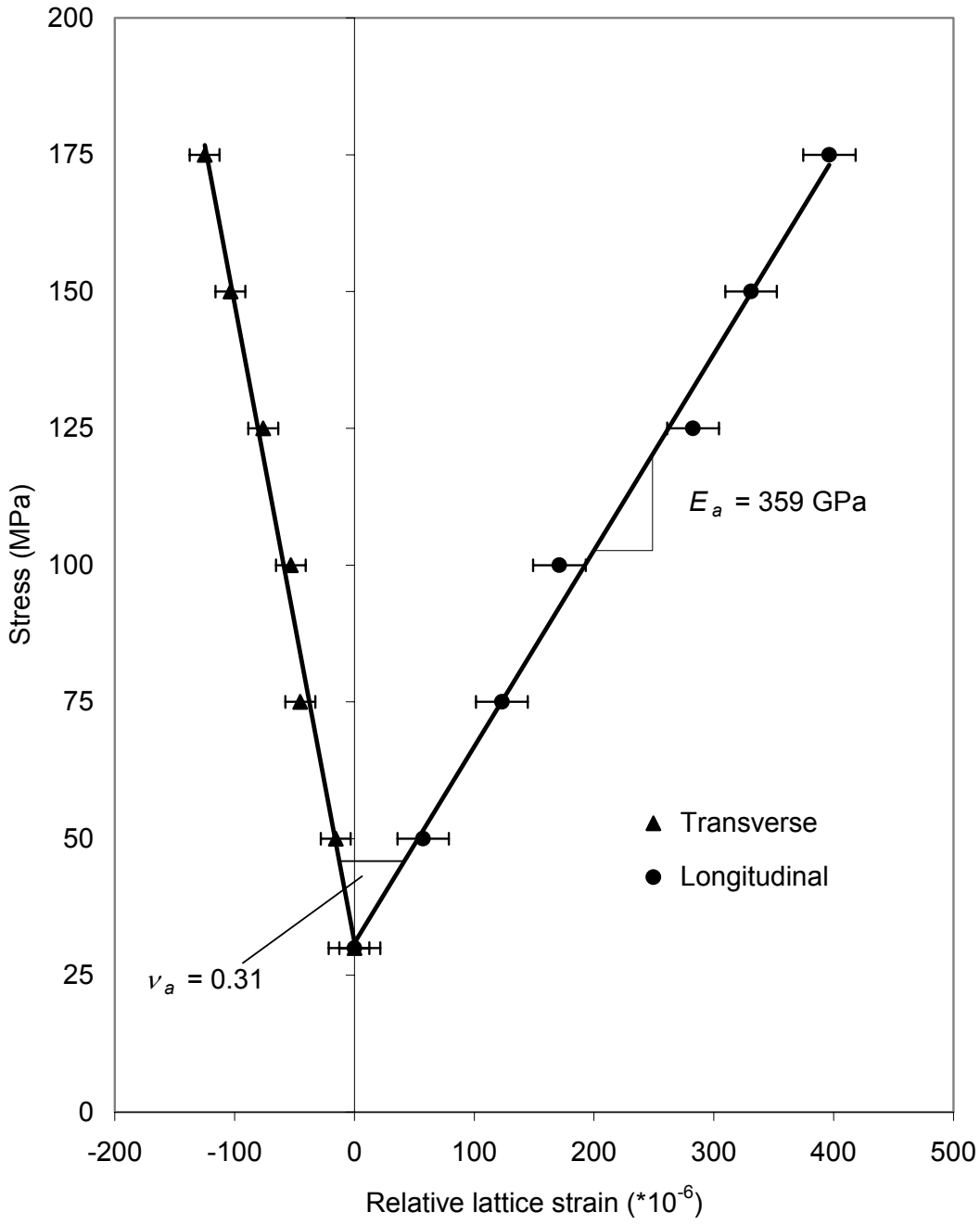

Figure 13. Applied stress versus diffraction strain ε_a for AS800 at 1648 K. Young's modulus, E_a, and Poisson's ratio, ν_a, are indicated with the linear fits used to determine them. Error bars are from fitting residuals of the GSAS-determined lattice parameter.

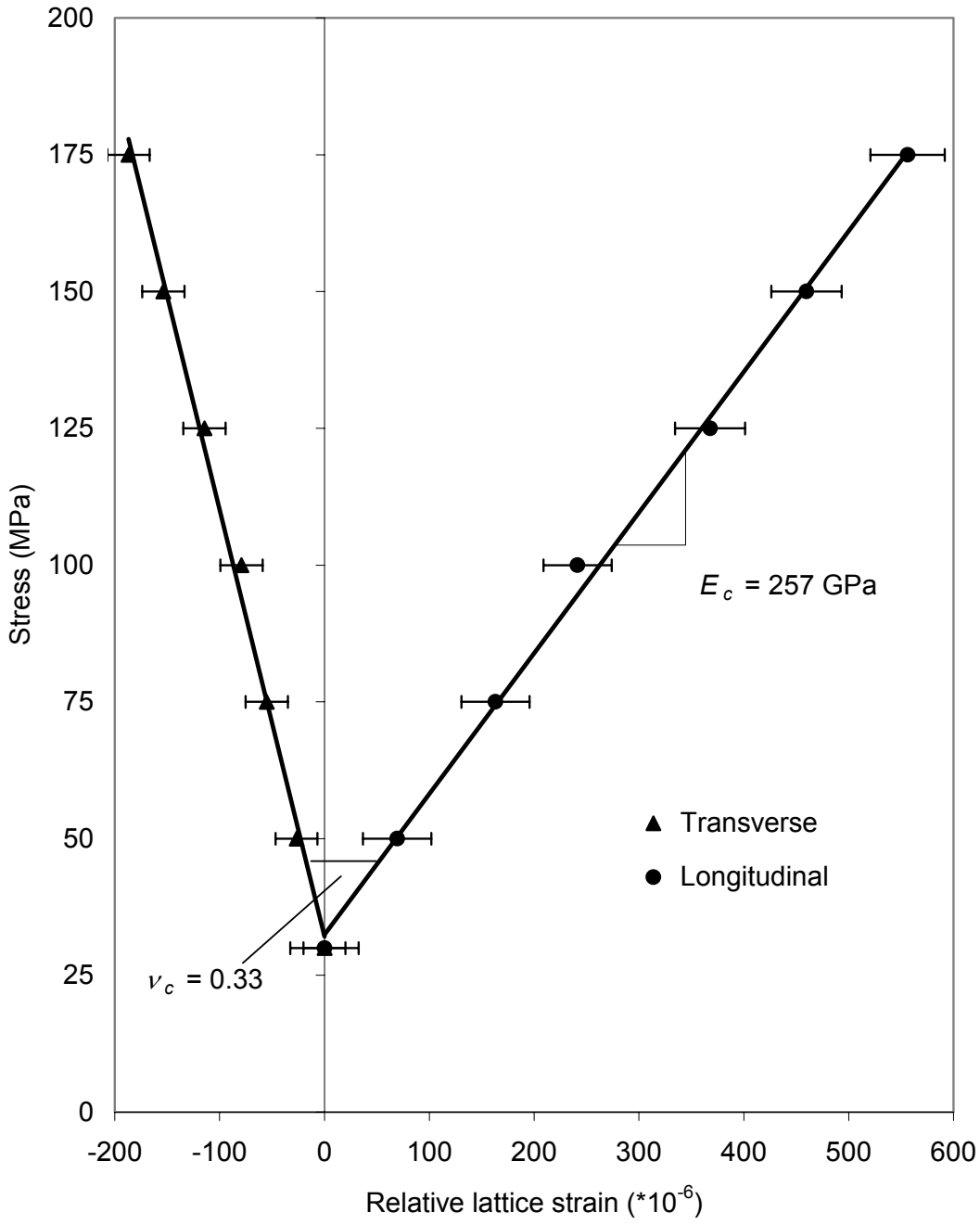

Figure 14. Applied stress versus diffraction strain ε_c for AS800 at 1648 K. Young's modulus, E_c, and Poisson's ratio, ν_c, are indicated with the linear fits used to determine them. Error bars are from fitting residuals of the GSAS-determined lattice parameter.

Table VI. Elastic constants for specific *hkl* reflections for AS800 from diffraction data, E given in units of GPa. E is presented for linear fits to diffraction data (first two columns), and is compared to predicted values using the AS800 tensor of Equation (24) and the tensor from [62].

hkl	***E* (long. fit r^2)**	***E* [62] (% diff)**	***E*, Eqn (24) (% diff)**	**ν (trans. fit r^2)**	**ν [62] (% diff)**	**ν, Eqn (24) (% diff)**
(02·0)	252 (0.98)	312 (19)	336 (25)	0.302 (0.86)	0.275 (10)	0.327 (7.7)
(01·1)	200 (0.93)	261 (23)	368 (47)	0.278 (0.91)	0.279 (0.3)	0.323 (14)
(12·0)	292 (0.89)	312 (6.3)	336 (13)	0.460 (0.89)	0.275 (67)	0.327 (41)
(11·1)	304 (0.99)	305 (0.4)	330 (7.8)	0.339 (0.98)	0.296 (14)	0.302 (12)
(13·0)	297 (0.92)	312 (4.7)	336 (12)	0.475 (0.89)	0.275 (73)	0.327 (45)
(03·1)	312 (0.83)	339 (8.0)	313 (0.2)	1.080 (0.04)	0.300 (260)	0.294 (268)
(22·1)	317 (0.97)	341 (6.9)	313 (1.4)	0.288 (0.99)	0.298 (3.4)	0.296 (2.7)
(23·0)	333 (0.99)	312 (6.9)	336 (0.8)	0.332 (0.94)	0.275 (21)	0.327 (1.5)
(00·2)	226 (0.98)	225 (0.6)	426 (47)	0.373 (0.98)	0.250 (49)	0.342 (9.0)

Also shown in Table VI are the predicted results for the Young's modulus and Poisson's ratio based on the stiffness tensor of Vogelgesang *et al.*, and for the AS800 stiffness tensor of Equation (24), using the program of Gnaupel-Herold *et al*., to get s_1 and s_2, and

solving Equations (17) and (18) for E_{hkl} and ν_{hkl}. It is not unexpected that the AS800 tensor predictions closely match the data from which they were obtained, but it is important to note that the predicted values from the literature room temperature tensor data of Vogelgesang *et al*. [62], are also in good agreement with these high-temperature measurements. Single peaks with less linear behavior do not match the predicted values, while the better the linear fit, the better the agreement with the prediction.

There is no clear trend to note regarding the *hkl*-effect on elastic modulus. The least stiff *hkl* is the (01·1), which has mixed *a*- and *c*-character. The second-least stiff *hkl* is the (00·2) reflection, while the (02·0) is third-least, with regards to longitudinal strains, despite (00·2) being purely *c*-axis and (02·0) purely *a*-axis, with both having comparable quality linear fits. However, the (00·2) Poisson ratio is greater than for (02·0). The (23·0) reflection has the highest Young's modulus *and* a high Poisson's ratio, while the (11·1) is comparable. However, the lack of literature values prevents any meaningful comparison of these data.

The single peak strains were used as described in the experimental procedure for refining the stiffness tensor. The starting point for the refinement was the full-pattern fit results for E_d and ν_d. For simplicity, the initial starting tensor was generated from these values as though for an isotropic material. In this case, with E_d = 339 GPa and ν_d = 0.32, the starting tensor values were $C_{11} = C_{22} = C_{33}$ = 485 GPa, $C_{12} = C_{13} = C_{23}$ = 228 GPa, and $C_{44} = C_{55} = C_{66}$ = 128 GPa using Equations (14) - (16). This starting tensor was used in the EPSC method solving the inverse problem. The EPSC method uses an Eshelby-type

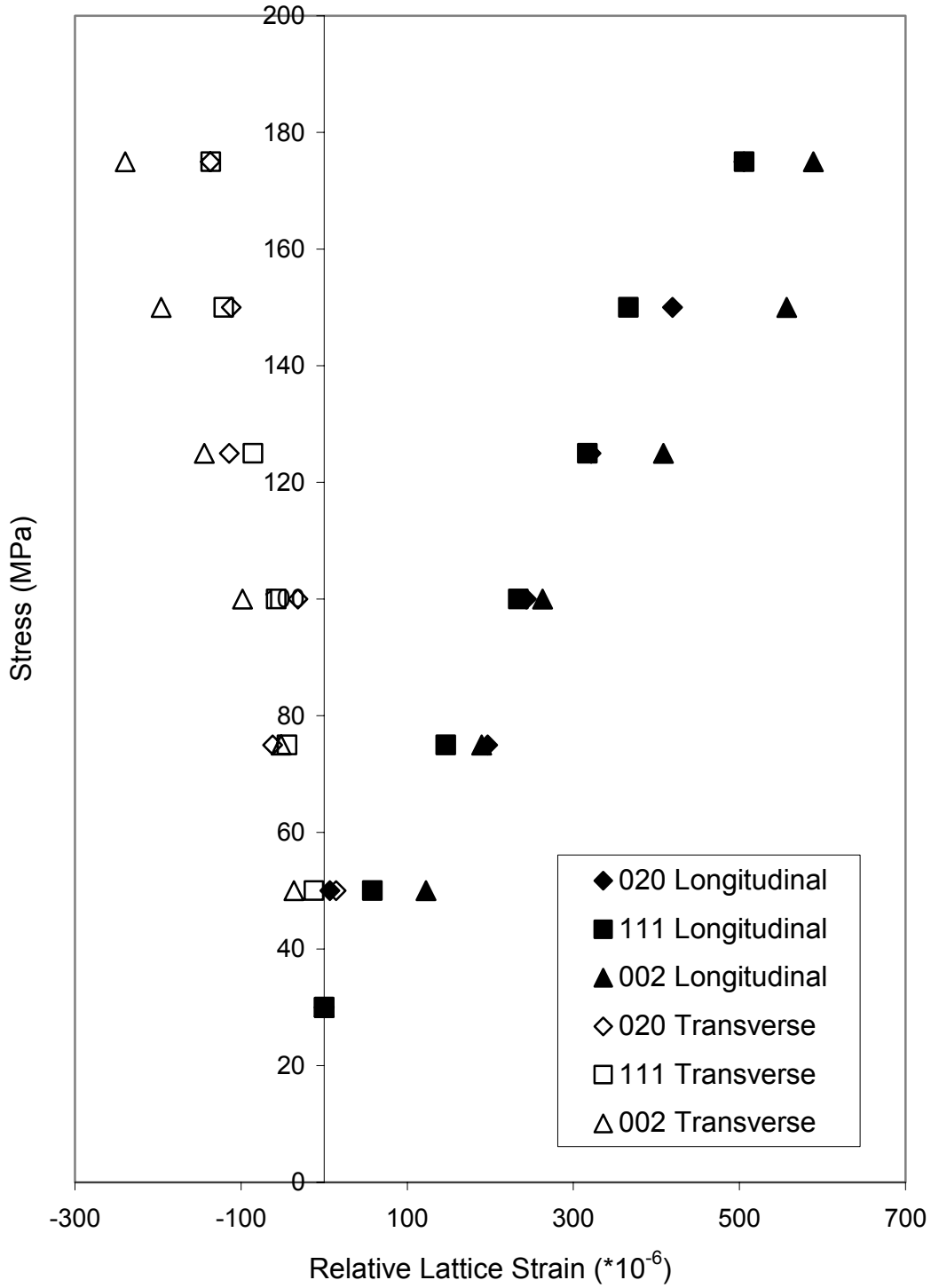

Figure 15. Stress versus strain for three AS800 reflections. Open symbols are transverse strains, while filled symbols are longitudinal strains. Error bars are omitted for clarity. (See Figures A1-A9 for individual plots with error bars.)

model to determine plastic deformation properties of materials. A homogeneous matrix is assumed in which the grains of the material are embedded. Based on the behavior that a grain of a particular *hkl* orientation would experience, derived from the single crystal stiffness tensor for that material, the model determines what strains might be observed in diffraction based on an input stress. This method requires the single crystal stiffness tensor to predict *hkl*-behavior, but that tensor was unknown. Instead, the measured *hkl* strains were input and the stiffness tensor refined. The resolved stiffness tensor for AS800 at 1648 K is given in Equation (24). This is the first time such a stiffness tensor has been determined for Si_3N_4 at this temperature (or for any material at this temperature using TOF ND). Thus, there are no like comparisons for determining its veracity. This stiffness tensor information is important for those who produce predictive behavior models for material systems.

$$C_{ij} = \begin{pmatrix} 456 \pm 31 & 158 \pm 40 & 238 \pm 21 & 0 & 0 & 0 \\ 158 \pm 40 & 456 \pm 31 & 238 \pm 21 & 0 & 0 & 0 \\ 238 \pm 21 & 238 \pm 21 & 311 \pm 40 & 0 & 0 & 0 \\ 0 & 0 & 0 & 144 \pm 11 & 0 & 0 \\ 0 & 0 & 0 & 0 & 144 \pm 11 & 0 \\ 0 & 0 & 0 & 0 & 0 & 149 \pm 40 \end{pmatrix} \text{GPa} \qquad (24)$$

However, there are some literature stiffness values, though for different test conditions and different grades of Si_3N_4. Table VII compares these results to these literature data. As might be expected, the present tensor differs from the literature. Besides the temperature difference of the test methods, Vogelgesang *et al*.,[62] tested single crystal Si_3N_4 samples. As the present work made use of polycrystalline material produced under different conditions, discrepancy is unsurprising. Note, though, that the C_{33} component is

noticeably less (*i.e.*, softer) than the literature, while other values are more similar. This coincides with the previously mentioned softening along that crystallographic direction for AS800.

Table VII. Stiffness tensor comparison of AS800 at 1648 K ("Current work") to room temperature results [62] on non-ISR Si_3N_4 single crystals. All values are GPa.

	C_{11}	C_{33}	C_{44}	C_{66}	C_{12}	C_{13}
Current work	456	311	144	149	158	238
[62]	433	574	108	119	195	127

From the stiffness tensor components of Equation (24), the macroscopic Young's modulus and Poisson's ratio were determined according to Equations (15) and (16). These values were $E_{AS800,\ 1648\ K} = 313$ GPa and $\nu_{AS800,\ 1648\ K} = 0.31$, respectively. Again, these 1648 K values are greater than those quoted by the manufacturer for this material at 1473 K, 293 GPa and 0.28. However, the results from the tensor components are closer to the cited values than those from the full-pattern GSAS *d* results shown in Figure 12. Again, this is attributed to the use of single peak data being more accurate than the use of full-pattern fit data. Nevertheless, the discrepancy still exists, and is likely due to the issue mentioned above, namely, the effect of vacuum on the grain boundary phase.

Data from scans taken after applied stress was removed (back to the holding stress of 30 MPa) were used to check for any residual strain in the sample. Table VIII shows the longitudinal strains measured at 30 MPa and 1648 K after unloading, relative to the initial

30 MPa data at 1648 K. Table VIII also shows the averaged strains for the lattice parameters *a* and *c*, polycrystalline average *d*, and the nine single peaks. Also shown are the residual strains after cooling down to room temperature, strains relative to the initial pre-heating room temperature scans. Table IX gives the transverse strains for the same conditions.

Table VIII. Residual longitudinal strains for AS800 after reducing stress at 1648 K and after cooling to 300 K. Values are given in microstrain (με). Presented values are the average of strains from multiple patterns after unloading and after cooling.

***hkl* or lattice parameter**	**Residual strain at 1648 K**	**Residual strain at 300 K**
a	-80 ± 20	-30 ± 20
c	30 ± 30	110 ± 30
d	-70 ± 30	-10 ± 20
(02·0)	20 ± 130	-10 ± 80
(01·1)	30 ± 120	70 ± 70
(12·0)	-60 ± 160	70 ± 100
(11·1)	-50 ± 50	40 ± 30
(13·0)	-70 ± 180	0 ± 160
(03·1)	-160 ± 210	-100 ± 120
(22·1)	-10 ± 50	20 ± 30
(23·0)	-10 ± 110	70 ± 60
(00·2)	-40 ± 60	160 ± 40

Table IX. Residual transverse strains for AS800 after reducing stress at 1648 K and after cooling to 300 K. Values are given in microstrain (με). Presented values are the average of strains from multiple patterns after unloading and after cooling.

***hkl* or lattice parameter**	**Residual strain at 1648 K**	**Residual strain at 300 K**
a	-100 ± 10	-32 ± 10
c	-140 ± 20	-36 ± 20
d	-20 ± 20	-32 ± 10
(02·0)	-30 ± 70	10 ± 40
(01·1)	-20 ± 60	-50 ± 40
(12·0)	-60 ± 80	-90 ± 50
(11·1)	-40 ± 30	0 ± 20
(13·0)	-140 ± 100	-50 ± 100
(03·1)	120 ± 100	50 ± 70
(22·1)	-10 ± 30	0 ± 20
(23·0)	-30 ± 60	-70 ± 40
(00·2)	-90 ± 40	-100 ± 40

As seen from the values in Table VIII and Table IX, slight residual strains exist in both directions for all reflections and lattice parameters, but these strains are minor and nearly all are zero within the fitting error. This lack of significant residual strains corroborated the elastic nature of the high-temperature experiment, and so the computation of the elastic stiffness tensor was not invalidated.

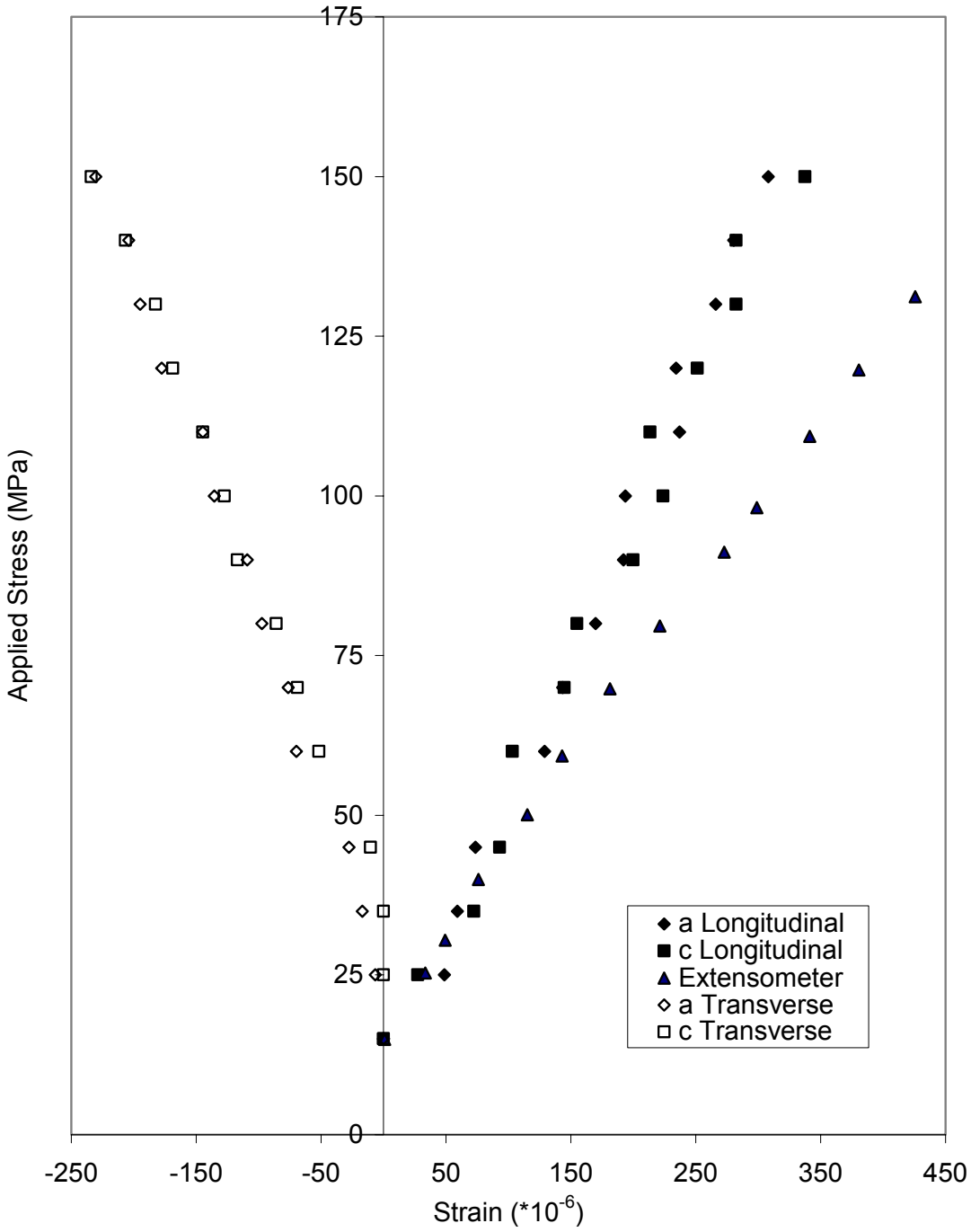

Figure 16. Stress-strain plot for longitudinal diffraction data and extensometer for first room temperature loading experiment of AS800. Both *a* and *c* are plotted from diffraction data for both banks, plus the extensometer data. Error bars are omitted for clarity (see text for typical values).

3.1.3 Room-Temperature Stress Application

As mentioned in Table III, there were two separate attempts to test AS800 at room temperature. The stress-strain curve from the first experiment (October 2002) is shown in Figure 16. Only the *a* and *c* lattice parameters and extensometer data are shown. Error bars are not shown (in order to maintain clarity of the presented data), but maximum error bars for *a* were 20 με and 15 με for longitudinal and transverse data, respectively. Correspondingly, the *c* error bars were 30 με and 20 με. The Poisson's ratio for these data was 0.81, which is an unrealistic value. The Young's modulus from the extensometer data seems realistic at 270 GPa, but this result is noticeably different from the diffraction strain value of 446 GPa. It was concluded that some manner of systematic error was present in this data, perhaps a displacement error, causing the measured strains to be unrealistic. Single peak fits were similarly erroneous. This systematic error prevented the calculation of the room temperature stiffness tensor.

The second room-temperature experiment of AS800 was performed in September 2003. The stress-strain data are shown in Figure 17, though only longitudinal data are shown as the transverse data indicated tensile strains. As this results in a negative Poisson's ratio, and is unknown for Si_3N_4, the transverse data are believed to be erroneous. In this case, there is believed to have been another systematic error; however, the instrument parameter file was out of date for the transverse detector bank (bank 1) and could have played a role in the inherent unrealistic results for the elastic constants. Single peak fits indicated tensile strains in the transverse direction as did the full-pattern fit lattice

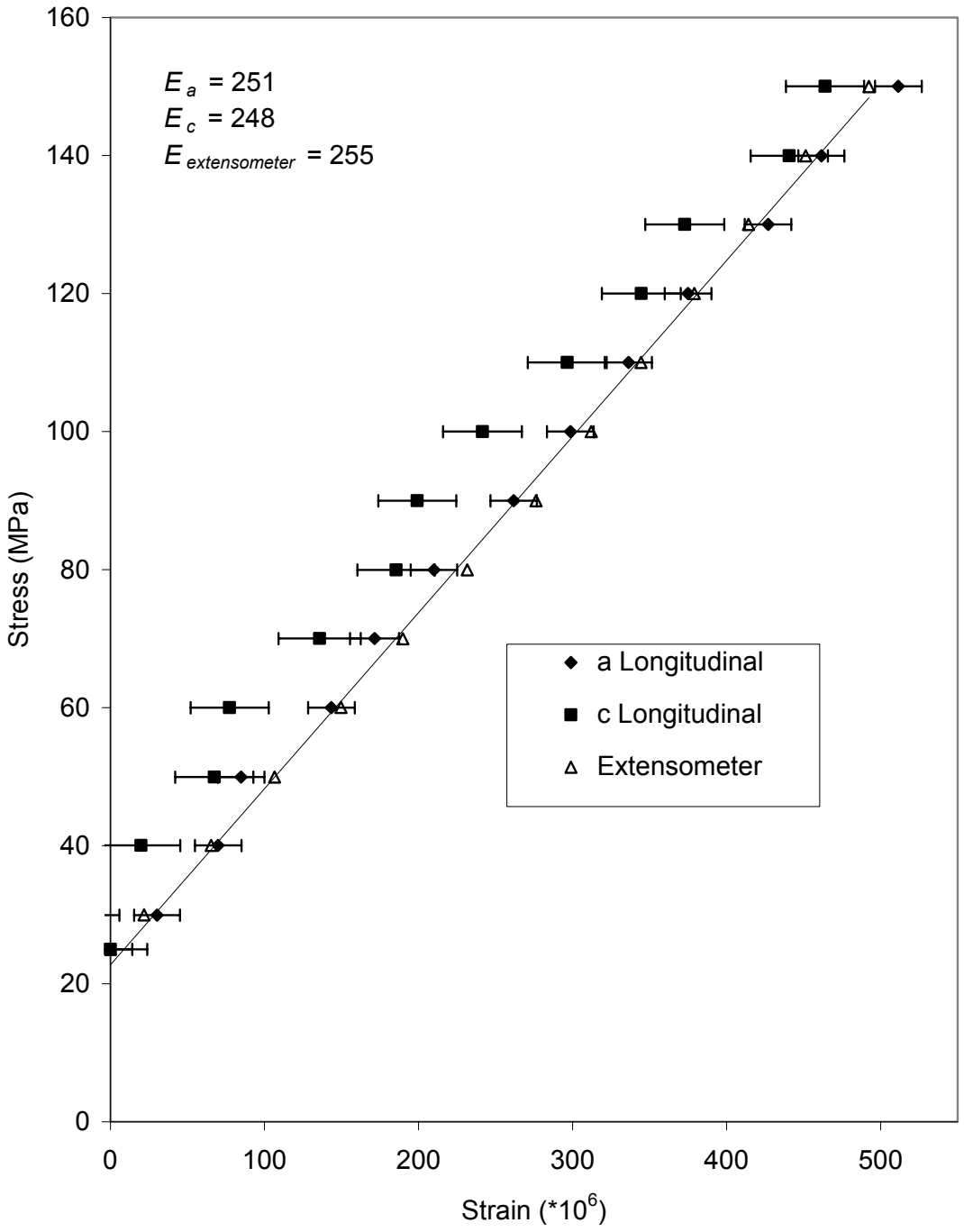

Figure 17. Stress-strain plot for longitudinal diffraction data and extensometer for second room temperature loading experiment of AS800. Transverse data are not plotted, as they indicated tensile strain. There is acceptable agreement, however, of the longitudinal data and the extensometer.

parameters. Thus, the room-temperature stiffness tensor was incalculable for AS800. Note, however, that in Figure 17 the longitudinal diffraction strains agree well with the extensometer. The Young's modulus from the extensometer was E = 255 GPa, while the polycrystalline average (not shown) was 249 GPa. Both the extensometer and diffraction strain-derived Young's moduli are significantly less than their corresponding values from both literature and at high-temperature. The origin of this discrepancy is unknown, but the agreement between the longitudinal diffraction data and the extensometer point to the present results' accuracy.

3.1.4 Ultrasonic Elastic Constant Measurement

Table X shows the results from the ultrasonic measurement method. These results were obtained by ultrasonic testing of an as-received AS800 sample, that is, a sample that had not been exposed to any mechanical or thermal testing. The sample was tested in both the grip and gage regions, with the results being the same. The Young's modulus, E, shear modulus, G, and Poisson's ratio, ν, are given. The corresponding values from the manufacturer are shown for comparison. The similar results suggest that this method perhaps was that used by the manufacturer for determining these quantities. The fact that the samples subjected to applied stress for diffraction data collection came from the same sample material as that tested with the ultrasonic method, yet all give very different results, indicates that there are additional experimental variable affecting the diffraction data collection. The high degree of correlation using the ultrasonic method seems to indicate that the manufacturer's quoted values are acceptable, but that some aspect of the SMARTS setup prevents obtaining comparable results. These results are vastly different from the data collected on SMARTS for AS800 at room temperature. This discrepancy

may be related to the pull-rods and grips used for the SMARTS room temperature testing. The rods and pins are made from stainless steel, while the grips are made from a Mo-containing steel. These are replaced with the better-characterized high-temperature W-10Th grips and rods. If the cold rods and grips were not machined precisely, then the applied load may not have been uniaxial, resulting in the lower value for *E* from SMARTS, which was consistent between the diffraction and extensometer. Alternatively, the applied load may have been recorded incorrectly. The latter possibility is discounted, as the high-temperature data, with the W-10Th equipment, are more in line with literature values than are the room temperature data.

Table X. Ultrasonic measurement results for room-temperature elastic constants of AS800. Data were collected at two regions of a non-tested AS800 sample (*i.e.*, not exposed to heat or applied stress), the grip region and the gage region with the same results obtained.

	***E* (GPa)**	***G* (GPa)**	***ν***
Present results	317 ± 4	124 ± 2	0.28 ± 0.01
Manufacturer	310	122	0.28

3.2 GS-44

Multiple GS-44 samples were tested at various conditions. Table XI summarizes these experiments. The less refractory grain boundary material precludes testing this grade of Si_3N_4 at the same temperature as AS800. However, while the manufacturer indicates a maximum use temperature of 1273 K, samples were tested at 1473 K. This test

temperature was chosen, first, because there is creep literature for this grade at 1473 K, and second, in effort to alleviate the creep inhibition due to the SMARTS vacuum furnace.

Table XI. GS-44 Experiments

CTE	**High-Temperature Loading**	**Creep stress (MPa)**	**Room Temperature Loading**	**Date**
Yes	Yes	120-150-175	No	October 2002
No	No	-	Yes	October 2002
No	No	-	Yes	September 2003
No	Yes	100	No	November 2003
No	Yes	125	No	November 2003
No	Yes	150	No	September 2003
No	Yes	175	No	September 2003
Yes	Yes	-	No	November 2003

3.2.1 CTE Data

The CTE of GS-44 was determined in the same manner as for AS800. Note that there were two measurements of the GS-44 CTE. The earlier measurement was performed with a sample from a different block of material as the second. The second block of material was the source for all the specimens tested in November 2003. The second measurement was intended to determine whether there were any significant differences between the two materials. Figure 18 shows the diffraction data for thermal expansion strains from the 2002 measurement, while Figure 19 shows the same for the 2003 measurement. In both cases, the thermal expansion is linear and agrees well with the extensometer data. The 2003 measurement made use of data from more temperatures,

though the results are similar. Note that both samples were under a 25 MPa holding stress, as discussed earlier, to keep the sample in the center of diffraction. For both samples, the same nine *hkl*s as with AS800 were used to determine the tensor using ALPHA, with results shown in and Equations (25) and (26).

$$\alpha_{GS44,2002} = \begin{pmatrix} 3.07 \pm 0.09 & 0 & 0 \\ 0 & 3.07 \pm 0.09 & 0 \\ 0 & 0 & 3.62 \pm 0.13 \end{pmatrix} \times 10^{-6} K^{-1} \quad (25)$$

$$\alpha_{GS44,2003} = \begin{pmatrix} 3.38 \pm 0.04 & 0 & 0 \\ 0 & 3.38 \pm 0.04 & 0 \\ 0 & 0 & 3.70 \pm 0.05 \end{pmatrix} \times 10^{-6} K^{-1} \quad (26)$$

Table XII CTE values for lattice parameters (*a, c* and *d*), ALPHA (α_{avg}), and the extensometer, as shown in Figure 18 and Figure 19, indicated as "2002" and "2003," respectively.

Parameter	**2002 CTE (*10^{-6} K^{-1})**	**2003 CTE (*10^{-6} K^{-1})**
a	3.19	3.37
c	3.65	3.84
d	3.27	3.53
α_{avg}	3.25	3.49
Extensometer	3.18	3.28

Table XII summarizes the CTE parameters plotted in Figure 18 and Figure 19, while Table XIII gives the CTE for each of the nine single peaks. These CTE values for diffraction data-derived parameters (namely, *a*, *c*, and *d*) in these tables are the slopes to linear fits of the thermal expansion diffraction data. As previously presented, α_{avg} is determined from the tensor components of Equations (25) and (26) using Equation (22).

Comparison of the two measurements indicates that while the CTE values are consistently higher in the 2003 measurement (for all parameters, ranging from 10-26 με K^{-1} greater than the 2002 measurement), the difference is not extreme. The 2003 measurement, however, seems closer to the literature value of 3.4 x 10^{-6} K^{-1}. Also, the fitting errors from ALPHA were less with the 2003 data, indicating that the 2002 data may not have been optimal. Table XIII gives the single peak CTE values from linear fits to the 2003 data.

Table XIII CTE of individual reflections from both longitudinal and transverse diffraction data (September 2003), from linear fits to single peak data. All values are *10^{-6} K^{-1}.

hkl	**CTE (longitudinal)**	**CTE (transverse)**
(02·0)	3.6	3.1
(01·1)	3.9	3.6
(12·0)	3.4	3.2
(11·1)	3.7	4.1
(13·0)	3.4	3.2
(03·1)	3.4	3.4
(22·1)	3.5	3.4
(23·0)	3.4	3.3
(00·2)	3.9	3.8

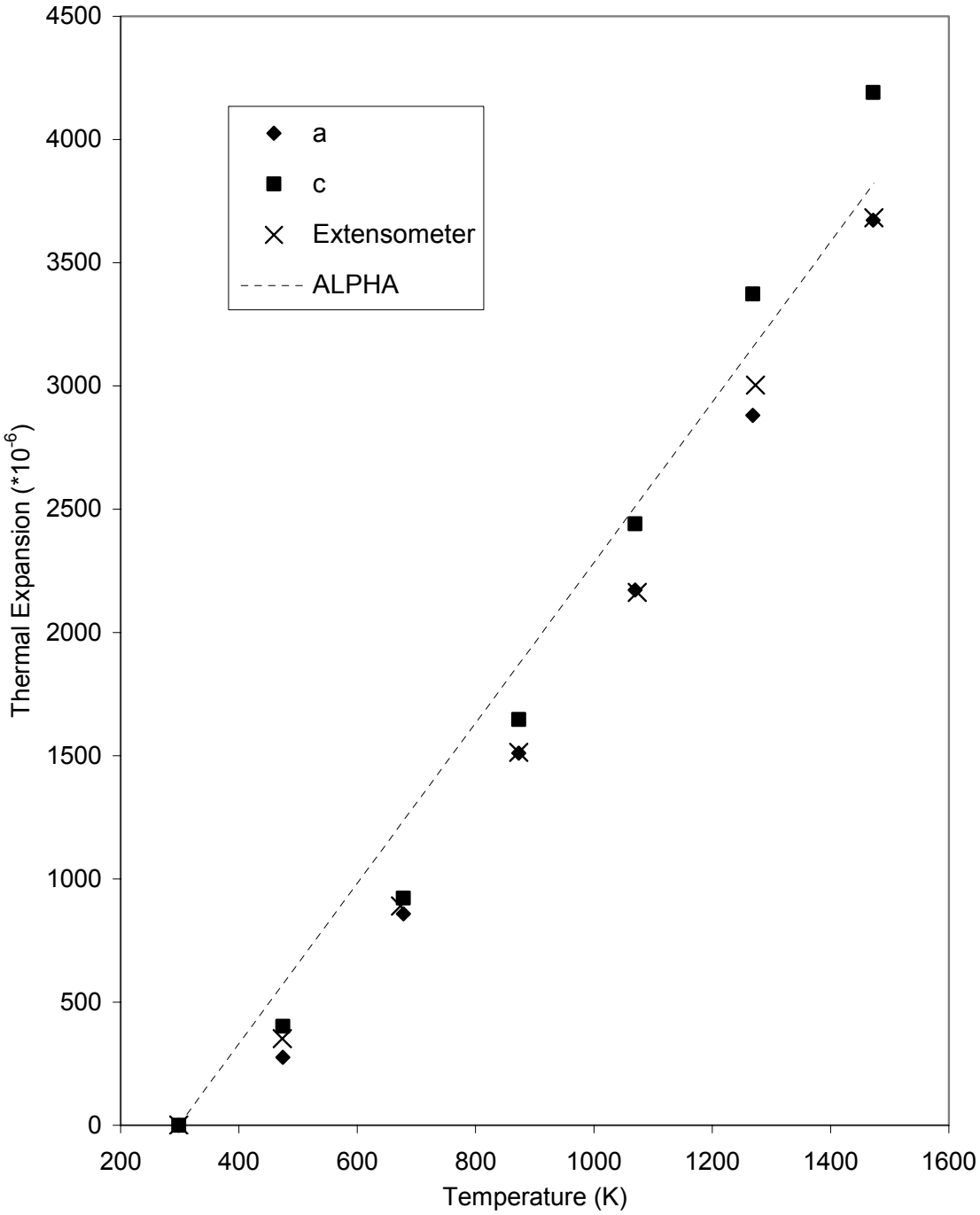

Figure 18. Thermal expansion of GS-44 based on 2002 SMARTS measurements. Error bars are included for *a* and *c*, based on GSAS fitting errors, but they are too small to appear.

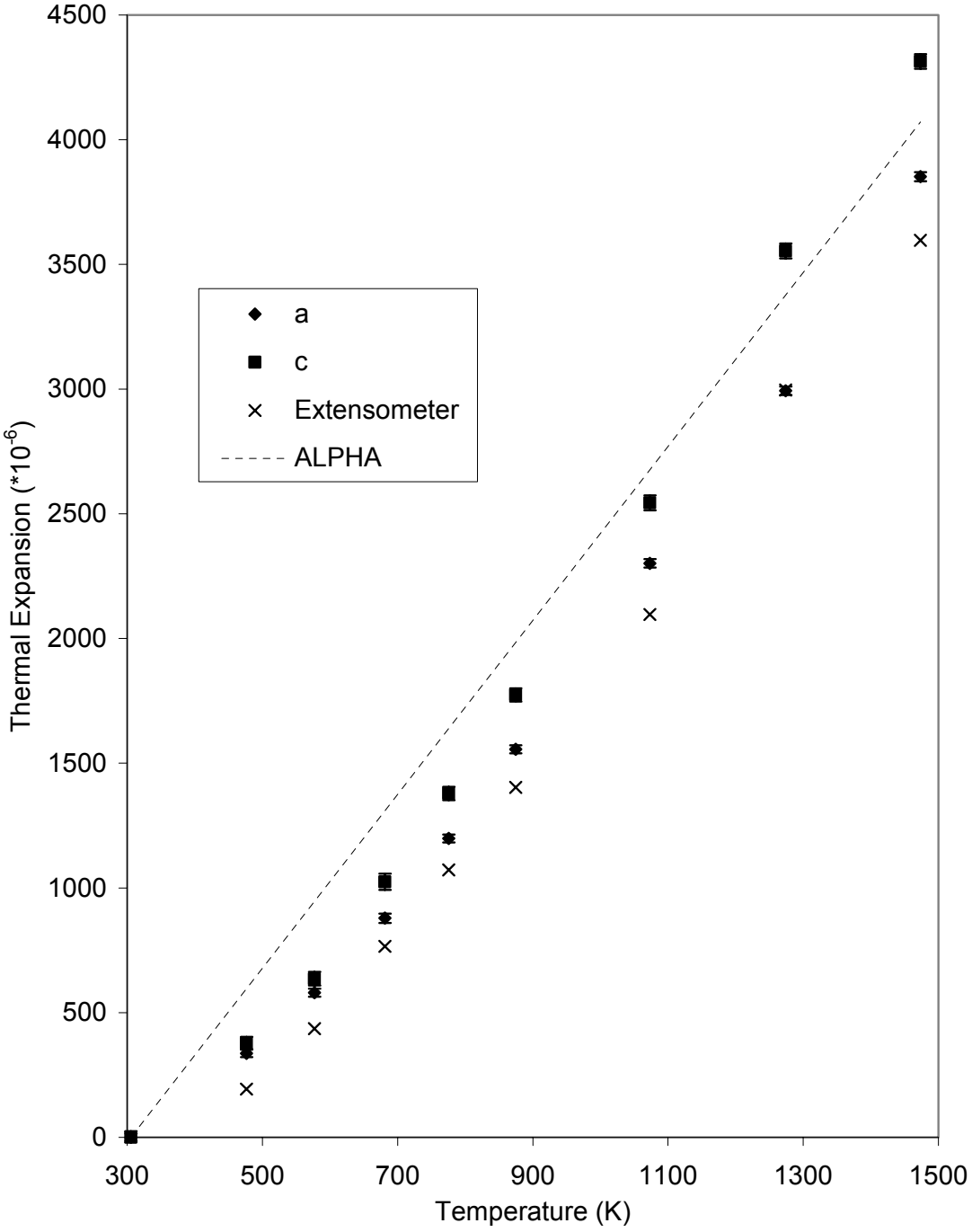

Figure 19. Thermal expansion of GS-44 based on 2003 SMARTS measurements. Error bars are included for *a* and *c*, based on GSAS fitting errors.

Regarding *hkl*-dependent CTE properties, the 2003 data are considered in the following discussion, due to the greater confidence inspired by the improved ALPHA fitting. As shown in Figure 19 and Table XIII, the *c*-axis of GS-44 experiences a greater thermal expansion than the *a*-axis, as was the case with AS800. Note, as shown in Table XIII, that the greatest CTE is not possessed by the (00·2) reflection, but by the (11·1). The (00·2) and (01·1) reflections have the next highest CTEs; as they have the highest *c*-character of the remaining eight reflections this is not unexpected. As for AS800, reflections with zero *c*-character, *i.e.*, (02·0), (12·0), (13·0) and (23·0), have the lowest CTE, while the other mixed *hkl*s, *e.g.*, (03·1), have intermediate CTEs. The aspherism index, computed from Equation (13) using the tensor components of Equation (26), is $A = 0.02$. This indicates that GS-44 has a less anisotropic CTE than AS800, which can be seen by the lesser difference between the *a* and *c* CTE values from Table XII for GS-44 compared to those for AS800 in Table IV. This would indicate that there would be a more uniform microstructural shrinkage from high-temperature when cooling from the processing temperature. This may be due to the different chemistry of the GS-44 grain boundary phase, and its lower viscosity at lower temperatures than the grain boundary phase of AS800, indicated by creep at lower temperature than AS800.

3.2.2 High-Temperature Stress Application

3.2.2.1 High-Temperature Young's Modulus

The first GS-44 sample tested at high-temperature on SMARTS was subjected to multiple loads. At 1473 K, after heating under a stress of 25 MPa (and collecting CTE data) the sample was loaded up to 100 MPa stress in 10-15 MPa increments. The stress-strain

curve for this loading is shown in Figure 20, with longitudinal strains only; note that strains shown are relative to the initial 25 MPa 1473 K pattern, *i.e.*, CTE strains are subtracted. Note that in this case, the *c*-axis very closely follows the behavior of the extensometer, and is much less stiff than the *a*-axis, as was seen with AS800. Though the polycrystalline average is not plotted, the Young's modulus was calculated as E_d = 302 GPa. The extensometer indicated a modulus of just 225 GPa, which is the slope of the line in Figure 20. The transverse data for this experiment was very non-linear and erroneous, with the c-axis showing tensile strains primarily. The data gave a Poisson's ratio for ν_d of nearly 0.5. Subsequent experiments attempted to obtain better quality stress-strain data for GS-44.

The best stress-strain curve, in terms of quality of linear fits from both banks and the resulting elastic property values, was from the 125 MPa creep sample, which was loaded at 1473 K in 25 MPa increments. The data for this experiment are shown in Figure 21, with CTE strains subtracted. As with Figure 20, the *c*-axis strains similarly to the extensometer, which had E = 235 GPa. The calculated polycrystalline average (not plotted) was E_d = 293 GPa, in close agreement with the manufacturer but not with the extensometer. The Poisson's ratio was ν_d = 0.22, again a very reasonable value. For the *a* and *c* axes, respectively, had E = 320 and 239 GPa, ν = 0.34 and 0.18. The plotted strain errors were approximately 21 με for *a* and 35 με for *c*. Table XIV shows elastic properties for single peaks. Note the poor quality of the linear fits (r^2 far from 1). This non-linear behavior was dominant for all the GS-44 samples, preventing determination of the 1473 K stiffness tensor. Aside from CTE data, only full-pattern fit data were used.

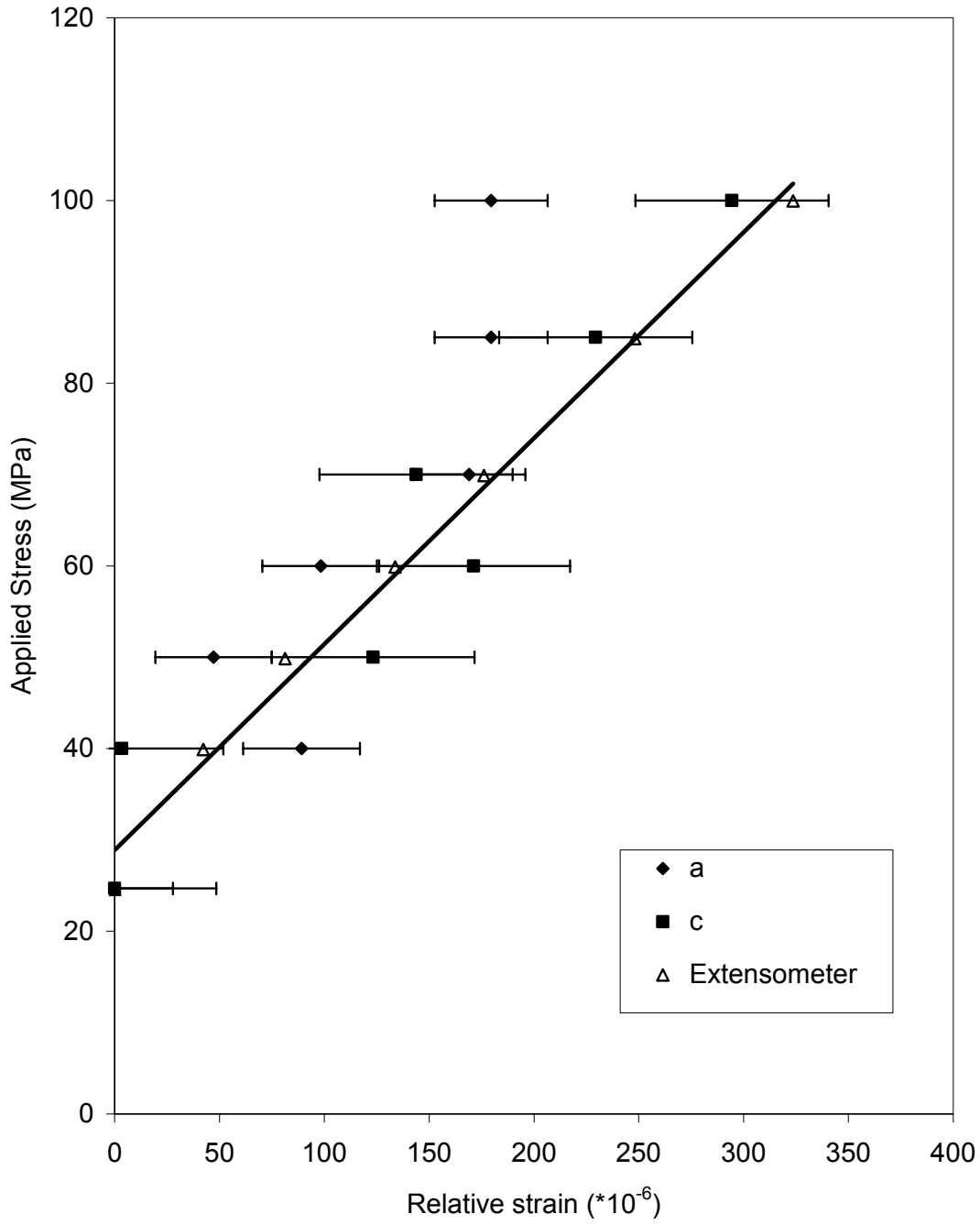

Figure 20. Stress-strain data up to 100 MPa for GS-44 at 1473 K. A linear fit to the extensometer data is shown. Error bars based on GSAS fitting residuals are provided.

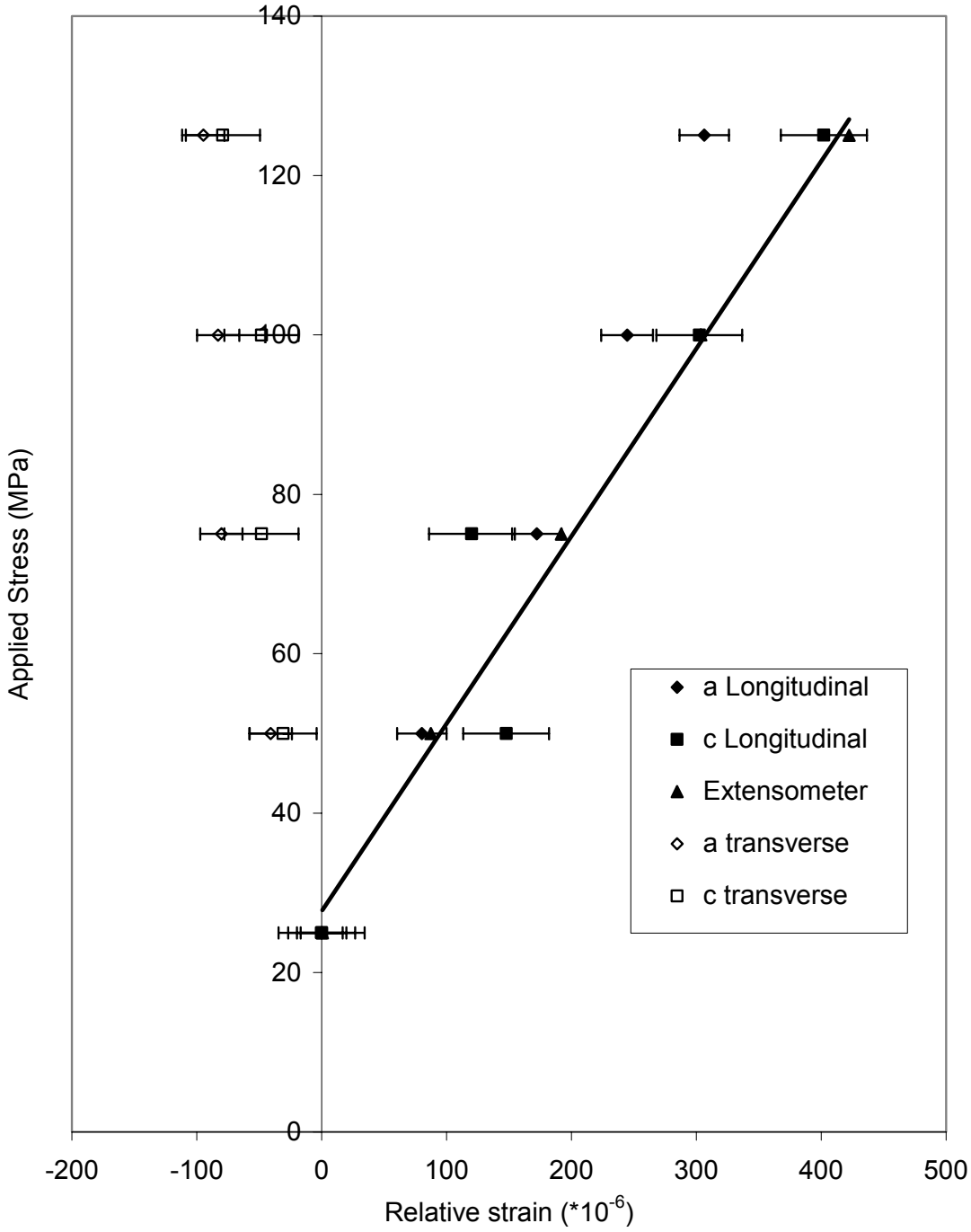

Figure 21. Stress-strain data up to 125 MPa for GS-44 at 1473 K. A linear fit to the extensometer data is shown. Error bars based on GSAS fitting residuals are provided.

Table XIV. Elastic constants for specific *hkl* reflections for GS-44 from diffraction data, *E* given in units of GPa. *E* is presented for linear fits to diffraction data (first two columns), and is compared to predicted values using the AS800 tensor of Equation (24) and the tensor from [62]. Values in parentheses are fitting r^2 values (columns 1 and 2) or relative difference of columns 3 and 4 compared to column 1.

hkl	***E*** **(fit r^2)**	***ν*** **(fit r^2)**	***E* [62]** **(% diff)**	***E* eqn (24)** **(% diff)**
(02·0)	316 (0.746)	0.491 (0.252)	336 (5.9)	312 (1.4)
(01·1)	203 (0.768)	0.320 (0.819)	368 (45)	261 (22)
(12·0)	103 (0.140)	0.276 (0.111)	336 (69)	312 (67)
(11·1)	327 (0.865)	0.225 (0.585)	330 (0.8)	305 (7.1)
(13·0)	385 (0.679)	4.332 (0.014)	336 (15)	312 (24)
(03·1)	263 (0.734)	0.688 (0.186)	313 (16)	339 (22)
(22·1)	289 (0.745)	0.347 (0.444)	313 (7.6)	341 (15)
(23·0)	114 (0.104)	0.727 (0.025)	336 (66)	312 (63)
(00·2)	308 (0.911)	0.305 (0.368)	426 (28)	225 (37)

Also in Table XIV are the predicted values for E_{hkl} as with AS800. Since the transverse data was of low quality, the predicted Poisson's ratios are not compared here. Since the

tensor for GS-44 was not obtainable, comparing it to AS800 is unsuitable. The inability to obtain the GS-44 tensor was likely due to the GS-44 experiencing inelastic strain due to increased stress at temperature compared to AS800. Note that AS800 was tested below it maximum use temperature, while GS-44 was tested above its maximum use temperature.

3.2.2.2 Creep Experiments

There were five creep experiments performed on GS-44 at 1473 K. The first was a stress step-up experiment, while the other four were longer-term, single-stress experiments. All experiments ended with an unload to allow creep recovery, after which the sample was cooled back to room temperature. Creep recovery took place at the minimum 25 MPa used for sample position maintenance. Note that the single-stress creep tests incorporated an unload to 25 MPa during the creep test, to determine any effect on the elastic properties, followed by a reloading to the creep stress. These unloads were performed after steady-state creep had initiated. Creep was then continued for a significant time before the sudden unload for creep recovery. These in-creep unloads were performed in steps rather than the sudden unloading used for creep recovery.

The stress step-up creep test first subjected the sample to 100 MPa, then 120 MPa, and finally 150 MPa. Figure 22 and Figure 23 show the stress-strain data for both directions for the *a* and *c* lattice parameters, respectively, with the extensometer data also shown. Strains are relative to the initial 1473 K, 25 MPa data. When comparing these two figures, note from Figure 23 that the *c* strain at the start of the creep test is nearer the

extensometer strain than the *a* strain of Figure 22. This is the same phenomenon as when loading elastically and the *c* strain more closely approximated the extensometer than did the *a* strain. However, during the constant load portions of the test, the strain remains constant within the data fitting error, while the extensometer clearly shows a strain increase at constant stress, indicating that creep was occurring. Only when the load was increased did the strain experience a noticeable strain increase. Note that the approximate strain increase due to stepping up the stress in the longitudinal *c*-strain was closely correlated with the strain increase of the extensometer. The increase from 100 to 120 MPa added 115 με to the extensometer and 85 με to the *c*-strain, while the 120-150 MPa increase added 150 με and 140 με, respectively. The strains were compared to the predictions of Hooke's Law, shown in Equation (27), with applied stress σ, strain ε, and Young's modulus E. This relation holds for materials subjected to tensile stress, generally at low levels, for which the resulting strain is proportional to the applied stress with E the constant of proportionality, with the material behavior referred to as *elastic* in this region [7]. Note that while Equation (27) is a relation for the initial elastic part of the stress-strain curve, for some materials such as cast iron, the initial stress-strain behavior is non-linear and other methods are used to determine the Young's modulus.

$$\sigma = E\varepsilon \qquad (27)$$

The increase from 100 to 120 MPa was a 20 MPa increase, while that from 120 to 150 MPa was a 30 MPa increase. Since Hooke's Law is a linear relation, the change in stress was used to determine the predicted change in strain. The value used for E (220 GPa) was the manufacturer's value for 1273 K (see Table I), the closest literature value to the test temperature of 1473 K. A change in stress of 20 MPa is predicted to result in a strain

change of 90 με, very close to the *c*-strain of 85 με. A change of 30 MPa should result in a strain change of 140 με, again, closely matching the *c*-strain. Thus it was concluded that Si_3N_4 grains were elastic within the sample, as Hooke's Law is a relation for elastic stress-strain in materials.

In Figure 22, when the unload and creep recovery began, the transverse and longitudinal *a*-strains switched sense, meaning that the longitudinal strain went from tensile to compressive, and vice versa for the transverse strain. This did not occur for the *c* axis in Figure 23, though the transverse strain alone did change sense. (The error bars in the creep recovery portion of Figure 23 have been omitted so that the two directions can be seen.) The unload decreased the extensometer strain by 560 με, with the longitudinal *c*-strain dropping by 450 με. A greater discrepancy than for the stress increases, but the two are still comparable. Note that the transverse strain jumps by 200 με due to the unload. The longitudinal *a*-strains, by comparison, increased by 70 and 100 με for the two stress increases, while the unload induced a drop of 330 με for the longitudinal and a jump of 175 με for the transverse *a*-strains. The *a* axis of GS-44 attained residual strain of the opposite sense (compressive to tensile and vice versa) from that induced by stress application in both detector banks. The *c* axis, however, exhibited tensile residual strain from both detector banks. This could be an indication of grain sliding which prevented a return to the initial state. Given that the *c* axis has been demonstrated to be more compliant, the different nature of its residual strain is acceptable. Single peak data, however, were deemed unusable, for the same reason as in the previous section (poor results, lack of trends).

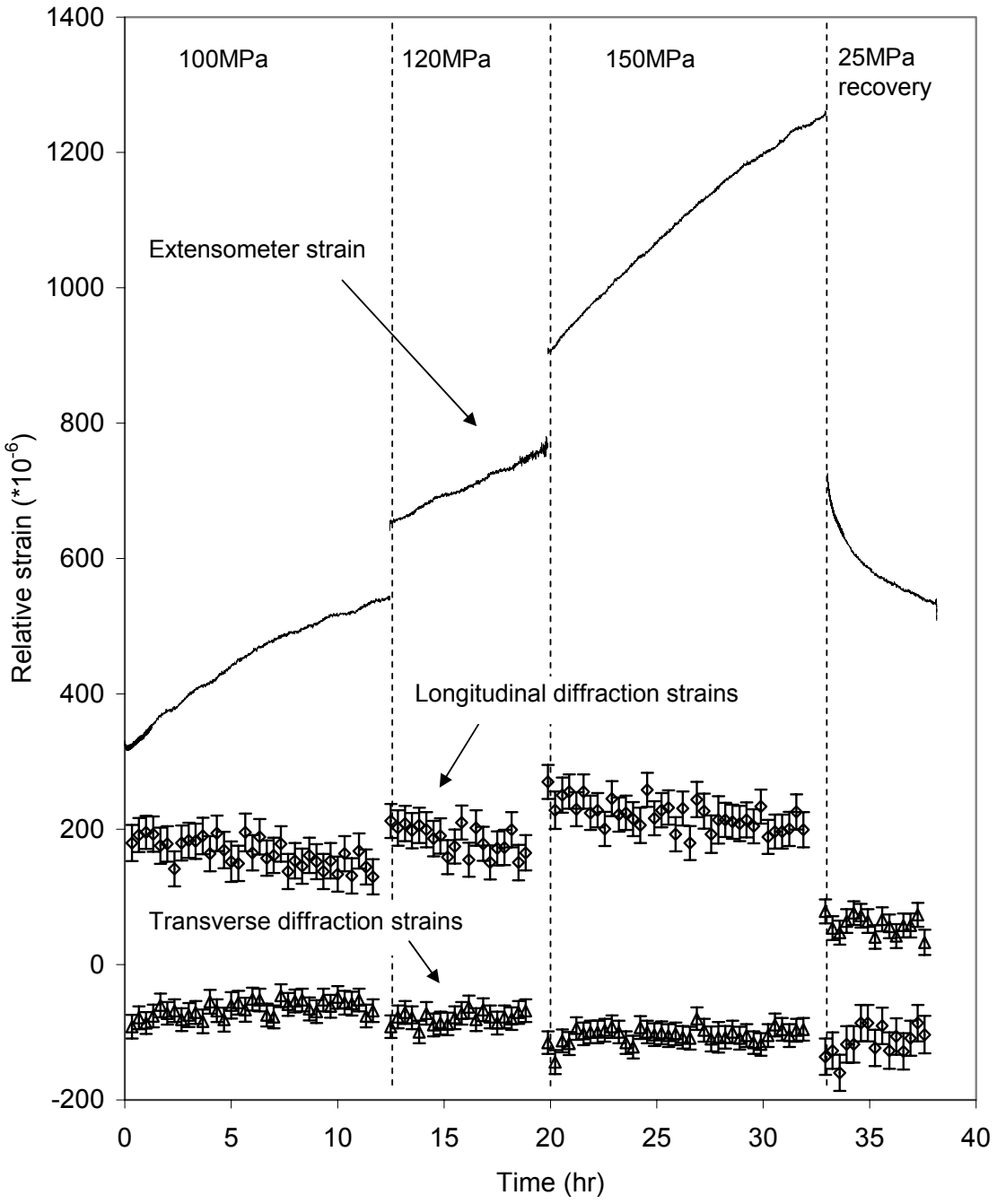

Figure 22. Longitudinal and transverse diffraction strains for *a* lattice parameter of GS-44, and extensometer strain, under various stresses at 1473 K. Diamonds are longitudinal data, triangles are transverse data. Strains are relative to 25 MPa, 1473 K data.

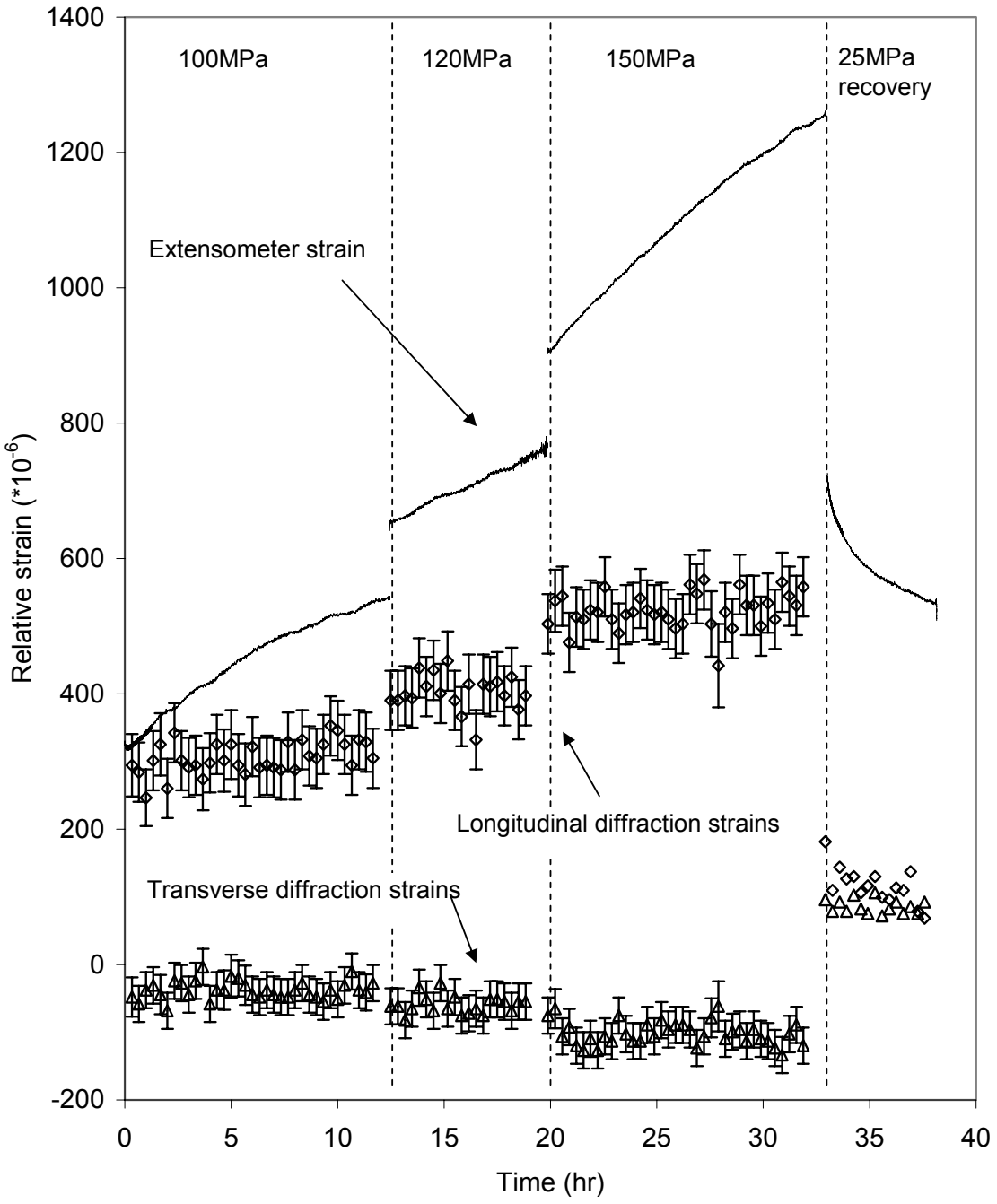

Figure 23. Longitudinal and transverse diffraction strains for *c* lattice parameter of GS-44, and extensometer strain, under various stresses at 1473 K. Diamonds are longitudinal data, triangles are transverse data. Strains are relative to 25 MPa 1473 K data.

Using the extensometer strain for each stress, the stress exponent for GS-44 in vacuum was determined. A linear fit was applied to the strain data. For the 100 MPa data, this was done in the region after approximately 8 hours of creep, when the slope changed. This was the onset of secondary or steady-state creep. The 120 and 150 MPa strains were fit as a line over their entirety. While the data are not perfectly linear, the quality of fits was acceptable. The slope of the linear fits is the steady-state creep rate. When this creep rate is plotted as a function of applied stress on a log-log plot, the creep exponent is determined from the slope of a linear fit. This gave a creep exponent for GS-44 of $n = 2$, comparable with the results of others. Wei *et al.* [25] reported a creep exponent of $n = 2.24$, while values for ISR Si_3N_4 range from 2-4, with even greater values sometimes reported [3, 27]. Since n is not unity, it is clear that diffusional creep is not the mechanism observed here.

After the multi-stress step-up test described above, it was clear that creep of GS-44 could be realized in the SMARTS vacuum furnace. Further creep tests were performed, each applying a different stress to the sample for a longer period than the 12 hours or less of the step-up experiment. Four tests were conducted, at 100, 125, 150, and 175 MPa. Figures (24) through (27) show the *a* and *c* longitudinal strains for these four stresses. Note that the magnitude of creep is much less than that obtained by Wei *et al.* [25], for like stresses and temperature. At $t = 10$ hr, they measured strains of 2500 and 4500 με for 100 and 120 MPa applied stresses, respectively, at 1473 K. This is compared to 550 με for the present 100 MPa results at $t = 10$ hr, less than 25% of Wei *et al.*'s reported

value. The present 175 MPa creep strain at t = 10 hr was 2000 με, less than their 100 MPa result.

Unfortunately, the transverse data from these experiments were not particularly useful and are not presented here, though they are included in the appendix (Figures A10-A13). (They behaved not appreciably different from the transverse data of the stress step-up test, being essentially constant throughout the experiment. While there was a slight change noted for the 175 and 150 MPa tests, this change indicated a tensile strain for both lattice parameters, which seems to invalidate the accuracy of this data. Note that the instrument parameter file for the transverse bank was out of date when these data were collected.) As noted earlier, after steady-state creep was in progress, these four samples were unloaded then reloaded. These data are not shown in Figures (24) - (27), but are evident as gaps in the extensometer data. Gaps in diffraction data other than at this point in the creep experiment were due to loss of the neutron beam, save for the 150 MPa data of Figure (26), in which a data collection error prevented data acquisition for the first eight hours of creep and the first pattern at 150 MPa. Regarding the 150 MPa plot, note further that the initial data at 150 MPa were lost in the same error, with the first plotted data point being the 125 MPa diffraction data obtained during the load increase. Data were collected for all four samples at 25 MPa, 1473 K; these data are the reference for strain for each sample, to provide as similar as possible a comparison between samples. It can be seen quite clearly that for lower creep stress, there is less effect from unloading and reloading. The first extensometer strain measured at the creep stress for each sample was compared to the strain predicted by Hooke's Law, Equation (27).

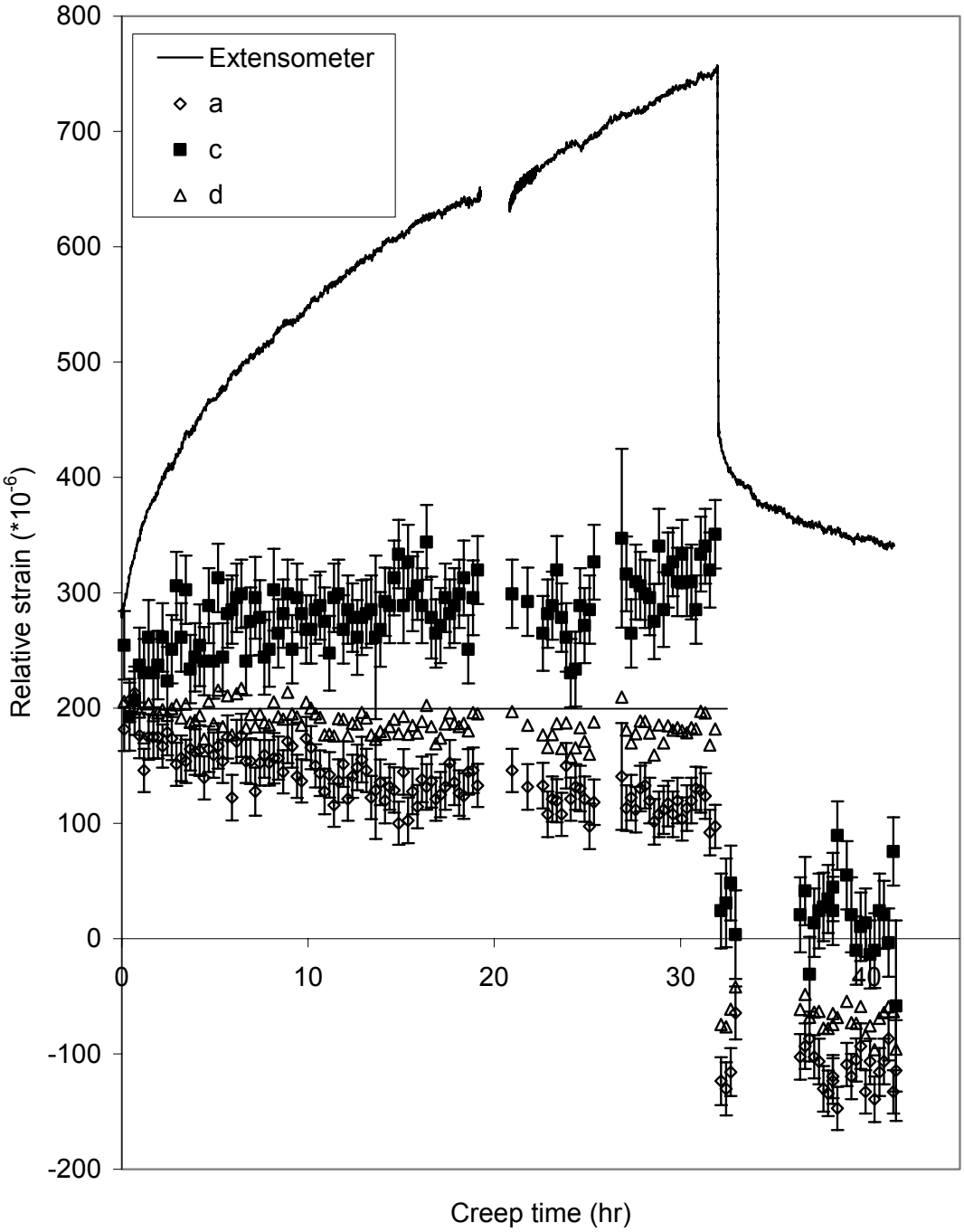

Figure 24. GS-44 creep at 1473 K with 100 MPa applied stress. Longitudinal diffraction data are shown. Strains are relative to data from 25 MPa, 1473 K. Horizontal line indicates the initial *d*-strain at 100 MPa, 1473 K.

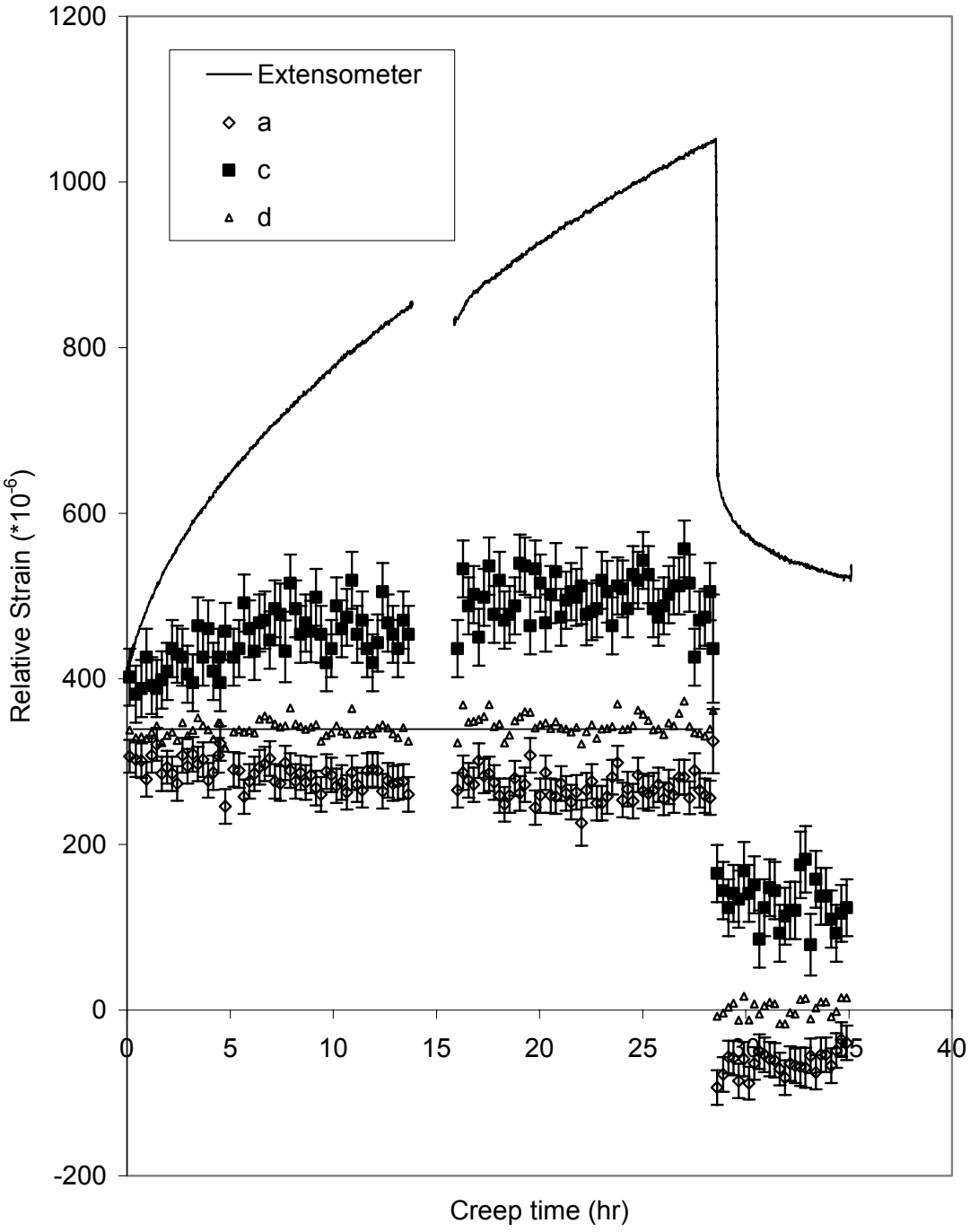

Figure 25. GS-44 creep at 1473 K with 125 MPa applied stress. Longitudinal diffraction data are shown. Strains are relative to data from 25 MPa, 1473 K. Horizontal line indicates the initial *d*-strain at 125 MPa, 1473 K.

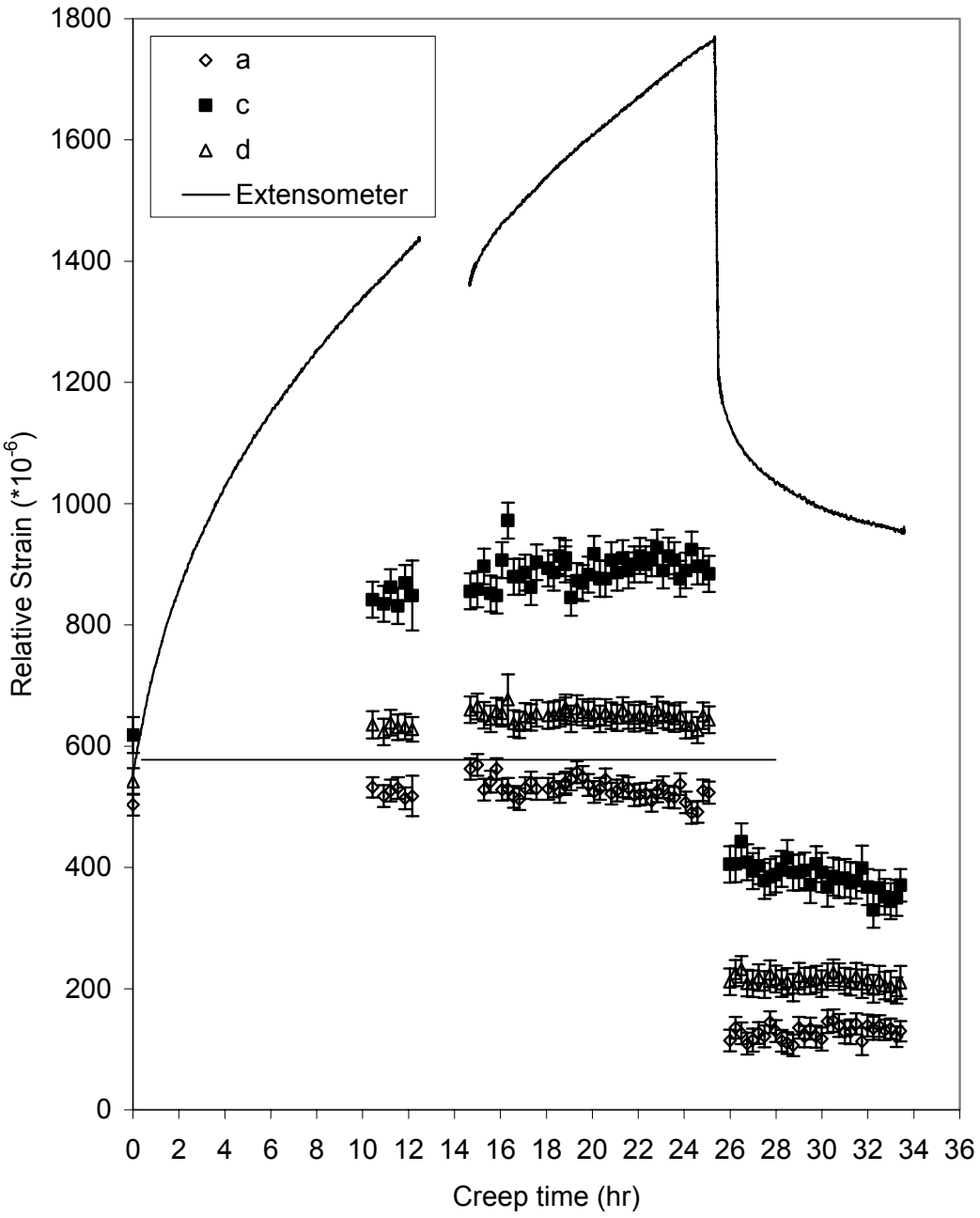

Figure 26. GS-44 creep at 1473 K with 150 MPa applied stress. Longitudinal diffraction data are shown. Strains are relative to data from 25 MPa, 1473 K. Horizontal line indicates the initial *d*-strain at 150 MPa, 1473 K for the 175 MPa test sample (since the first 150 MPa data was lost for this sample).

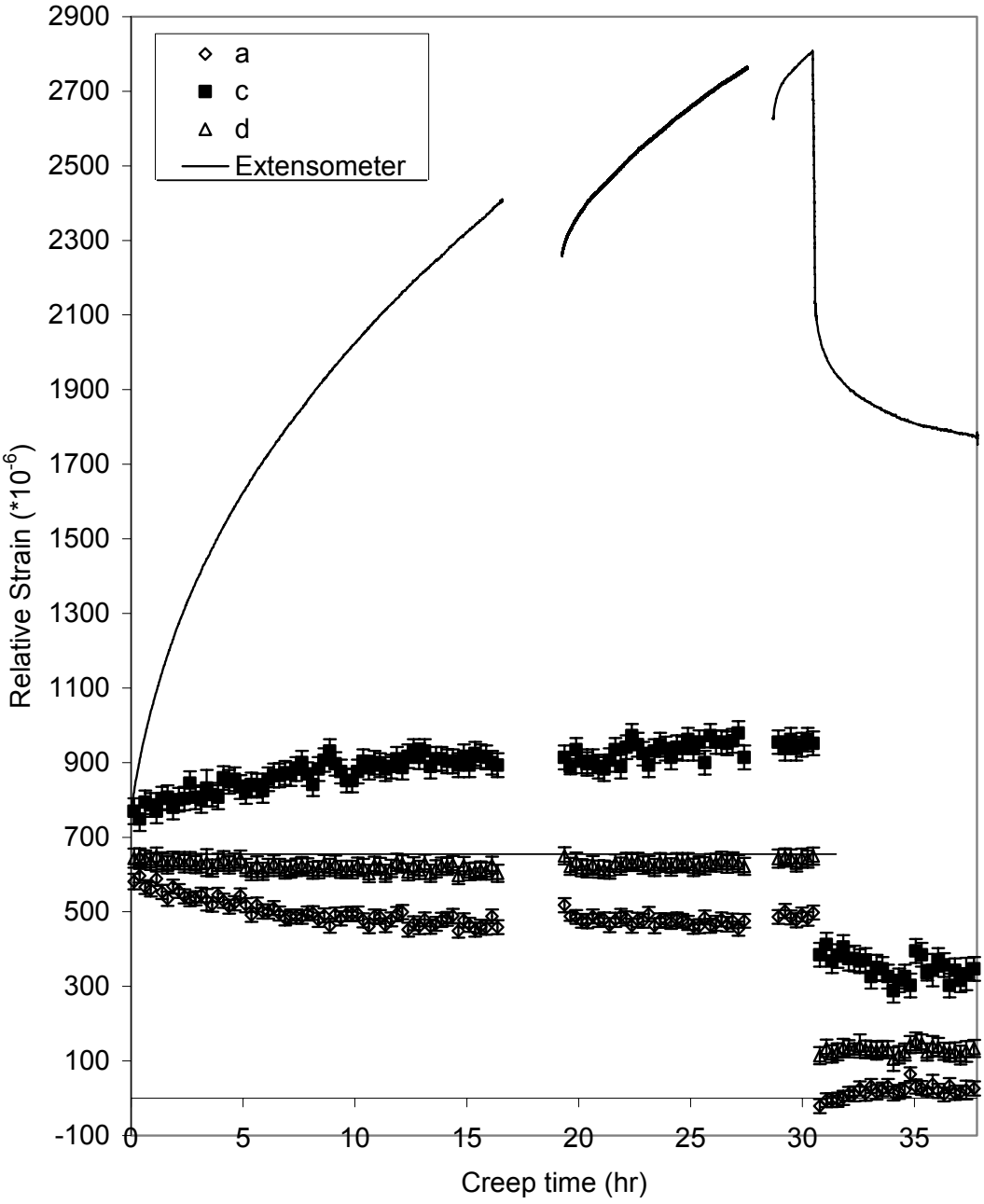

Figure 27. GS-44 creep at 1473 K with 175 MPa applied stress. Longitudinal diffraction data are shown. Strains are relative to data from 25 MPa, 1473 K. Horizontal line indicates the initial *d*-strain at 175 MPa, 1473 K.

Table XV. Comparison of measured strains at 1473 K to Hooke's Law prediction for manufacturer's quoted *E* for 1273 K. Values for *a* and *c* are longitudinal diffraction strains. Recall that the initial 150 MPa strain was lost due to a data collection error.

	Measured strain (με)			
Applied stress (MPa)	**Extensometer**	***a***	***c***	**Hooke's Law**
100	280	180	250	460
125	410	310	400	570
150	550	-	-	680
175	770	580	770	800

The highest temperature for which the manufacturer quotes a value for the Young's modulus is 1273 K, with E = 220 GPa (see Table I), the predicted strains per Equation (27) are shown in Table XV, compared to the measured strains for the extensometer and the lattice parameters from diffraction. The use of Hooke's Law for the calculation of these values requires the assumption that the samples were elastic until the final load was reached, which since creep was observed for all four stresses is uncertain. However, the time was minimized while loading to each final stress value, though the discrepancy between the measured and Hooke's Law values indicate that the effective Young's modulus was not the same as the literature value, in addition to any imposed inelastic effects. The first thing to note in Table XV is the similarity between the extensometer and *c*-axis strains for all applied stresses. This can be noted also in the creep plots of Figures (24)-(27). For σ = 100 and 125 MPa, Hooke's Law indicates that the strain should be higher than measured, while at 175 MPa the predicted strain is not much greater than the measured strain (4% difference). However, since the manufacturer listed the Young's modulus for 1273 K, 200 K below the test temperature for these data, it is

concluded that the samples possessed a Young's modulus greater at 1473 K than expected even at 1273 K. Again, this effect is attributed to the lack of oxygen to reduce the viscosity of the grain boundary phase, as the reported literature value was likely from a test performed in air.

At 100 MPa (Figure 24), after reloading the extensometer strain rate is essentially the same as before the unloading took place, while for each of the higher stresses, the difference after reloading increases with increasing stress. A very interesting result is the trend exhibited by the *a* and *c* strains at constant stress. The *c* strain shows a distinct increase, while the *a* strain a decrease. The effect is more pronounced for the higher stresses, for which the strain is large enough to overshadow the fitting error bars. Unfortunately, the data for the 150 MPa sample were lost, preventing a suitable comparison with the 175 MPa data, which show a distinct trend. Note that, after steady-state creep has begun, the diffraction strains level off, at about 8 hours and later in terms of creep time. Comparing these data with those from the stress step-up test (Figure 23), it can be seen that the longitudinal strain of the *a* axis in that sample was not appreciably different from the behavior seen in the single stress creep tests. However, after unloading and reloading, the diffraction strains returned to their previous levels and remained essentially unchanged. This indicates that whatever had occurred previously during creep was not lost with the unload, nor was any further alteration needed to resume the prior state. Note that the *d* strains plotted in all four creep plots are essentially constant over time. Horizontal lines have been drawn at the initial creep strain (the first diffraction strain value for *d* obtained at the creep stress) value as a guide to the eye. Thus, the

"forking" of the *c* and *a* lattice parameters still preserves the expected constant diffraction strain, since, assuming that everything remains elastic one would expect a constant strain for a constant applied stress. Recall that diffraction only measures elastic lattice strains. The forking, then, is likely an elastic effect in which volume conservation is present, thus the expansion of the shorter *c*-axis is balanced by a contraction along the longer *a*-axis. This shape change of crystallites aligned with the load axis is attributed to the flow and redistribution of the grain boundary phase straining the GS-44 grains. Single peak creep strains are of no use for interpreting this behavior, as the strains have wide scatter and are without a trend. Only the full-pattern derived lattice parameters indicate a pattern, thus the single peak strains are not provided.

The forking of the diffraction strain data is unexpected, and there is nothing similar in the literature. In order to determine if the different behavior is based on geometric considerations, Figure 28 was created. This figure shows, first, the *c*/*a* ratio of the GS-44 sample at 175 MPa, relative to the 25 MPa 1473 K reference data. Obviously, there is an increase over time. However, also shown in Figure 28, and plotted on the secondary *y*-axis, is the volume of the unit cell. The volume was calculated simply based from the lattice parameters for a right regular hexagonal cylinder, and is plotted as the change in that volume relative to the reference data already mentioned. Unlike the creep data plot, this plot shows the data from the patterns obtained during the stress increase. These are the data points with a negative time, which was simply an arbitrary constant value subtracted from the elapsed creep time.

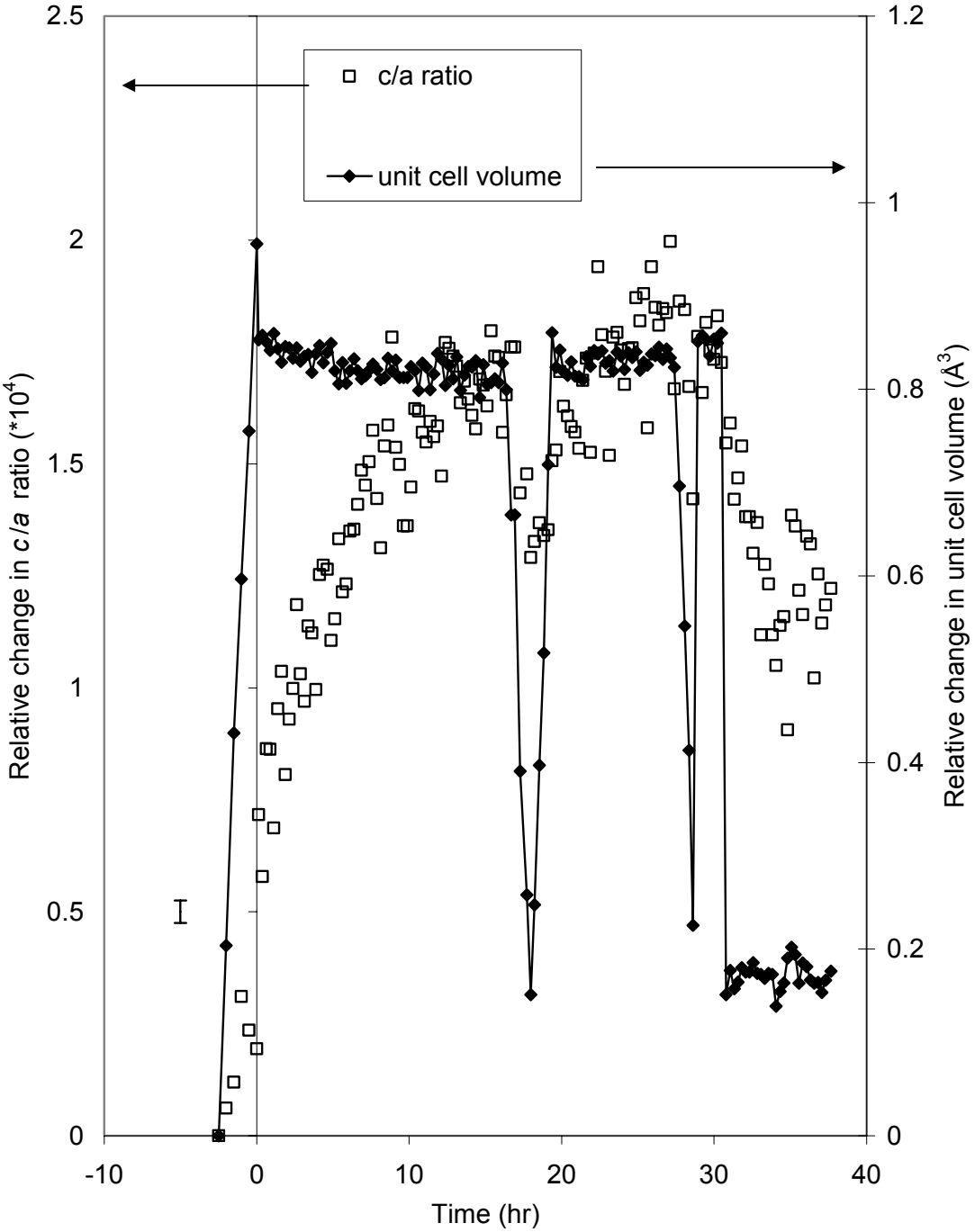

Figure 28. Relative change of *c*/*a* ratio and unit cell volume (relative to 1473 K, 25 MPa diffraction data) for 175 MPa creep of GS-44. Data are from longitudinal 175 MPa creep at 1473 K; typical error bar shown at left (± 5%) is based on error from strains as seen in Figure 27.

From Figure 28 it is interesting to note that after initial application of the 175 MPa stress, the volume change proceeds to decrease from its maximum over the course of the experiment, reaching a constant value at approximately 8 hours creep time, the same time determined as the onset time of steady-state creep. Even after this, the *c*/*a* ratio is seen to increase. Thus, while the *c* axis is experiencing a tensile strain and the *a* axis a compressive strain and increasing the *c*/*a* ratio, the volume has reached a balance. The same is seen to occur after the two unload cycles, though the max volume is less than that of the first stress application, and the relaxation proceeds faster. Thus it is concluded that while the lattice parameters in the longitudinal direction indicate a change, these changes are in fact balancing one another in order to maintain a steady-state volume. This balance perhaps is maintained by the constraint of space in which to expand in the densified GS-44 microstructure, with some change being facilitated by the redistribution of the grain boundary phase. Since the bulk of the diffraction strain occurs in the primary creep regime, when the fastest strain rate is experienced, the grain boundary phase is being strained the most and redistributing the most in that regime. This redistribution will be to move out of the tensile straining GS-44 grains, and relocating to the sides of those grains. This would allow strain to occur in the loading direction, while constraining the lateral direction. Thus, the diffraction data would indicate that the *c* axis is aligned with the loading direction, as that axis expands, while the *a* axis is compressed due to the redistributed grain boundary phase, and the volume of the unit cell reaches a constant value. The reason that strain appears in the pattern is that additional load is transferred to the Si_3N_4 grains as the redistribution allows the grain boundary phase to shed load to the Si_3N_4. As the applied stress is unchanged, this strain would be expected to reach a

maximum value, once the redistribution was functionally complete, as is seen by the reduction of diffraction strain change once secondary creep begins. This supports the notion of creep of Si_3N_4 as postulated by Luecke and Wiederhorn as a redistribution of the grain boundary phase out of the tensile direction due to cavity nucleation and redeposited along the lateral (transverse) sides of grains, since cavitation during tensile creep of Si_3N_4 gives strain in the loading (axial) direction but not a uniform volume expansion [24]. The extensometer creep curves before unloading are plotted together in Figure 29. Unsurprisingly, the creep rate is much faster for the higher stresses than the lower. The steady-state regime is reached earlier for the lower stresses. This agrees with literature data for GS-44 creep. This can be interpreted by realizing that a lower stress cannot perturb the system as much as the higher stress, thus less change is possible before the steady-state condition is reached. Since there is no absolute definition of when steady-state creep begins, it was decided arbitrarily, by fitting a line to the extensometer strain data over a large region while still obtaining a reduced r^2 value. This was between 8 and 10 hours after the creep stress was reached until the (first) unload for the four stresses performed. Note that these steady-state creep rates give a creep exponent of n = 3.18 (see Figure 30, in which the slope of the plotted line is the creep exponent). The discrepancy between this result and the prior result is very likely the effect of time. The stress step-up test did not allow sufficient time for steady-state creep to begin, beyond the 100 MPa stress at least. However, this result is different from that of Wei *et al*., who reported a value of n = 2.24 [25]. It is possible that the preservation of the grain boundary phase properties by the vacuum furnace of SMARTS had some effect. Note that the strains attained in these creep tests is much less than that of Wei *et al*. For

example, at 1473 K and 100 MPa, they reported a creep strain of over 2000 με, while the present results have a creep strain of under 700 με for the same conditions, except for the atmosphere in which the test was performed [25]. Given that the creep rate depends heavily upon the grain boundary phase viscosity, and since the grain boundary phase in the present experiments was not exposed to oxygen, thus suffering no decrease in viscosity, such a result is not wholly unexpected.

Given that the steady-state creep rate is linear with stress, as shown in the log-log plot of Figure 30, the Norton formulation of Equation (4) fits the data well. However, the equation developed by Luecke and Wiederhorn, Equation (7) (repeated below for convenience), predicts a non-linear behavior when plotted on a semi-log basis.

$$\dot{\varepsilon} = A\sigma \exp\left(\frac{-\Delta H}{RT}\right)\frac{f^3}{(1-f)^2}\exp(\alpha\sigma) \qquad (7)$$

However, in this case, the log-log plot would not exhibit the linearity evident in Figure 30. While attempt was made to fit the data on a semi-log basis using the Luecke and Wiederhorn equation, it was necessary to tailor the pre-exponential constant for each stress in order to fit the data with any quality. The constant included the activation energy term, since at a given temperature it is a constant; 75 MPa was used as the critical stress to nucleate a cavity, determining the other exponential term. This value (75 MPa) was chosen because while performing the unloads and reloads during the four creep tests, the extensometer strain at 75 MPa was nearly constant, meaning that no creep was occurring, nor was creep recovery, during the short scan time that 75 MPa was applied.

The pre-exponential constant was determined based on a linear function of the applied stress, namely,

$$A'(\sigma) = 0.08 * \left(\frac{\sigma}{25} - 3 \right) \qquad (28)$$

Given that the volume fraction of the grain boundary phase, *f*, is included in the *A'* formulation of Equation (28), the stress dependence is not wholly unexpected. Given that more cavities should nucleate for a higher stress, then the value of *f* should depend on stress. This formulation was determined by first finding the constant necessary to match the 100 MPa strain rate (the source of the 0.08 term), through a simple iterative approach, then observing that the subsequent strain rates increased relatively linearly. While an empirical relation, it indicates an additional dependence on stress that Equation (7) could not match. Note that if the value of the critical stress is altered from 75 MPa, this would only modify the entire equation by a constant value. Note that the volume fraction of the grain boundary phase was also included in the constant term, as indicated by Luecke and Wiederhorn. Given that this value should not be constant, this is acceptable. The prediction based on Equations (7) and (28) is shown in the semi-log plot of Figure 31. Note that while the data are linear on the log-log plot of Figure 30, there is a very slight curvature evident in the semi-log plot of Figure 31. For GS-44, then, as tested in vacuum, it seems that the Norton Equation (Equation (4)) predicts the steady-state creep rate as well as the Luecke and Wiederhorn equation (Equation (7)). Note that the latter formulation accounts for the viscosity of the grain boundary phase, which is known to behave differently in the present test environment than in air.[24] Again the reduced viscosity decrease, due to vacuum, plays a major role in the creep behavior.

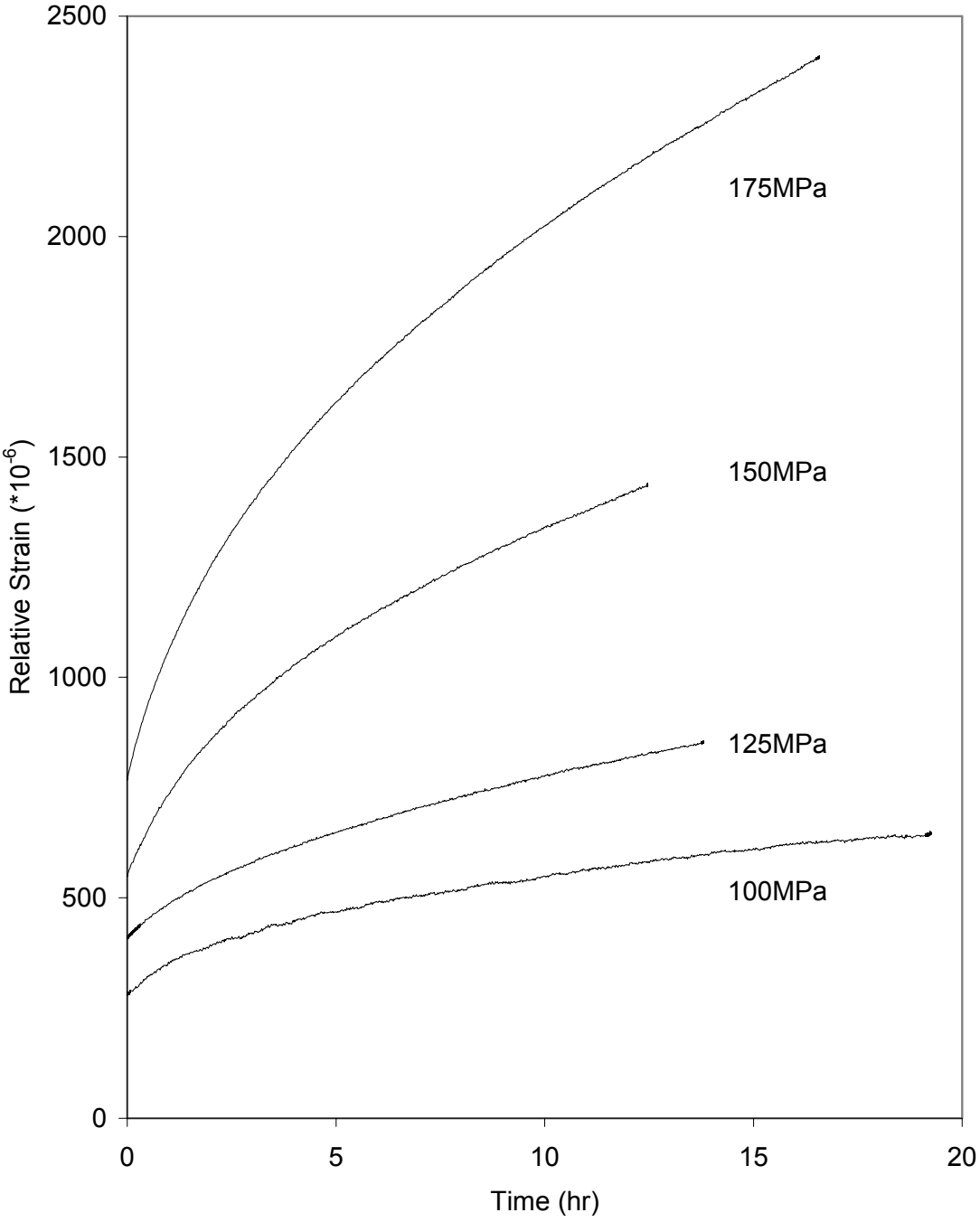

Figure 29. Extensometer creep curves for GS-44 under various applied stresses at 1473 K prior to any unloading-reloading cycle. Strains are relative to the data from 1473 K, 25 MPa for each individual sample.

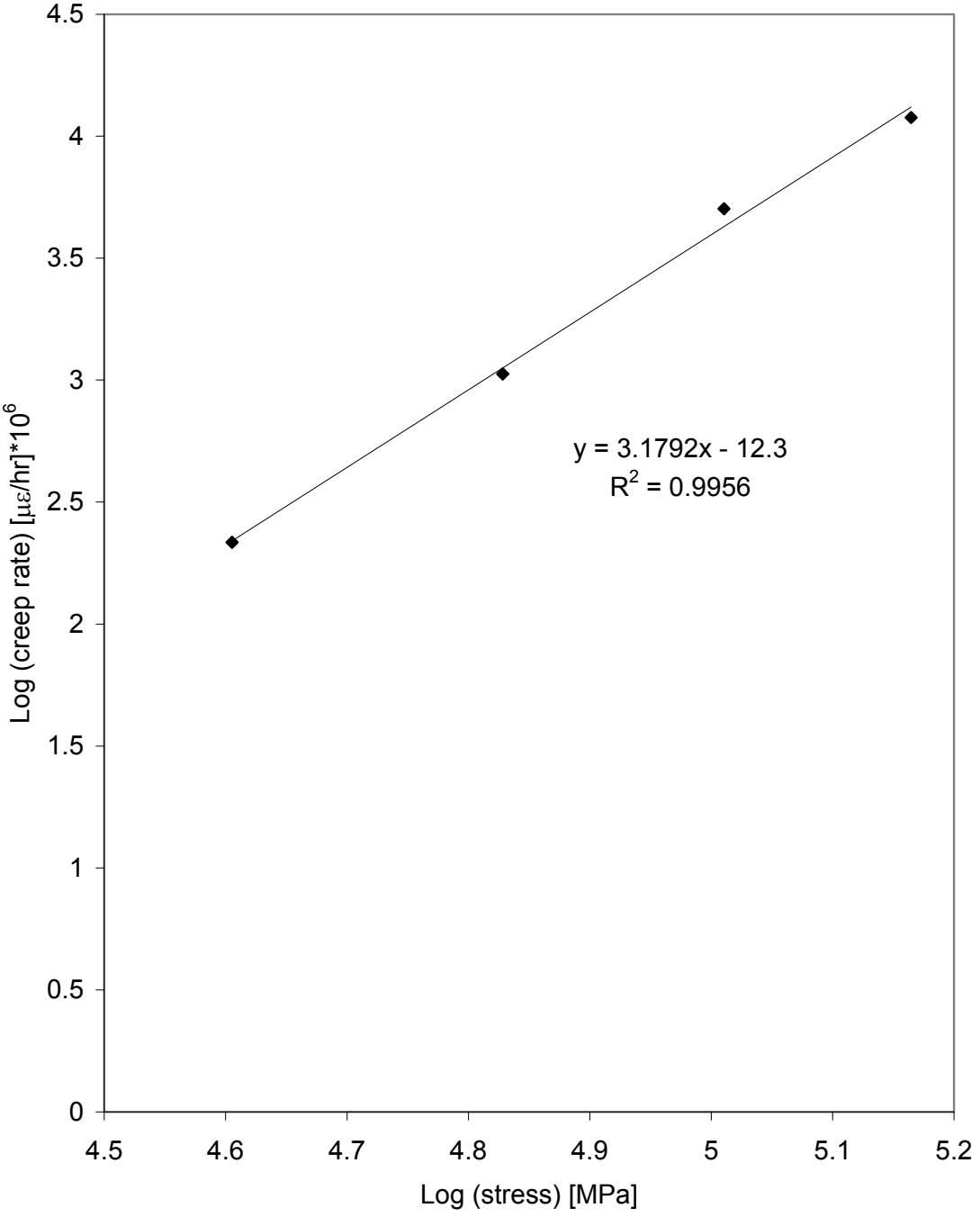

Figure 30. Log-log plot of creep rate versus applied stress for GS-44 at 1473 K. Data are fit as a line, in accord with Equation (5), the classic Norton creep equation. The r^2 for the linear fit is 0.996, with the slope being the creep exponent, n = 3.18.

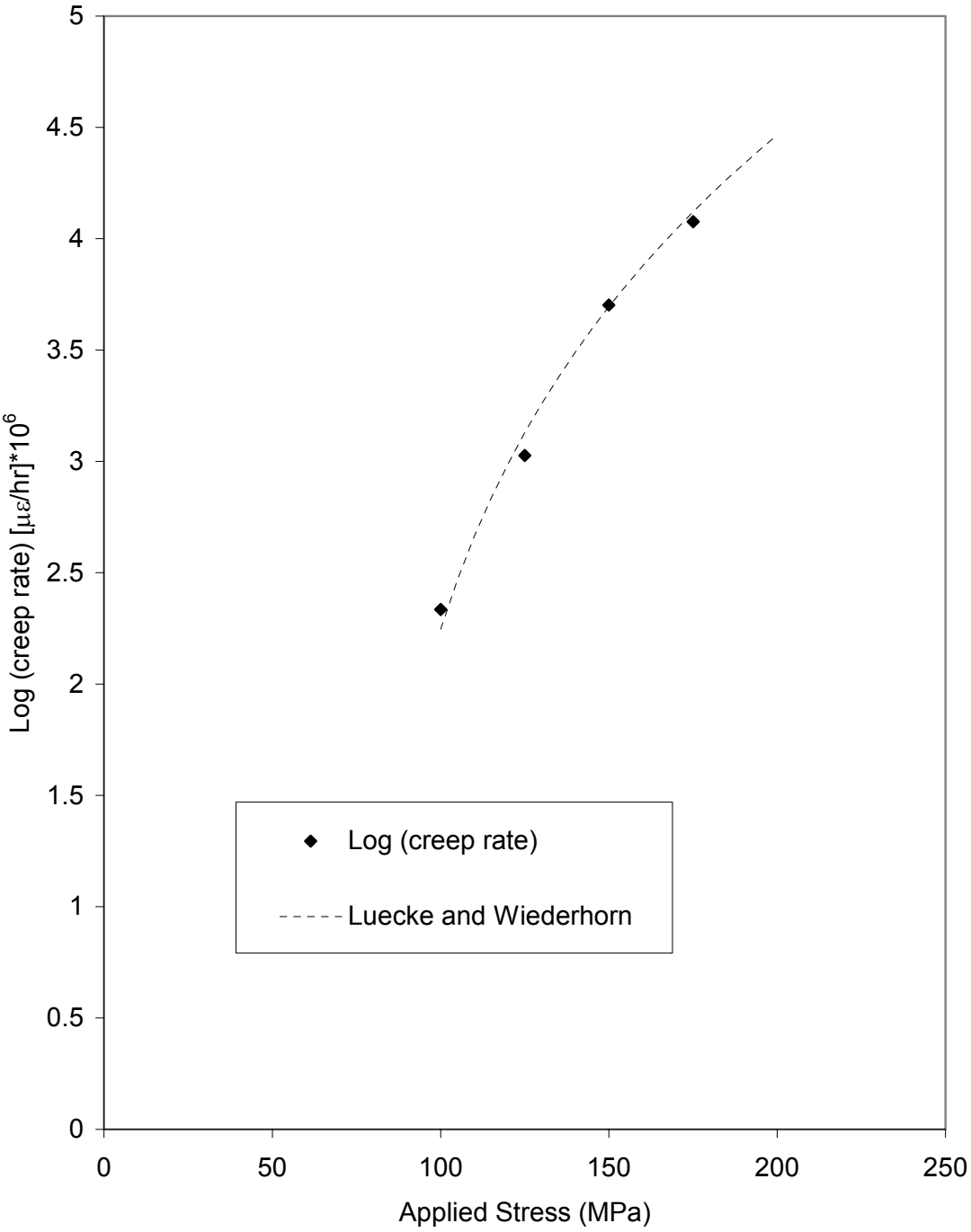

Figure 31. Semi-log plot of creep rate versus applied stress, with data prediction as per Equations (7) and (28). The predicted values approximate the data well (r^2 was calculated as 0.989), but require an additional dependence on the applied stress than indicated.

3.2.2.3. Intra-Creep Elastic Modulus Measurement

During each of the single stress creep experiments, an unload was performed after the steady-state creep regime was entered. Though these tests were not performed at the exact same time for each applied stress, since each took place in the secondary regime, the exact time after which that stage was entered is irrelevant. Each sample was unloaded to 25 MPa, then reloaded to the creep stress. The slopes of the (longitudinal) diffraction data (*a* and *c* lattice parameters) and the extensometer from these various tests are provided in Table XVI. Note that the initial Young's moduli are inconsistent. Recall that the 150 and 175 MPa samples were from one sample source, while the 100 and 125 MPa samples were from a different source. The extensometer data show that even samples from a given batch of material can have varied properties. However, the diffraction data for the 150 and 175 MPa samples are very similar to one another, while the diffraction data for the 100 and 125 MPa samples are not. The increase in Young's modulus from the first loading to the second indicates stiffening has occurred due to creep. The 100 MPa data and the *a* axis data for the 125 MPa are exceptions. This stiffening is also evidenced in the extensometer results, in the same way, though not to the same degree.

The residual strains of GS-44 were also obtained. Note that for several samples, fracture occurred before complete cooling to room temperature, due to load frame malfunctions. Thus, only residual strains at 1473 K after unloading are presented in Table XVII. Residual strains for all four stresses are given, but only longitudinal strains, as the transverse strains, as mentioned, are of dubious quality at best. The presented values are from patterns obtained shortly before cooling, *i.e.*, at the end of the recovery period.

Table XVI. Effective Young's modulus before and during creep of GS-44 at 1473 K as obtained from linear fits to stress-(diffraction and extensometer) strain data measured during loading and unloading cycles. Values in GPa.

Applied Stress	**175 MPa**	**150 MPa**	**125 MPa**	**100 MPa**
a axis				
First load	250	250	320	410
First unload	310	310	300	300
Second load	280	280	300	280
Second unload	330	--	--	--
c axis				
First load	200	200	240	290
First unload	240	280	260	240
Second load	260	280	290	290
Second unload	270	--	--	--
Extensometer				
First load	170	200	240	260
First unload	180	210	240	230
Second load	220	240	250	240
Second unload	180	--	--	--

Table XVII. Residual longitudinal strains for GS-44 after unloading at 1473 K, for various stresses. Values are presented in microstrain (με). GSAS fitting errors are presented under the strain values.

***hkl* or lattice parameter**	**100 MPa**	**125 MPa**	**150 MPa**	**175 MPa**
a	-130 ± 20	-40 ± 20	130 ± 20	30 ± 20
c	80 ± 30	120 ± 30	370 ± 40	350 ± 30
d	-60 ± 20	10 ± 30	210 ± 30	130 ± 20
(02·0)	60 ± 100	-160 ± 120	150 ± 70	0 ± 80
(01·1)	-80 ± 90	190 ± 110	410 ± 70	210 ± 70
(12·0)	-50 ± 100	-170 ± 120	-50 ± 80	110 ± 90
(11·1)	50 ± 40	10 ± 40	170 ± 30	260 ± 30
(13·0)	5 ± 200	-170 ± 180	110 ± 170	-160 ± 170
(03·1)	-200 ± 150	30 ± 170	230 ± 110	400 ± 110
(22·1)	-70 ± 40	-20 ± 50	110 ± 30	170 ± 30
(23·0)	-120 ± 80	50 ± 90	230 ± 70	150 ± 70
(00·2)	70 ± 60	160 ± 60	480 ± 50	450 ± 50

While the tabulated residual strains do not follow a definite trend, *per se*, it is clear that the higher stresses imparted residual strains in GS-44. The residual strains for the 100 MPa sample are either near unchanged or slightly negative, with a slight change for the 125 MPa sample. The 150 and 175 MPa sample residual strains are of noticeably higher magnitude, and are tensile for the most part, even when considering the peak fitting error. This is further corroboration that the samples suffered inelastic strains due to creep.

3.2.3 Room-Temperature Stress Application

As indicated in Table XI, two samples of GS-44 were tested under applied stress at 298 K, both of which were from the first sample batch. The stress-strain curve from the first sample is shown in Figure 32, while the second is shown in Figure 33. Note that some experimental error affected the October 2002 data of Figure 32, as the strain was non-linear. The September 2003 sample, however, exhibited behavior in close agreement with the extensometer (Figure 33); only longitudinal strains are shown. As with prior room temperature tensile tests on SMARTS, the transverse data for the September 2003 sample were erroneous. In this case, the data indicated tensile strains, yielding a negative Poisson's ratio. Some systematic error again precluded stiffness tensor determination; perhaps the use of a special set of room temperature grips caused the error. The September 2003 data gave E_a = 246, E_c = 254, and E_{ext} = 254 GPa. As at 1473 K, the *c* strain more closely matched the extensometer than the *a* strain. However, in this case *a* was more compliant than *c*, unlike AS800 at room temperature, indicating a significant stiffness change with temperature, since the two lattice parameters exhibited comparable stress-strain behavior at 298 K, but not at 1473 K. This is illustrated when comparing the Sept. 2003 room temperature stress-strain data of Figure 33 with the 1473 K stress-strain data of Figures 20 and 21. At room temperature (Figure 33), the two lattice parameters strain similarly, while at high temperature (Figure 21, *e.g.*), the *a* lattice parameter is stiffer than the *c* lattice parameter.

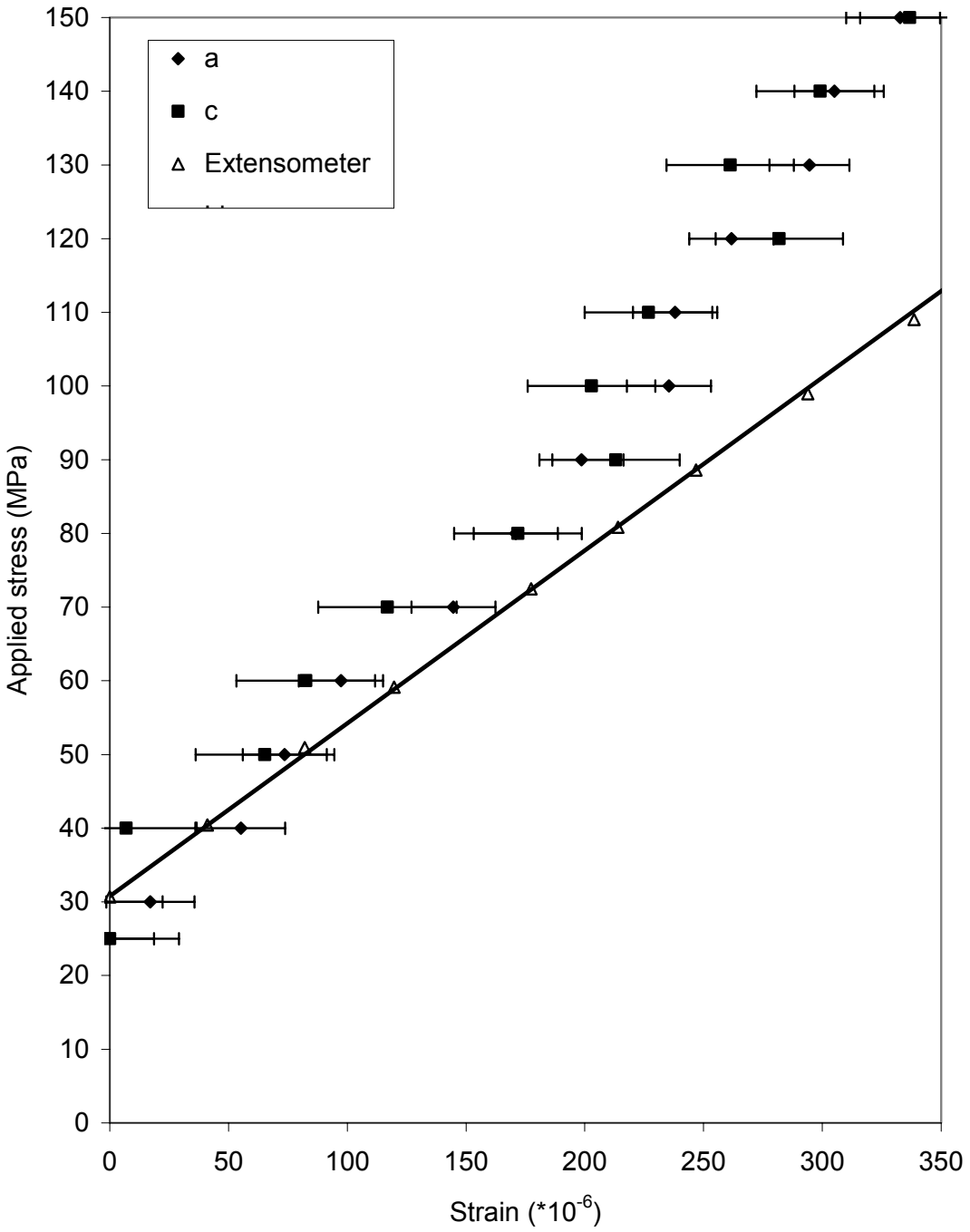

Figure 32. Stress-strain curve from GS-44 at room temperature, October 2002. Linear fit to extensometer data is shown. Error bars based on GSAS fitting residuals are provided.

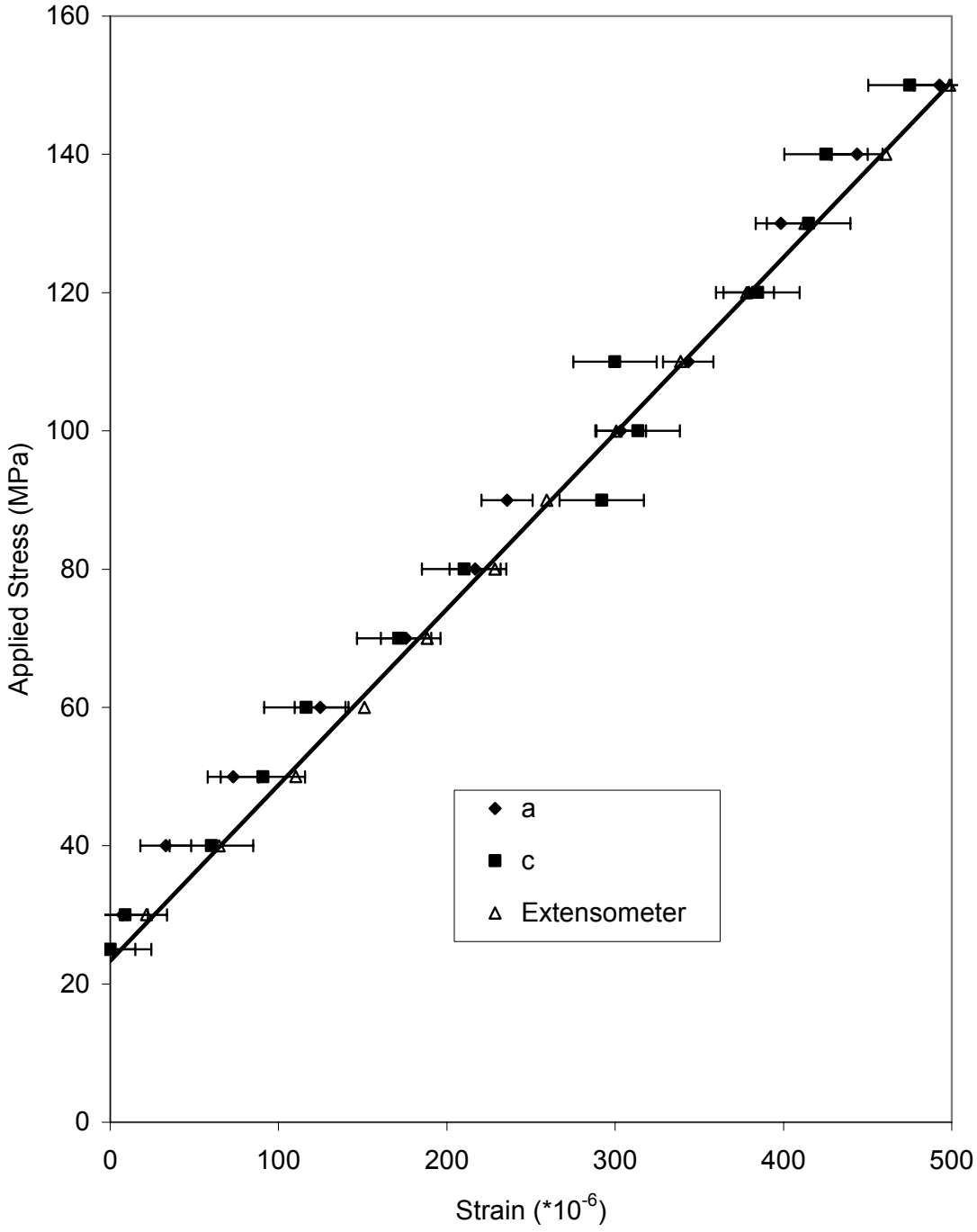

Figure 33. Stress-strain curve from GS-44 at room temperature, September 2003. Linear fit to extensometer data is shown. Error bars based on GSAS fitting residuals are provided.

3.2.4 Ultrasonic Elastic Constant Measurement

Some of the samples tested at high temperature were later examined with the ultrasonic method to determine their elastic constants. The sample that was tested at room temperature on SMARTS was first tested with the ultrasonic method, in order to compare the extensometer and ultrasonic methods. The ultrasonic method is considered in this case to be more precise, since the SMARTS extensometer is less characterized. Table XVIII shows the results of the various samples tested. Note that not all samples measured with SMARTS were tested with the ultrasonic method. While there is a slight difference between the Young's moduli from the various samples tested on SMARTS at 1473 K and compared the sample later tested on SMARTS at room temperature ("RT sample"), the difference is negligible, and all agree with the manufacturer's quoted value of 300 GPa at 298 K within 7% at their maximum scatter. However, given that the ultrasonic method gave 311 GPa and the load frame of SMARTS later gave a value of 254 GPa (for the September 2003 room temperature test shown in Figure 33), a discrepancy greater than 15% from the manufacturer's result, more doubt is cast upon the reliability of the SMARTS load frame at low temperature. Note that the SMARTS data are self-consistent in that the diffraction data agree with the extensometer data. The reason for this notable difference between results obtained at like conditions for the same sample is unresolved as yet. The similar values obtained for all samples tested at room temperature indicates that despite the measured effects at high temperature, upon cooling the grain boundary phase seems no longer the determinate factor in the mechanical response, or that its room temperature properties are unaffected by high temperature

creep, since at room temperature the grain boundary phase is no longer liquid (or at least more viscous).

Table XVIII. Ultrasonic measurement results for room-temperature Young's modulus of GS-44. *E* given in GPa. Samples (except RT sample) were the post-creep-test samples tested at SMARTS (See Figure 8 for dimensions). Error bars are from uncertainty of maxima in ultrasonic measurements. All samples were tested at both the gage center and the grip, with results being the same. Note that there is no literature value for the Poisson's ratio of GS-44.

	RT sample	175 MPa creep	150 MPa creep	Step-up creep
E				
Present results	311 ± 3	307 ± 6	315 ± 4	315 ± 3
Manufacturer	300			
ν				
Present results	0.27 ± 0.01	0.28 ± 0.01	0.28 ± 0.01	0.28 ± 0.01

3.2.5 SEM of GS-44

As described in Section 2.6, effort was made to polish, plasma etch, and examine the microstructure of GS-44 with SEM. Several samples were examined, though there was no observed difference between them, in terms of microstructure. Two samples illustrated best this lack of microstructural effects due to the creep experiments on SMARTS; these were a piece of untested material and a slice of the gage section from the

175 MPa creep sample. Microstructures imaged at like magnifications are provided in Figure 34.

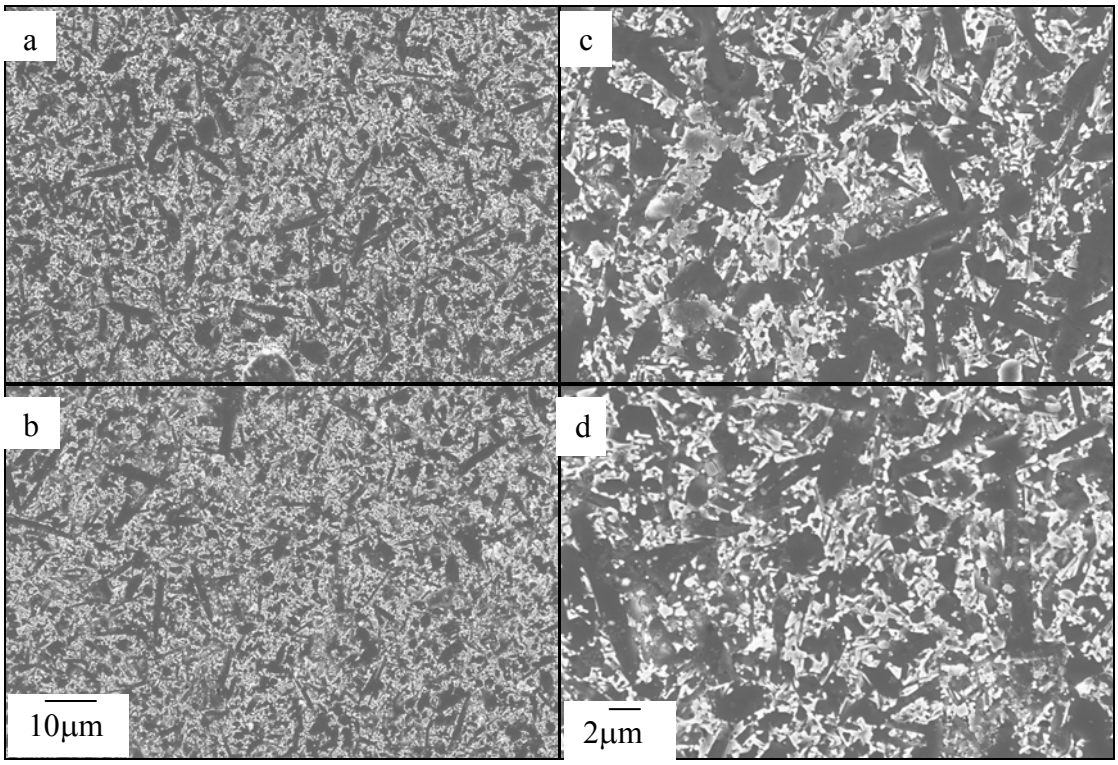

Figure 34. SEM images of GS-44. (a) Untested GS-44 and (b) GS-44 after creep at 175 MPa, 1473 K, both at the same magnification. (c) Untested GS-44 and (d) GS-44 after creep 175 MPa, 1473 K, both at the same magnification. The elongated (acicular) grain structure is plainly visible, and remains random after testing. Grain boundary cavities are not observed.

The grain size and distribution, and the lack of orientation of acicular grains are comparable. There was no indication of cavities in grain boundary regions, though TEM would be a better tool for such than SEM. Note that other researchers perform SEM on

samples after creep experiments with much longer time periods (order(s) of magnitude difference), sometimes reaching tertiary creep. The lack of long time creep experiments in the present research likely reduces the number and size of cavities that can form in the grain boundary phase in any case.

IV. Conclusions

Silicon nitride was subjected to applied stress at high temperature in vacuum. Two different varieties of Si_3N_4 were tested, one (AS800) possessed of a more refractory grain boundary phase than the other (GS-44).

AS800 was subjected to stresses up to 175 MPa at a temperature of 1648 K. While the stress was maintained for a short period of time, there was no indication of incipient creep. Diffraction strains obtained for various applied stresses exhibited linear behavior, and the single crystal elastic stiffness tensor was determined from the behavior of nine individual reflections using the self-consistent method [58-61]. The same nine reflections were used to refine the CTE tensor, using data obtained from various temperatures during the process of heating to 1648 K, with the method of Jessen *et al*. [52]. Both of these tensors yielded satisfactory comparison with literature values for bulk properties of AS800. Room temperature testing of AS800, in attempt to obtain a room temperature stiffness tensor for comparison with the 1648 K stiffness tensor, was unsuccessful. While the diffraction strains from the 1648 K patterns were possessed of linear behavior as a function of applied stress to allow the tensor refinement, the GSAS-derived lattice strains yielded impossible values for elastic properties, while the single peak fits were non-linear in nature. The origin of this behavior is undetermined and may be due to a systematic error, though the fact that GS-44 experiences inelastic behavior under these conditions is the more likely cause of the strange behavior.

GS-44 was tested at 1473 K. Five creep experiments were performed. The first was a stress step-up test, performed initially to determine if creep could be observed with GS-44, since none had been observed with AS800. GS-44 has a less creep-resistant grain boundary composition than AS800 [36], thus creep was in fact observed to occur. The subsequent experiments were single stress creep tests, at 100, 125, 150, and 175 MPa applied stress. For all these experiments, the two lattice parameters of Si_3N_4 were seen to diverge as creep proceeded. The *a* axis indicated a relative compressive strain, while the *c* axis a tensile strain. This was the first observation of a diffraction strain due to creep. As evidenced by the 175 MPa data (Figure 27), the *a* compression was a balancing effect to maintain a constant unit cell volume despite the *c* elongation, as determined through simple geometry (considering the unit cell to be a right regular hexagonal cylinder). This effect is believed to corroborate the notion that the grain boundary phase is flowing and redistributing, with the bulk of this diffraction strain occurring in the primary creep regime and settling to a constant, unchanging level after the secondary creep regime begins. It also suggests that the *c* axis is oriented along the loading direction, despite no indication of texture in the diffraction patterns. The strain measured by diffraction is believed to be additional elastic strain imposed by load shedding from the grain boundary phase to the Si_3N_4 grains as the grain boundary phase redistributes from the loading direction to the lateral sides of grains. The creep exponent was determined from the steady-state creep rates for the four applied stresses, with a value of 3.18 obtained. While this is higher than the creep exponent reported in literature, the vacuum environment is believed to affect the creep rates, as the grain boundary phase viscosity is known to be reduced when creep tested in air. Thus, these experiments are a more true measure of the

creep since there was no contamination by atmospheric oxygen, while experiments in air simulate the service environment and are more realistic for predictions relating to lifetime. While the diffraction strains from stress application were unsatisfactory for determining the elastic stiffness tensor (for either 1473 K or room temperature), patterns obtained from various temperatures during heating allowed determination of the CTE tensor. It was found that the CTE of GS-44 is of greater isotropic character than AS800, evidenced by the smaller aspherism index and the lesser degree of difference between the *11* and *33* tensor components. Thus, upon cooling from processing temperatures, it is expected that there will be a more uniform thermal contraction of GS-44 than AS800, though both will result in residual strain. The different chemistries of their grain boundary phases also will have an effect on residual strain.

Thus, creep experiments on refractory materials are possible on SMARTS. The vacuum environment required that the maximum use temperature per the manufacturer be exceeded, in order to offset the greater viscosity of the grain boundary phase relative to air experiments. Diffraction data acquired from stress application are problematic for obtaining detailed elastic property data, while data from heating experiments are more useful in terms of calculating the CTE tensor. Room temperature loading was unsuccessful, despite multiple attempts with different samples. The use of different grips at room temperature than at high temperatures might be the cause of the poor results obtained.

V. Recommendations for Future Work

- Of paramount importance for future high-temperature creep experiments of GS-44 is performing similar creep experiments as presented here but at differing temperatures. Performing tests at like stresses but different temperatures will allow determination of the activation energy for creep. Given that the creep exponent determined in this research is markedly different from that in literature for this particular variety of Si_3N_4, due to the atmosphere, the activation energy might exhibit unique results as well.

- Determination of the systematic error affecting room temperature measurements is also very important. Clearly, the ability to refine stiffness tensors from applied stress-diffraction strain data exists, as it was done here at high temperature, but all attempts to obtain the same for room temperature met with failure. Then the room temperature stiffness could be compared to the high-temperature stiffness to illustrate temperature effects, for example if specific components degrade with temperature increase.

- Once the ability to refine stiffness tensors is regained, it might be possible to apply an elasto-plastic self-consistent model to interpret the strains due to stress application, and perhaps to develop a similar model to predict creep. This might be possible through adaptation of an existing model, or creation of a new one.

- Perform creep tests on other material systems. While there were difficulties in testing Si_3N_4, it was examined since it is a very important material, technologically. Other materials might undergo creep more easily than either AS800 or GS-44, allowing for faster experimental completion.

References

1. J. B. Wachtman, *Mechanical Properties of Ceramics*, 1996, New York: John Wiley & Sons
2. G. Ziegler, "Thermo-Mechanical Properties of Silicon Nitride and their Dependence on Microstructure," *Materials Science Forum*, **47**, pp. 162-203 (1989)
3. J. J. Melendez-Martinez and A. Dominguez-Rodriguez, "Creep of Silicon Nitride," *Progress in Materials Science*, **49**, pp. 19-107 (2004)
4. D. W. Richerson, *Modern Ceramic Engineering: Properties, Processing and Use in Design*. Revised and Expanded Second ed, 1992, New York: Marcel Dekker, Inc.
5. G. Schwier, G. Nietfeld, and G. Franz, "Production and Characterization of Silicon Nitride Powders," *Materials Science Forum*, **47**, pp. 1-20 (1989)
6. S. Kaza, *Synthesis of Sub-Micron α-Si_3N_4 Powders via Carbothermal Nitridation Using Novel Carbon Coated Silica Precursors*, Southern Illinois University, Carbondale, IL (1998)
7. W. D. Callister, *Materials Science and Engineering: An Introduction*. Third ed, 1994, New York: John Wiley & Sons
8. W. D. Kingery, H. K. Bowen, and D. R. Uhlmann, *Introduction to Ceramics*. 2nd ed, 1976, New York: John Wiley & Sons
9. F. L. Riley, "Reaction Bonded Silicon Nitride," *Materials Science Forum*, **47**, pp. 70-83 (1989)

10. Q. Wei, J. Sankar, and J. Narayan, "Effect of Heat Treatment on Creep Behavior of a Self-Reinforced Silicon Nitride (Si_3N_4)," in *Ceramic Engineering & Science Proceedings*, T. Jessen and E. Üstündag, Editors. 2000, The American Ceramic Society: Westerville, OH, pp. 537-544

11. H. T. Lin, S. B. Waters, K. L. More, J. Wimmer, and C. W. Li, "Evaluation of Creep Property of AS800 Silicon Nitride from As-Processed Surface Regions," in *Ceramic Engineering and Science Proceedings*, M. Singh and T. Jessen, Editors. 2001, American Ceramic Society: Westerville, OH, pp. 175-182

12. M. F. Ashby and D. R. H. Jones, *Engineering Materials I: An Introduction to their Properties and Applications*. Second ed, 1996, Oxford: Butterworth-Heinemann

13. F. Lofaj, S. M. Wiederhorn, and P. R. Jemian, "Tensile Creep in the Next Generation Silicon Nitride," in *Ceramic Engineering and Science Proceedings*, M. Singh and T. Jessen, Editors. 2001, American Ceramic Society: Westerville, OH, pp. 167-174

14. *GS-44 Silicon Nitride Data Sheet*, Honeywell Ceramic Components (2000)

15. *AS800 Silicon Nitride Data Sheet*, Honeywell Ceramic Components (2000)

16. T. Rouxel, "High Temperature Mechanical Behavior of Silicon Nitride Ceramics," *Journal of the Ceramic Society of Japan*, **109**(6), pp. S89-S97 (2001)

17. A. J. N. Dias, J. Duailibi, C. A. Vilardo, T. C. Silva, and M. C. S. Nobrega, "Gas Pressure Sintering Silicon Nitride Ceramics using Rare Earth and Transition Metal as Sintering Aids," in *Ceramic Engineering and Science Proceedings*, E.

Ustundag and G. Fischman, Editors. 1999, American Ceramic Society: Westerville, OH, pp. 475-480

18. A. Bellosi, F. Monteverde, C. Melandri, and S. Guicciardi, "Sintering Behavior, Microstructure and Properties of Fine Silicon Nitride Ceramics," in *Ceramic Microstructures: Control at the Atomic Level*, A. P. Tomsia and A. M. Glaeser, Editors. 1998, Plenum Press: New York, pp. 263-275

19. J. Sankar, G. Choudhury, Q. Wei, V. Vijayrao, and A. D. Kelkar, "A Comparative Study of the Tensile, Fatigue, and Creep Properties of Sintered (SNW-1000 & GS-44) and HIPed (PY-6) Silicon Nitride Ceramics," in *Ceramic Engineering & Science Proceedings*, E. Üstündag and G. Fischman, Editors. 1999, The American Ceramic Society: Westerville, OH, pp. 133-144

20. T. Rouxel, J. C. Sangleboeuf, M. Huger, C. Gault, J. L. Besson, and S. Testu, "Temperature Dependence of Young's Modulus in Si_3N_4-based Ceramics: Roles of Sintering Additives and of SiC-Particle Content," *Acta Materialia*, **50**(7), pp. 1669-1682 (2002)

21. P. F. Becher, H. T. Lin, S. L. Hwang, M. J. Hoffman, and I. W. Chen, "The Influence of Microstructure on the Mechanical Behavior of Silicon Nitride Ceramics," in *Materials Research Society Symposium Proceedings*, I. W. Chen, P. F. Becher, M. Mitomo, G. Petzow, and T. S. Yen, Editors. 1993, MRS: Pittsburgh, PA, pp. 147-158

22. C. J. Gasdaska, "Tensile Creep in an *In-Situ* Reinforced Silicon-Nitride," *Journal of the American Ceramic Society*, **77**(9), pp. 2408-2418 (1994)

23. S. Hampshire, "Oxynitride Glasses and their Properties - an Overview," in *Advanced Ceramics and Composites*. 2003, pp. 155-160

24. W. E. Luecke and S. M. Wiederhorn, "A New Model for Tensile Creep of Silicon Nitride," *Journal of the American Ceramic Society*, **82**(10), pp. 2769-2778 (1999)

25. Q. Wei, J. Sankar, and J. Narayan, "High Temperature Uniaxial Creep Behavior of a Sintered *In Situ* Reinforced Silicon Nitride Ceramics," in *Ceramic Engineering & Science Proceedings*, E. Üstündag and G. Fischman, Editors. 1999, The American Ceramic Society: Westerville, OH, pp. 463-470

26. Q. Wei, J. Sankar, and J. Narayan, "Microstructural Changes Due to Heat-treatment of Annealing and their Effect on the Creep Behavior of Self-Reinforced Silicon Nitride Ceramics," *Materials Science and Engineering*, **A299**, pp. 141-151 (2001)

27. W. R. Cannon and T. G. Langdon, "Creep of Ceramics Part 1: Mechanical Characteristics," *Journal of Materials Science*, **18**, pp. 1-50 (1983)

28. Q. Jin, D. S. Wilkinson, G. C. Weatherly, W. E. Luecke, and S. M. Wiederhorn, "Thickness Alteration of Grain-Boundary Amorphous Films during Creep of a Multiphase Silicon Nitride Ceramic," *Journal of the American Ceramic Society*, **84**(6), pp. 1296-1300 (2001)

29. C. W. Li and F. Reidinger, "Microstructure and Tensile Creep Mechanisms of an *In Situ* Reinforced Silicon Nitride," *Acta Materialia*, **45**(1), pp. 407-421 (1997)

30. F. Lofaj, A. Okada, and H. Kawamoto, "Cavitational Strain Contribution to Tensile Creep in Vitreous Bonded Ceramics," *Journal of the American Ceramic Society*, **80**(6), pp. 1619-1623 (1997)

31. F. Lofaj, A. Okada, H. Usami, and H. Kawamoto, "Creep Damage in an Advanced Self-Reinforced Silicon Nitride: Part I, Cavitation in the Amorphous Boundary Phase," *Journal of the American Ceramic Society*, **82**(4), pp. 1009-1019 (1999)

32. W. E. Luecke, S. M. Wiederhorn, B. J. Hockey, and G. G. Long, "Cavity Evolution during Tensile Creep of Si_3N_4," in *Materials Research Society Symposium Proceedings*, I. W. Chen, P. F. Becher, M. Mitomo, G. Petzow, and T. S. Yen, Editors. 1993, MRS: Pittsburgh, PA, pp. 467-472

33. J. A. Schneider and A. K. Mukherjee, "Microstructural Evaluation of Deformation Mechanisms in Silicon Nitride Ceramics," in *Ceramic Microstructures: Control at the Atomic Level*, A. P. Tomsia and A. M. Glaeser, Editors. 1998, Plenum Press: New York, pp. 787-794

34. M. K. Cinibulk and H.-J. Kleebe, "Grain-Boundary Films in a Silicon Nitride Ceramic at High Temperatures," in *Ceramic Microstructures: Control at the Atomic Level*, A. P. Tomsia and A. M. Glaeser, Editors. 1998, Plenum Press: New York, pp. 123-130

35. A. A. Wereszczak, M. K. Ferber, and T. P. Kirkland, "Effects of Oxidation and Creep Damage Mechanisms on Creep Rupture Behavior in HIPed Silicon Nitrides," in *Ceramic Engineering & Science Proceedings*, K. V. Logan, Editor. 1994, American Ceramic Society: Westerville, OH, pp. 49-56

36. H. T. Lin, Personal Communication, 2003

37. G. E. Bacon, *Neutron Diffraction*. Third ed, 1975, Oxford: Clarendon Press

38. B. Fultz and J. Howe, *Transmission Electron Microscopy and Diffractometry of Materials*, 2001, New York: Springer

39. B. D. Cullity and S. R. Stock, *Elements of X-Ray Diffraction*. Third ed, 2001, Upper Saddle River, NJ: Prentice Hall

40. B. Clausen, *Characterisation of Polycrystal Deformation by Numerical Modelling and Neutron Diffraction Measurements*, Riso National Laboratory, Roskilde, Denmark (1997)

41. I. C. Noyan and J. B. Cohen, *Residual Stress, Measurement by Diffraction and Interpretation*, 1987, New York: Springer-Verlag

42. H. M. A. Winand, A. F. Whitehouse, and P. J. Withers, "An Investigation of the Isothermal Creep Response of Al-based Composites by Neutron Diffraction," *Materials Science and Engineering*, **A284**, pp. 103-113 (2000)

43. A. Madgwick, T. Mori, and P. J. Withers, "Model-Neutron Diffraction Strain Measurement Comparisons for Steady State Creep of Metal Matrix Composites," *Mat. Sci. and Eng.*, **A285**, pp. 408-411 (2000)

44. A. Madgwick, T. Mori, and P. J. Withers, "A Neutron Diffraction Study of Creep and Damage Occurrence in an A359/SiC Composite," *Materials Science and Engineering*, **A333**, pp. 232-238 (2002)

45. M. R. Daymond, C. Lund, M. A. M. Bourke, and D. Dunand, "Elastic Phase-Strain Distribution in a Particulate-Reinforced Metal-Matrix Composite Deforming by Slip or Creep," *Metallurgical and Materials Transactions*, **A30**, pp. 2989-2997 (1999)

46. H. Choo, P. Rangaswamy, and M. A. M. Bourke, "Internal Strain Evolution during Heating of Ti-6Al-4V/SCS-6 Composite," *Scripta Materialia*, **42**(2), pp. 175-181 (1999)

47. H. Choo, P. Rangaswamy, M. A. M. Bourke, and J. M. Larsen, "Thermal Expansion Anisotropy in a Ti-6Al-4V/SiC Composite," *Materials Science and Engineering*, **A325**(1-2), pp. 236-241 (2002)

48. P. Rangaswamy, M. B. Prime, M. Daymond, M. A. M. Bourke, B. Clausen, H. Choo, and N. Jayaraman, "Comparison of Residual Strains Measured by X-ray and Neutron Diffraction in a Titanium (Ti-6Al-4V) Matrix Composite," *Materials Science and Engineering*, **A259**(2), pp. 209-219 (1999)

49. B. A. Latella, B. H. O'Connor, and B. A. Hunter, "*In Situ* High Temperature Neutron Diffraction Study of a Liquid-Phase-Sintered Alumina Ceramic," *Journal of Materials Science Letters*, **17**(5), pp. 349-353 (1998)

50. M. A. M. Bourke, D. C. Dunand, and E. Ustundag, "SMARTS - a Spectrometer for Strain Measurement in Engineering Materials," *Applied Physics A-Materials Science & Processing*, **74**, pp. S1707-S1709 (2002)

51. R. O. Nelson, M. A. M. Bourke, P. S. Bowling, G. M. Cooper, T. Kozlowski, P. D. Lara, C. R. Rose, J. J. Ross, J. R. Seal, and B. C. Williams, "The LANSCE Data Acquisition System and SMARTS," *IEEE Transactions on Nuclear Science*, **47**(2), pp. 75-79 (2000)

52. S. M. Jessen and H. Kuppers, "The Precision of Thermal-Expansion Tensors of Triclinic and Monoclinic Crystals," *Journal of Applied Crystallography*, **24**, pp. 239-242 (1991)

53. A. C. Larson and R. B. v. Dreele, *GSAS-General Structure Analysis System, LAUR 86-748*, Los Alamos National Laboratory (1986)

54. H. M. Rietveld, "A Profile Refinement Method for Nuclear and Magnetic Structures," *Journal of Applied Crystallography*, **2**, pp. 65-71 (1969)

55. P. Villars and L. D. Calvert, *Pearson's Handbook of Crystallographic Data for Intermetallic Phases I*. Vol. 3, 1985, Metals Park, OH: American Society for Metals, 2790

56. G. A. Swift, E. Ustundag, B. Clausen, M. A. M. Bourke, and H. T. Lin, "High-Temperature Elastic Properties of *In Situ*-Reinforced Si_3N_4," *Applied Physics Letters*, **82**(7), pp. 1039-1041 (2003)

57. D. E. Sands, *Vectors and Tensors in Crystallography*, 1982, New York: Dover Publications Inc.

58. B. Clausen, T. Lorentzen, M. A. M. Bourke, and M. R. Daymond, "Lattice Strain Evolution during Uniaxial Tensile Loading of Stainless Steel," *Materials Science and Engineering*, **A259**, pp. 17-24 (1999)

59. B. Clausen, T. Lorentzen, and T. Leffers, "Self-Consistent Modelling of the Plastic Deformation of FCC Polycrystals and Its Implications for Diffraction Measurements of Internal Stresses," *Acta Materialia*, **46**, pp. 3087-3098 (1998)

60. P. A. Turner and C. N. Tomé, "A Study of Residual-Stresses in Zircaloy-2 with Rod Texture," *Acta Metallica Materialia*, **42**, pp. 4143-4153 (1994)

61. T. M. Holden, R. A. Holt, and C. N. Tomé, "Intergranular Strains in Inconel-600," *Materials Science and Engineering*, **A282**, pp. 131-136 (2000)

62. R. Vogelgesang and M. Grimsditch, "The Elastic Constants of Single Crystal β-Si_3N_4," *Applied Physics Letters*, **76**(13), pp. 982-984 (2000)

63. T. Gnäupel-Herold, P. C. Brand, and H. J. Prask, "Calculation of Single-Crystal Elastic Constants for Cubic Crystal Symmetry from Powder Diffraction Data," *Journal of Applied Crystallography*, **31**, pp. 929-935 (1998)

64. G. Elssner, H. Hoven, G. Kiessler, and P. Wellner, *Ceramics and Ceramic Composites: Materialographic Preparation*, 1999, New York: Elsevier

Appendix

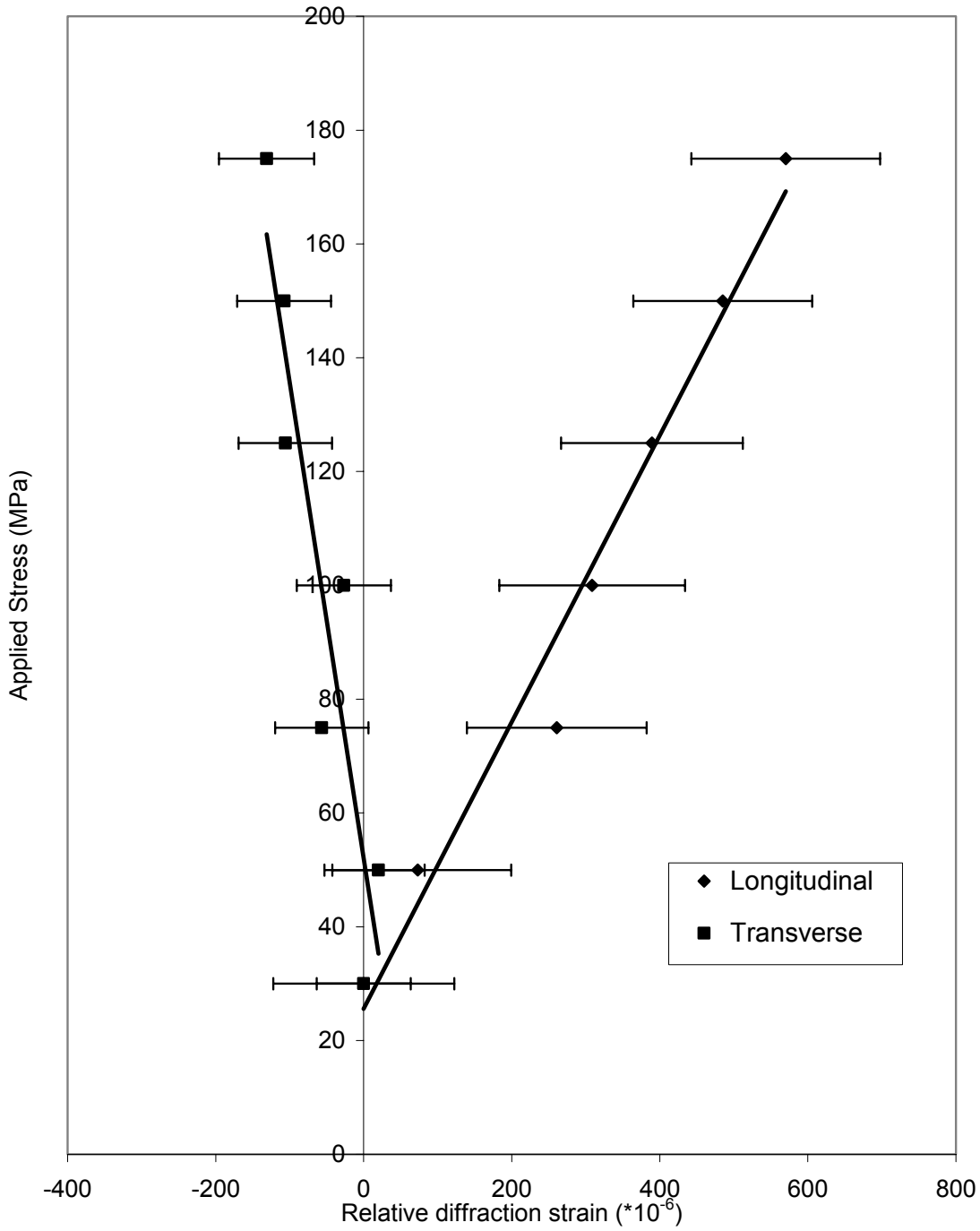

Figure A1. Stress versus strain for (02·0) reflection of AS800, both directions. Linear fits used to obtain the data in Table VI are shown.

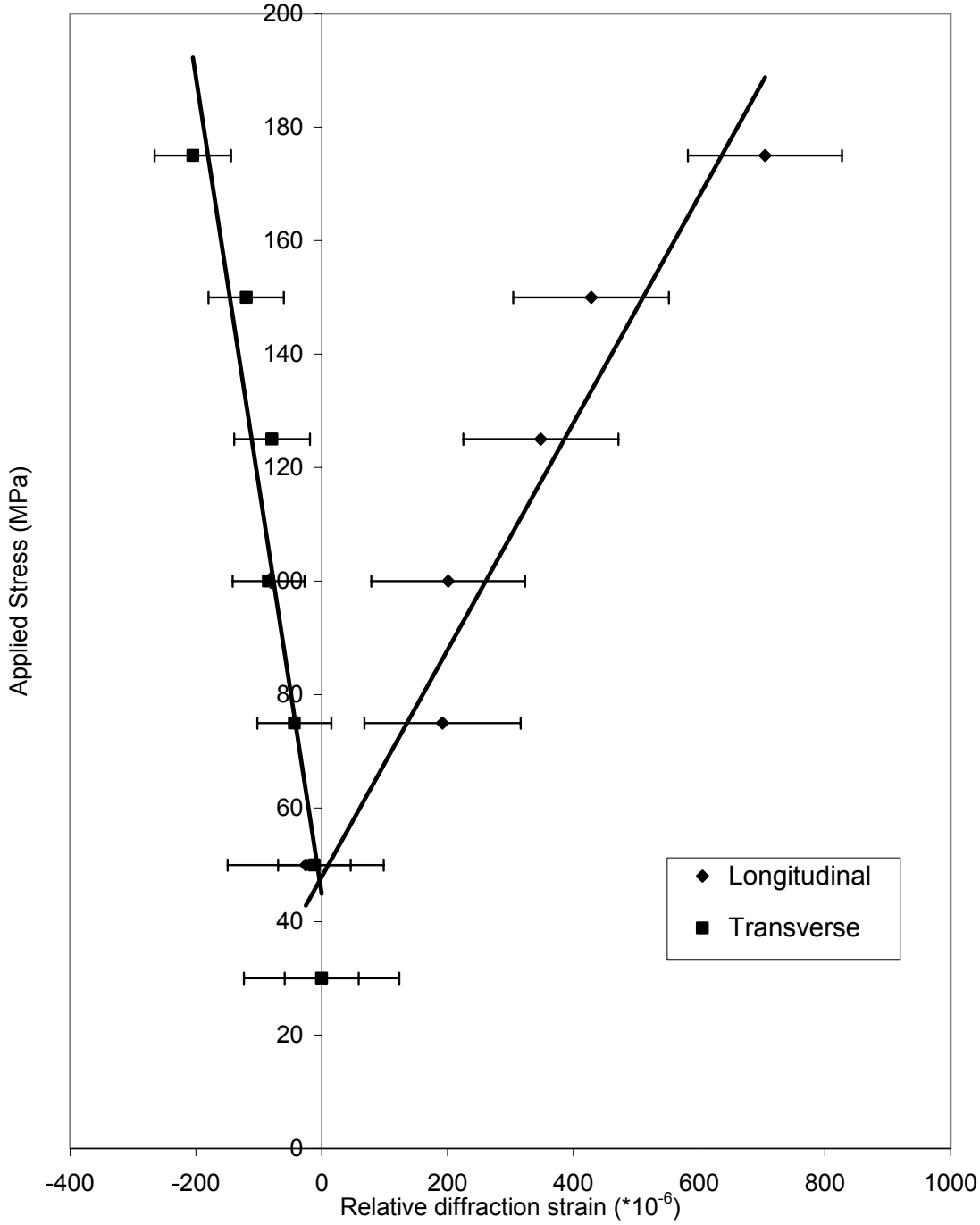

Figure A2. Stress versus strain for (01·1) reflection of AS800, both directions. Linear fits used to obtain the data in Table VI are shown.

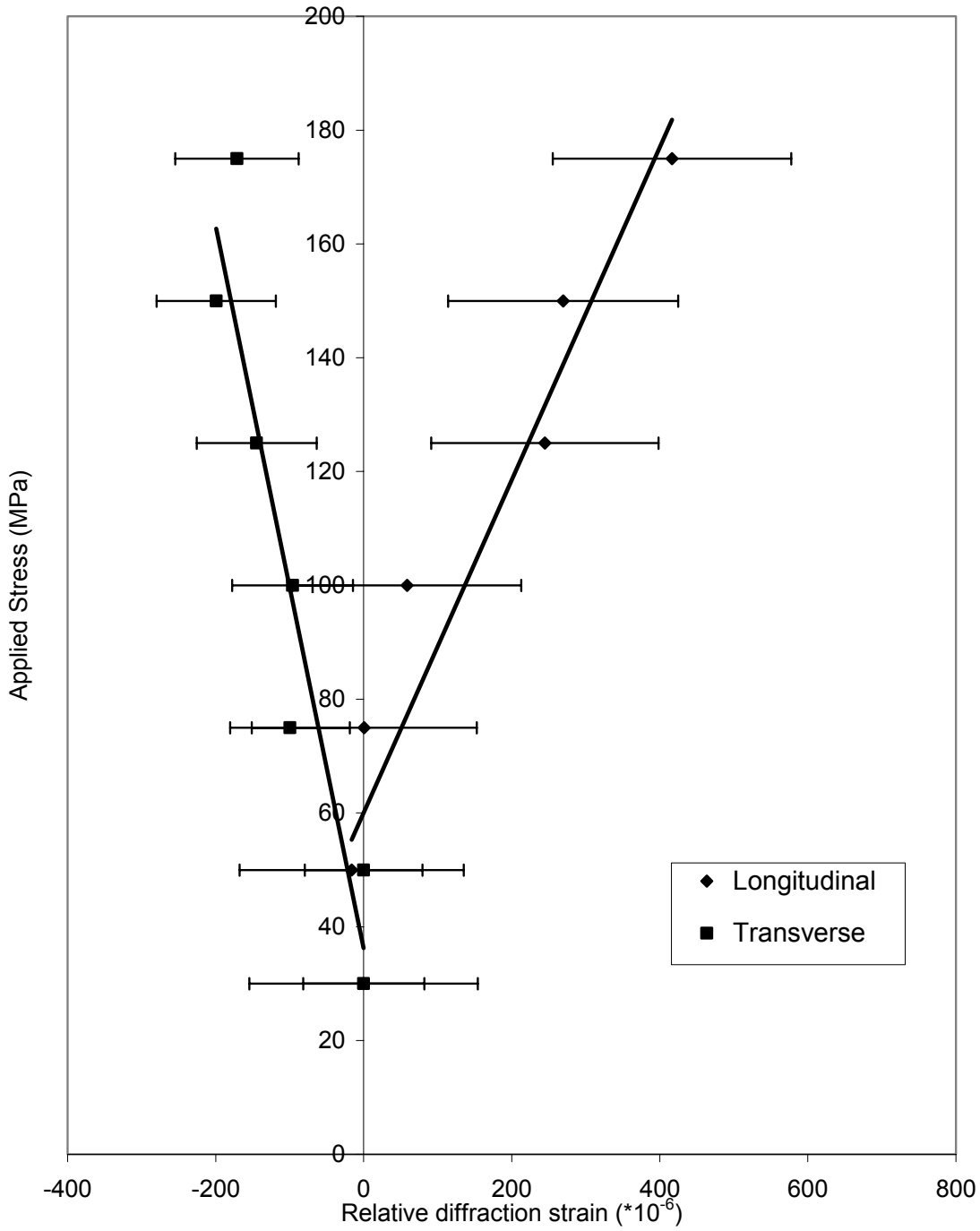

Figure A3. Stress versus strain for (12·0) reflection of AS800, both directions. Linear fits used to obtain the data in Table VI are shown.

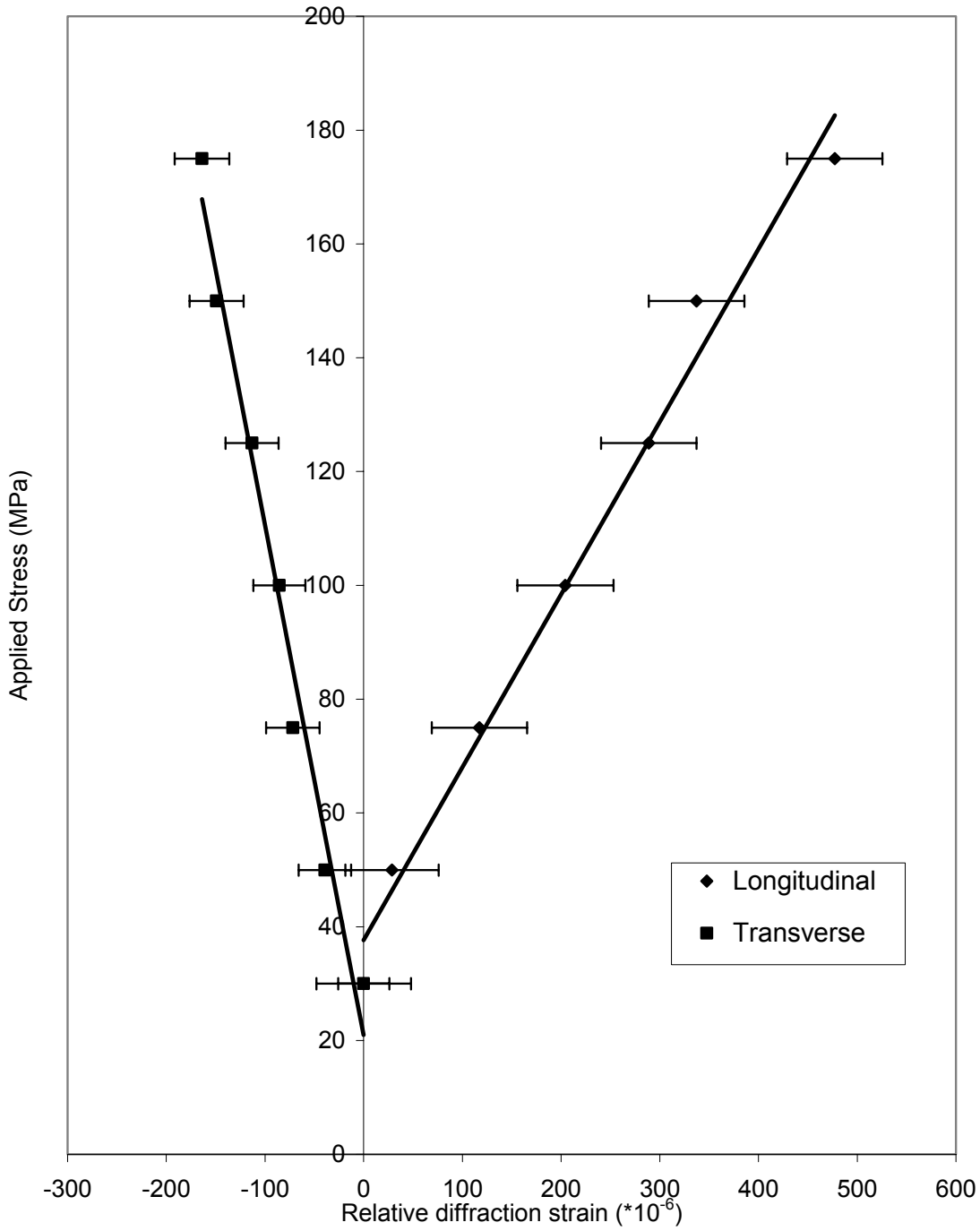

Figure A4. Stress versus strain for (11·1) reflection of AS800, both directions. Linear fits used to obtain the data in Table VI are shown.

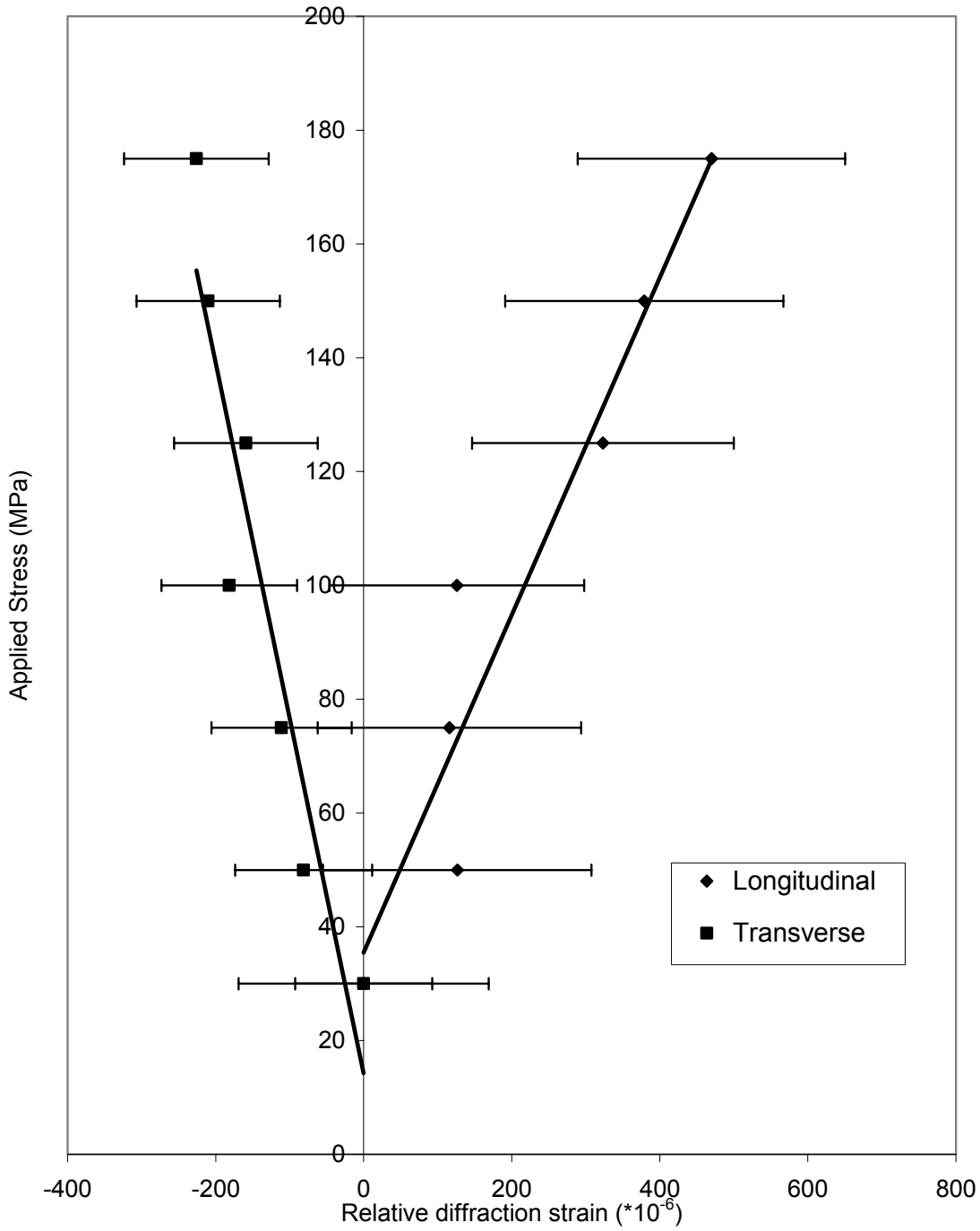

Figure A5. Stress versus strain for (13·0) reflection of AS800, both directions. Linear fits used to obtain the data in Table VI are shown.

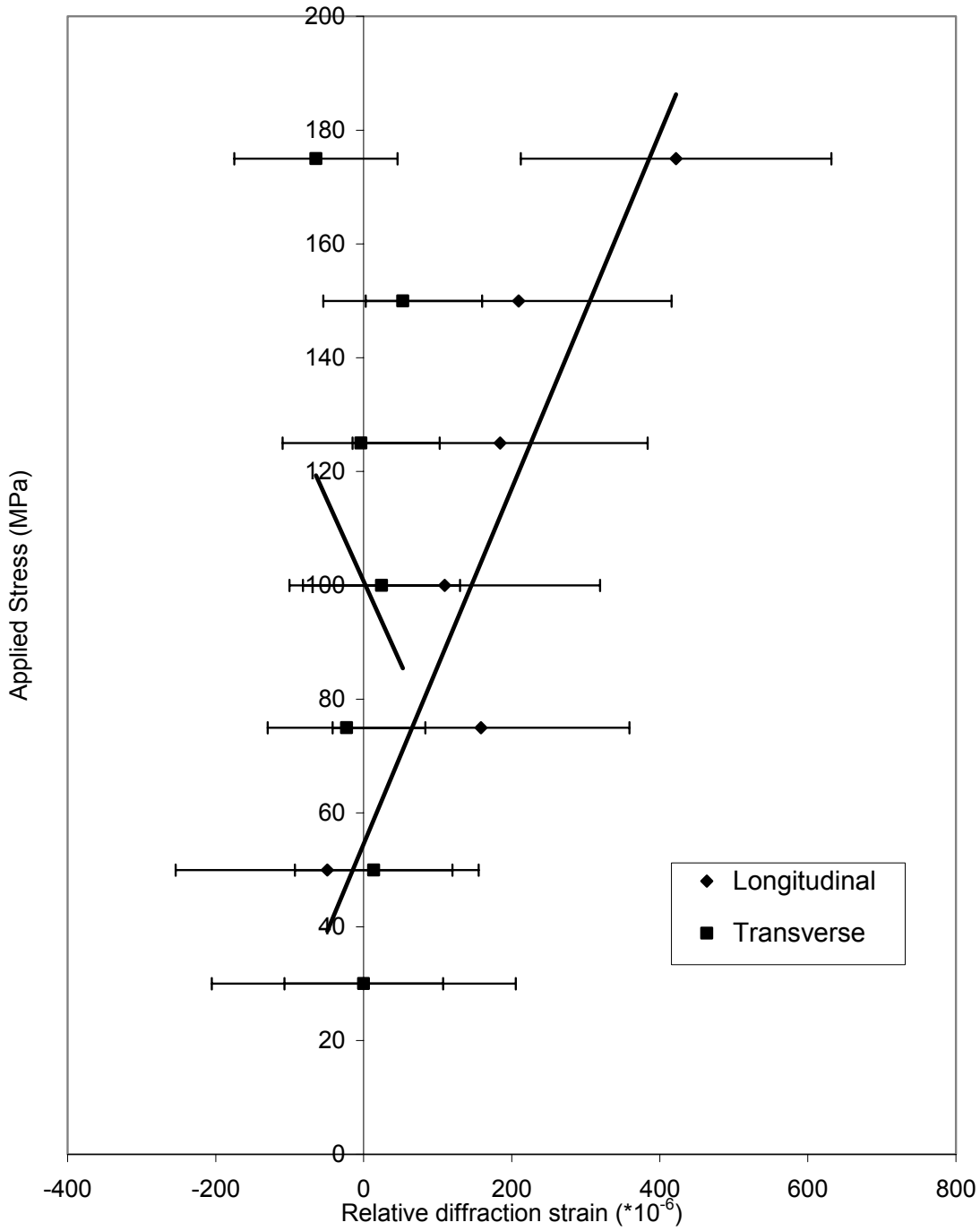

Figure A6. Stress versus strain for (03·1) reflection of AS800, both directions. Linear fits used to obtain the data in Table VI are shown.

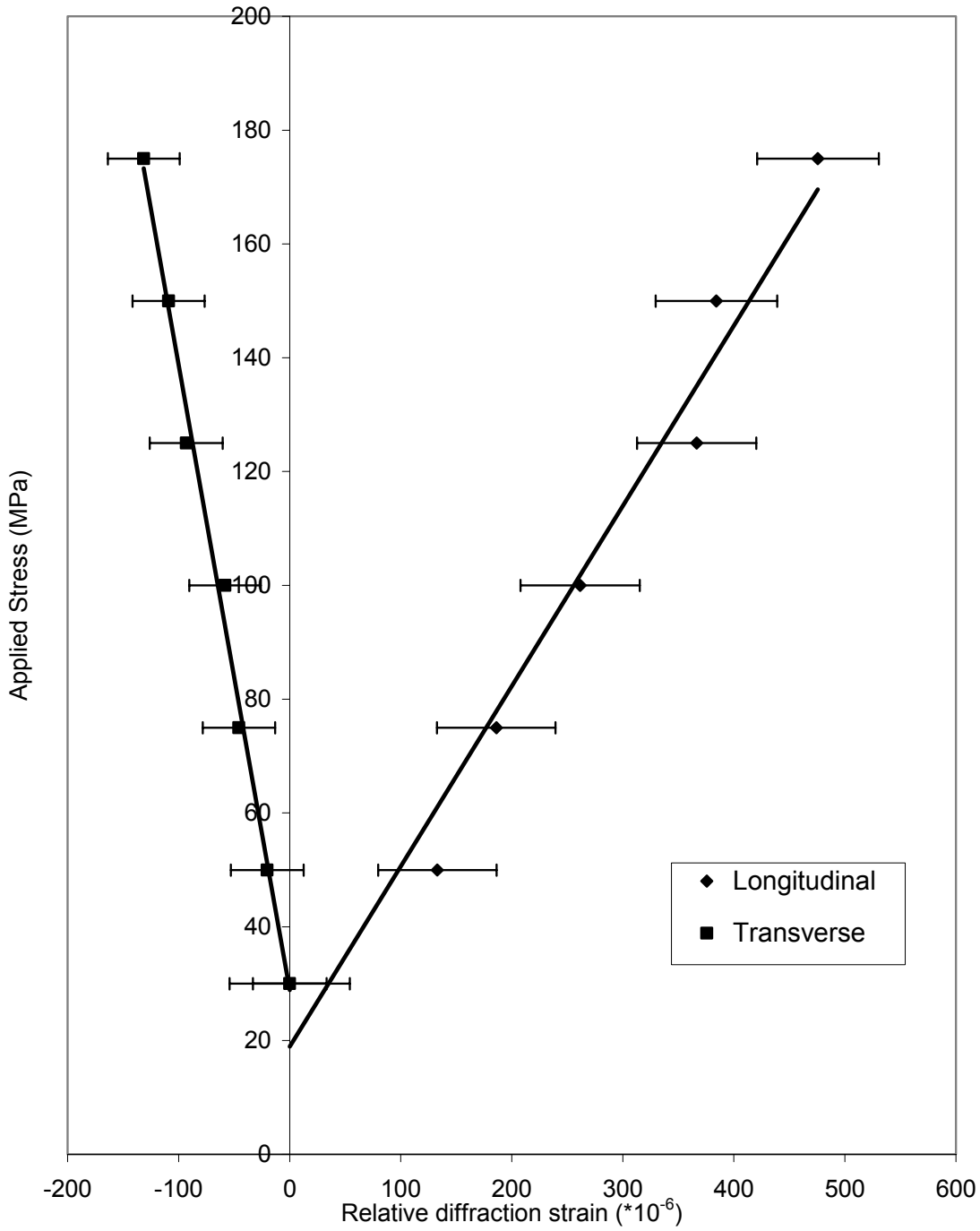

Figure A7. Stress versus strain for (22·1) reflection of AS800, both directions. Linear fits used to obtain the data in Table VI are shown.

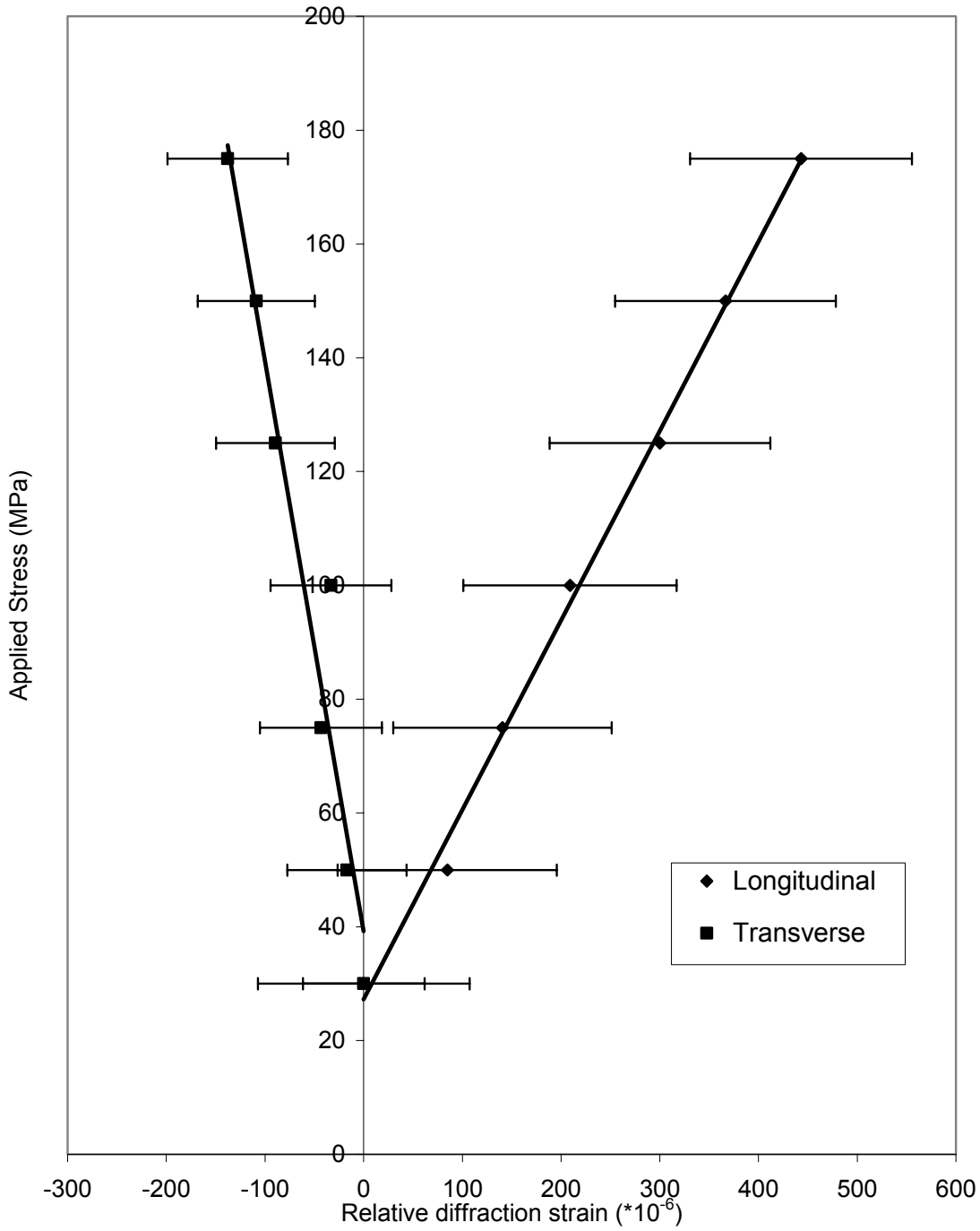

Figure A8. Stress versus strain for (23·0) reflection of AS800, both directions. Linear fits used to obtain the data in Table VI are shown.

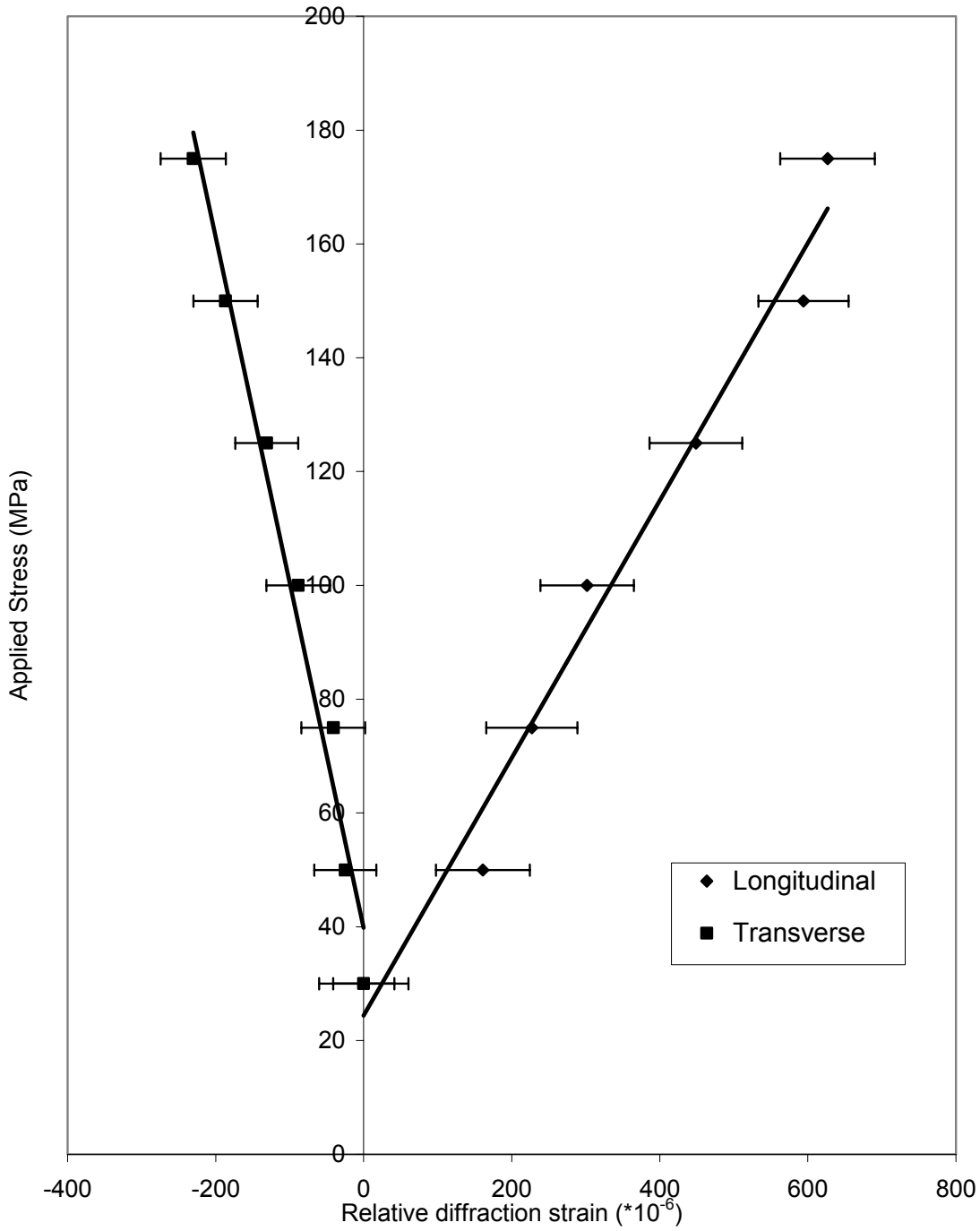

Figure A9. Stress versus strain for (23·0) reflection of AS800, both directions. Linear fits used to obtain the data in Table VI are shown.

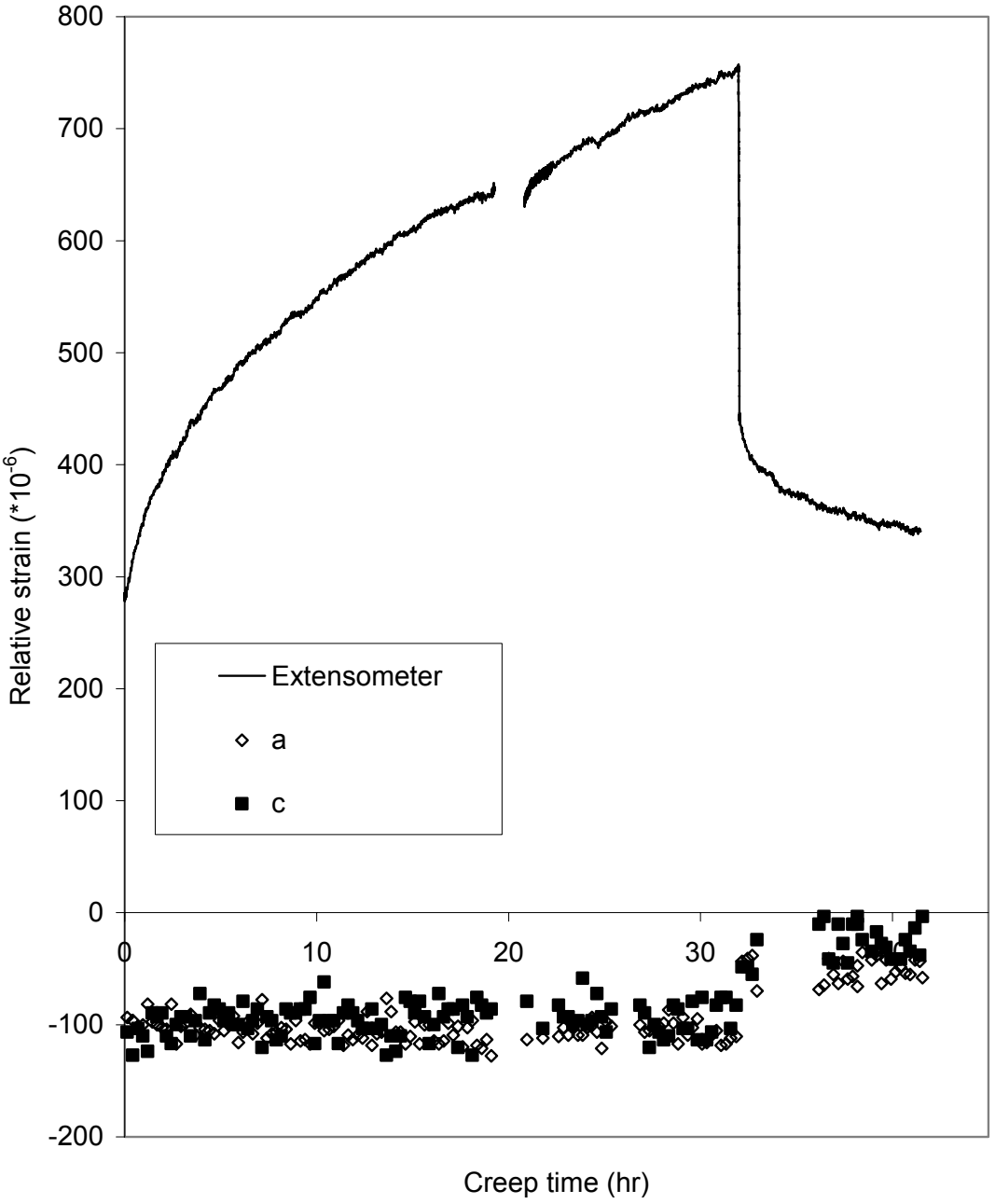

Figure A10. Transverse diffraction strain for GS44 at 1200°C under an applied creep stress of 100 MPa. Error bars are omitted for clarity. Typical error bar values were 17 με for *a* and 30 με for *c*.

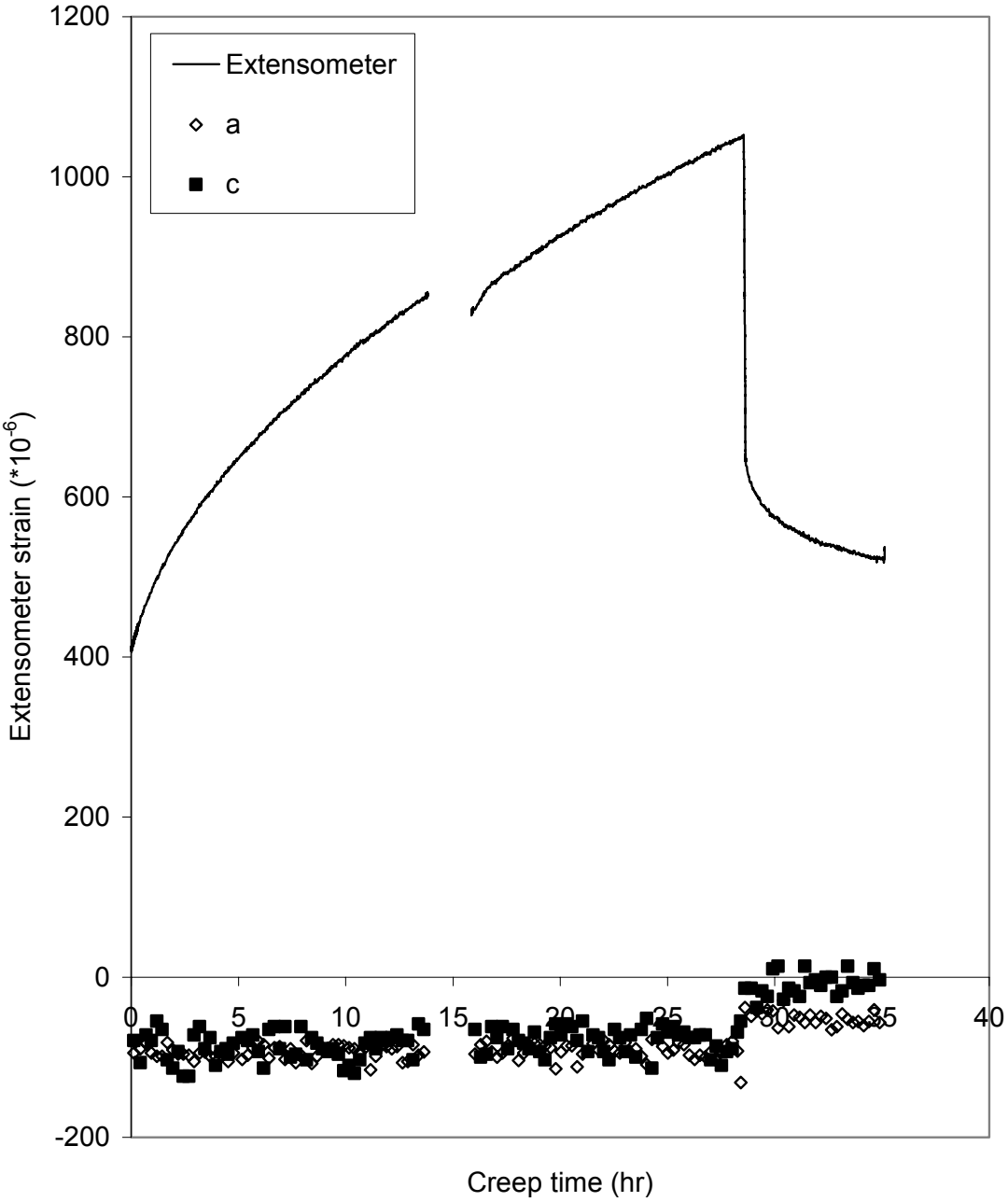

Figure A11. Transverse diffraction strain for GS44 at 1200°C under an applied creep stress of 125 MPa. Error bars are omitted for clarity. Typical error bar values were 18 με for *a* and 30 με for *c*.

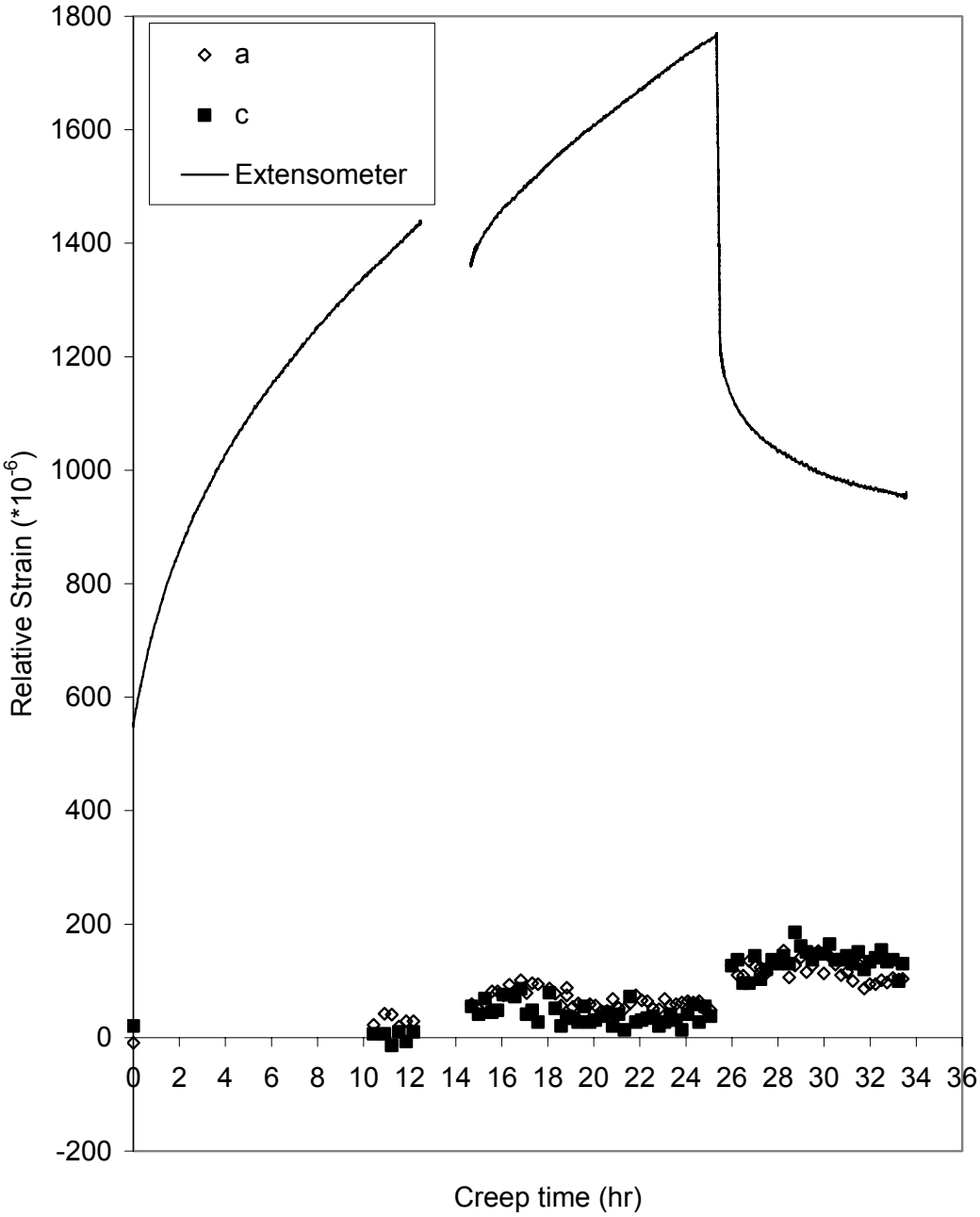

Figure A12. Transverse diffraction strain for GS44 at 1200°C under an applied creep stress of 150 MPa. Error bars are omitted for clarity. Typical error bar values were 16 με for *a* and 27 με for *c*.

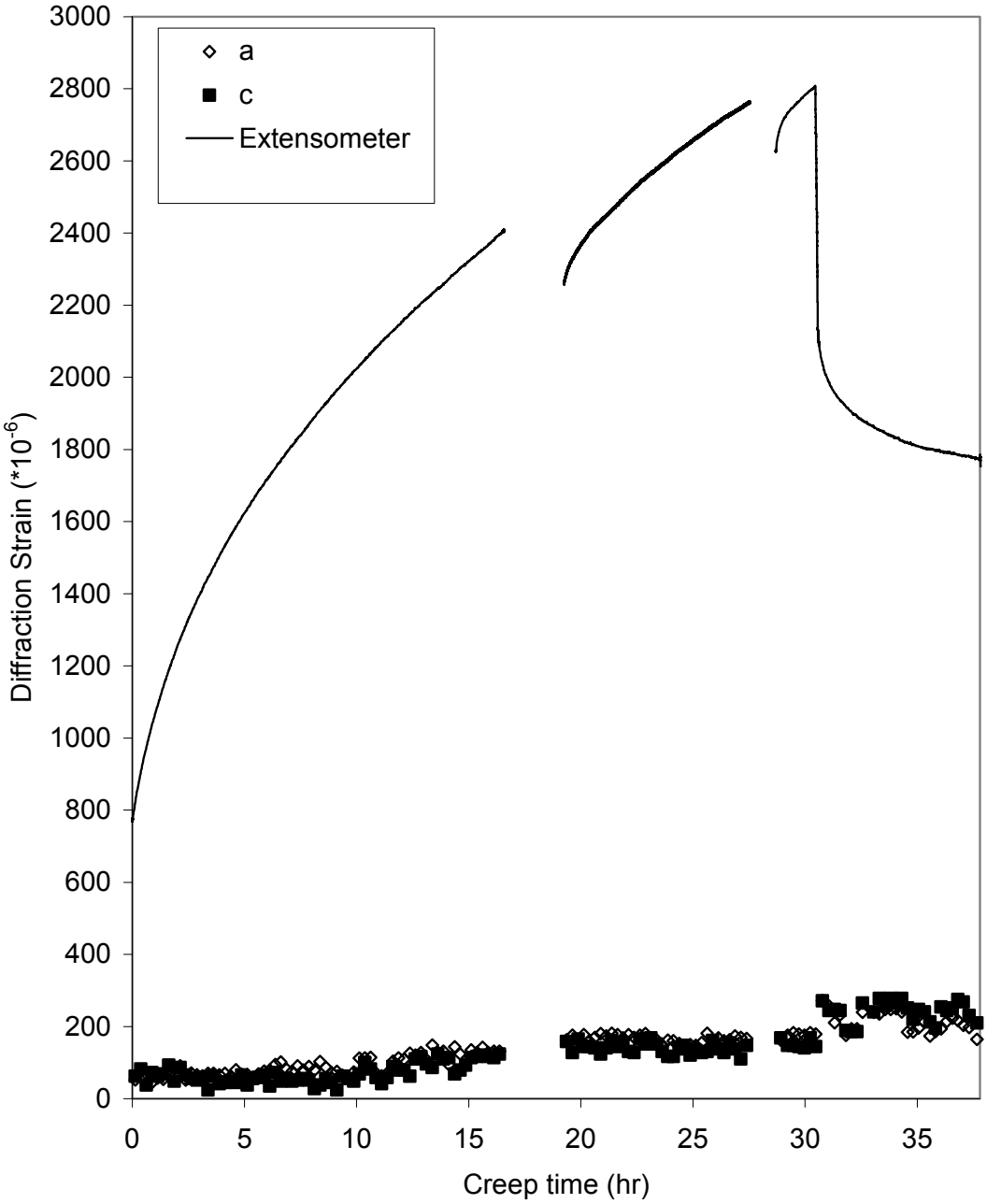

Figure A13. Transverse diffraction strain for GS44 at 1200°C under an applied creep stress of 175 MPa. Error bars are omitted for clarity. Typical error bar values were 13 με for *a* and 22 με for *c*.